Aeroacoustic Investigation of Propellers Operating at Low-Reynolds Numbers
Study of conventional and unconventional configurations

Grande, E.

DOI
10.4233/uuid:be6e22c6-594f-4733-96f5-ad08ad8723ea

Publication date
2026

Document Version
Final published version

Citation (APA)
Grande, E. (2026). *Aeroacoustic Investigation of Propellers Operating at Low-Reynolds Numbers: Study of conventional and unconventional configurations*. [Dissertation (TU Delft), Delft University of Technology]. https://doi.org/10.4233/uuid:be6e22c6-594f-4733-96f5-ad08ad8723ea

Aeroacoustic Investigation of Propellers Operating at Low-Reynolds Numbers

Study of conventional and unconventional configurations

Edoardo Grande

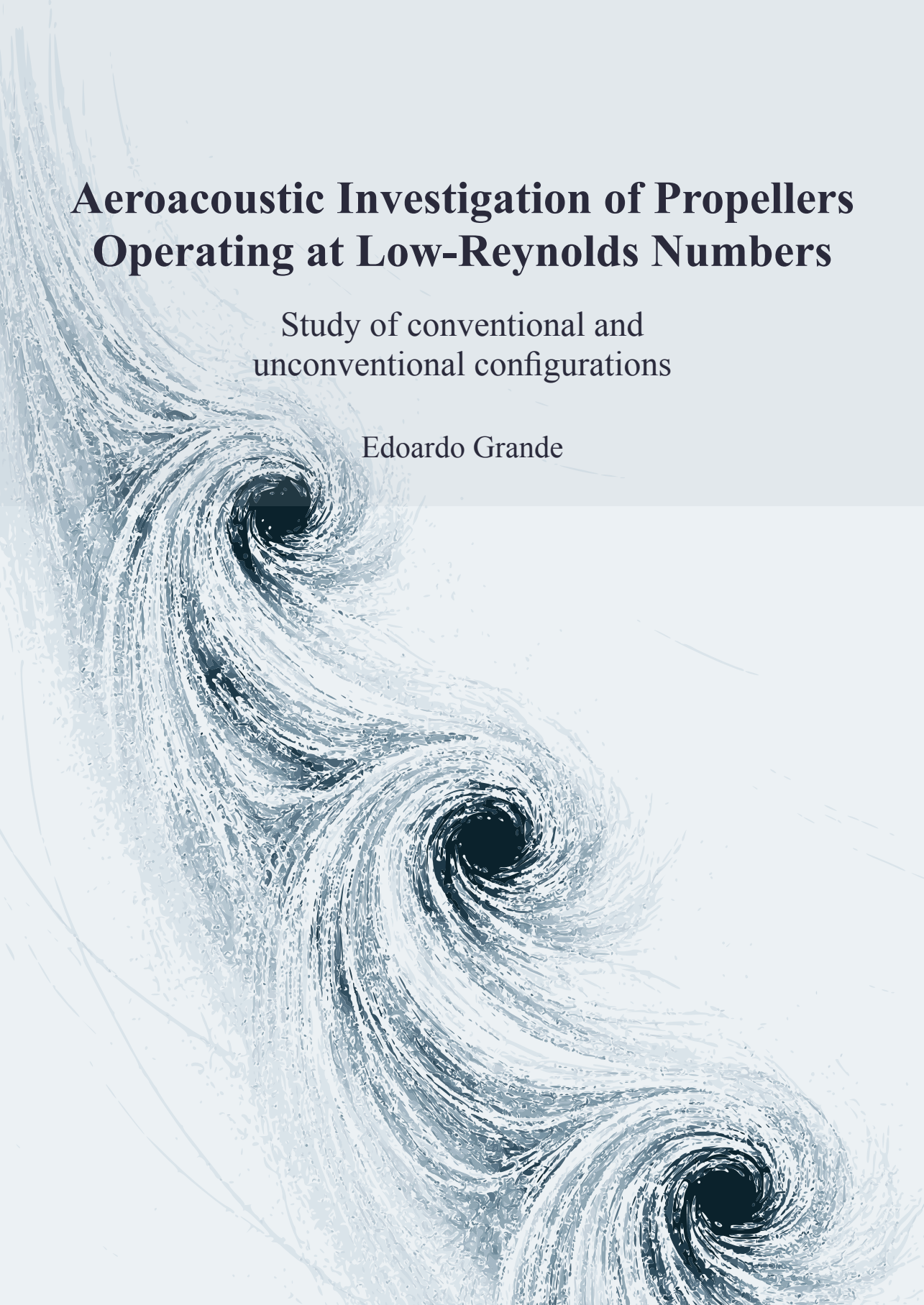

AEROACOUSTIC INVESTIGATION OF PROPELLERS OPERATING AT LOW-REYNOLDS NUMBERS

STUDY OF CONVENTIONAL AND UNCONVENTIONAL CONFIGURATIONS

AEROACOUSTIC INVESTIGATION OF PROPELLERS OPERATING AT LOW-REYNOLDS NUMBERS

STUDY OF CONVENTIONAL AND UNCONVENTIONAL CONFIGURATIONS

Dissertation

for the purpose of obtaining the degree of doctor
at Delft University of Technology,
by the authority of the Rector Magnificus, prof. dr. ir. H. Bijl,
chair of the Board for Doctorates,
to be defended publicly on Thursday 5 February 2026 at 10:00.

by

Edoardo GRANDE

This dissertation has been approved by the promotors.

Composition of the doctoral committee:

Rector Magnificus,	chairperson
Prof. dr. ing. D. Casalino,	Delft University of Technology, *promotor*
Dr. D. Ragni,	Delft University of Technology, *promotor*
Independent members:	
Prof. dr. F. Scarano,	Delft University of Technology
Prof. dr. R. Camussi,	Università Roma Tre, Italy
Prof. dr. J. Delfs,	TU Braunschweig, Germany
Dr. H. Parisot-Dupuis,	ISAE-SUPAERO, France
Prof. dr. F. Avallone,	Politecnico di Torino, Italy
Prof. dr. M. Kotsonis,	Delft University of Technology, reserve member

Keywords: Aeroacoustics, propeller noise, low-Reynolds, LSB, co-rotating rotors

Printed by: Gildeprint

Front & Back: Artistic representation of the vortical wake generated by a propeller, inspired by Particle Image Velocimetry measurements.

ISBN 978-94-6518-213-1

An electronic version of this dissertation is available at
http://repository.tudelft.nl/.

To all my friends who have ridden by my side,
on the road and beyond,
sharing climbs,
landscapes,
sheltering me from the wind.

CONTENTS

SUMMARY

Unmanned Aerial Vehicles (UAVs) and Urban Air Mobility (UAM) vehicles mark a major advancement in aviation technology, with the potential to reshape the future of aviation, particularly in the field of transportation and logistics in urban and rural environments. Undoubtedly, the noise generated by their unique propeller-driven propulsion systems poses a significant public health concern. Operating at low altitudes throughout their missions and producing an acoustic signature characterized by strong tonal noise and prominent high-frequency components, these vehicles are expected to have a greater impact on communities than traditional aircraft.

The complex acoustic signature of UAV and UAM vehicles derives mainly from two factors: the low-Reynolds number flow phenomena resulting from the small diameter of the propellers and low blade-tip speed and the unsteady, highly distorted flow caused by the unconventional integration of propellers with the airframe. This thesis addresses the first aspect, aiming to establish a fundamental understanding of noise generation mechanisms in both conventional and unconventional propeller configurations, focusing on the unique challenges posed by low Reynolds number flows. The research first examines an isolated propeller under clean inflow conditions, delving into the complex behavior of the transitional boundary layer. This understanding of isolated propeller noise generation at low Reynolds numbers is then applied to explore the potential for noise reduction using unconventional co-rotating rotor configurations.

Initially, a small-scale propeller is experimentally investigated in an anechoic wind tunnel under various axial flow conditions and rotational speeds (hence varying advance ratios J). Far-field noise measurements are coupled with load measurements and flow visualizations. The resulting far-field noise spectra exhibit both discrete tones, primarily at multiples of the blade passing frequency (BPF), and a broadband component. The first BPF tone, associated with steady loading, decreased with increasing advance ratio due to the reduction of thrust. In hover conditions, higher tonal noise between BPF 5 and 10 is observed, linked to unsteady loading from blade vortex interaction (BVI) and flow recirculation within the anechoic chamber.

A key finding of this thesis is the identification of a significant high-frequency noise emission, appearing as a hump centered around BPF 50 (7 kHz), which is attributed to wake vortex shedding originating from a laminar separation bubble (LSB). Oil-flow visualizations and velocity contours confirm a strong correlation between this high-frequency noise and the LSB on the blade suction side. As the advance ratio increases, the LSB moves toward the trailing edge and increases in chordwise dimension. This results in more coherent, larger-scale vortex shedding with increased velocity fluctuations (up to 22% of the free-stream velocity) in the wake compared to lower J conditions. Consequently, high-frequency noise increased by approximately 5 dB at $J = 0.4$ and 10 dB at $J = 0.6$ relative to the $J = 0$ (hover condition). A semi-empirical noise model is also used to further analyze the LSB vortex shedding noise, revealing that the high-frequency

hump is a result of the superposition of tones with varying amplitudes and frequencies, originating from different spanwise locations along the blade.

In the last part of the thesis, Lattice-Boltzmann simulations are employed to study two co-rotating rotor configurations in hover, each comprising two 2-bladed rotors with azimuthal separations ($\Delta\phi$) of 84° and 12°. Isolated 2- and 4-bladed rotors served as aerodynamic and aeroacoustic benchmarks. The flow analysis focused on tip vortices behavior and surface pressure distribution. For both configurations, the upper rotor tip vortices are accelerated downstream due to induction from the lower rotor, preventing BVI. In contrast, the lower rotor tip vortices stagnated near the rotor plane, causing BVI at $\Delta\phi = 12°$. The lower rotor of both configurations, operating into the upper rotor's wake, exhibited reduced aerodynamic performance: thrust decreased by 36% and 66% relative to the upper rotor at $\Delta\phi = 84°$ and 12°, respectively. Furthermore, at $\Delta\phi = 12°$, the lower blades acted as wing flaps, enhancing the upper rotor's thrust. The tonal noise emission for the co-rotating rotors is driven by the interference between the acoustic waveforms from upper and lower rotors. These waveforms (if low-pass filtered) appeared similar but time-shifted, with the shift correlated to the azimuthal separation. As a result, destructive interference led to 15 dB reduction at the first harmonic for the $\Delta\phi = 84°$ configuration compared to $\Delta\phi = 12°$. However, this was still 4.5 dB higher than the single 4-bladed rotor, which produced the lowest overall tonal noise level. The 12° configuration shows increased tonal noise due to the BVI originating at the lower rotor.

SAMENVATTING

Onbemande Luchtvaartuigen (UAVs) en Urban Air Mobility (UAM) voertuigen betekenen een enorme vooruitgang in de luchtvaarttechnologie, met het potentieel om de toekomst van de luchtvaart te hervormen, met name op het gebied van transport en logistiek in zowel stedelijke als landelijke omgevingen. Ongetwijfeld vormt de geluidsoverlast die wordt veroorzaakt door hun unieke, propeller-aangedreven aandrijfsystemen een aanzienlijk probleem voor de volksgezondheid. Door op lage hoogten te opereren tijdens hun missies en een complex akoestisch signaal te produceren dat wordt gekenmerkt door sterke tonale geluiden en prominente hoge frequentiecomponenten, wordt verwacht dat deze voertuigen een grotere impact op gemeenschappen zullen hebben dan traditionele vliegtuigen.

De complexe akoestische handtekening van UAV en UAM voertuigen is voornamelijk afkomstig van twee factoren: de onstabiele, sterk vervormde stroming veroorzaakt door de onconventionele integratie van propellers met het vliegtuigframe, en de stromingsverschijnselen bij lage Reynoldsgetallen als gevolg van de kleine diameter van de propellers en de lage bladsnelheid. Dit proefschrift richt zich op het laatste aspect en beoogt een fundamenteel begrip te vestigen van de mechanismen van geluidsgeneratie in zowel conventionele als onconventionele propellerconfiguraties voor UAV's en UAM-voertuigen, waarbij de nadruk ligt op de unieke uitdagingen die worden gesteld door stromingen bij lage Reynoldsgetallen. Het onderzoek begint met een onderzoek naar een geïsoleerde propeller onder schone instroomomstandigheden, waarbij de complexe eigenschappen van de transitiegrenslaag worden onderzocht die optreedt bij lage Reynoldsgetallen. Deze fundamentele kennis van de geluidsgeneratie door een geïsoleerde propeller bij lage Reynoldsgetallen wordt vervolgens toegepast om het potentieel voor geluidsreductie te onderzoeken met behulp van onconventionele co-roterende rotorconfiguraties.

Aanvankelijk wordt experimenteel onderzoek uitgevoerd in een anechoïsche windtunnel aan een kleine propeller onder verschillende axiale stromingsomstandigheden en rotatiesnelheden (en dus verschillende voortstuwingscoëfficiënten J). Met behulp van metingen in het verre veld wordt de geluidsproductie gekoppeld aan belastingmetingen en stromingsvisualisaties. De resulterende geluidsspectra in het verre veld vertonen zowel discrete tonen, voornamelijk op veelvouden van de bladdorssnelheid (BPF), als een breedbandcomponent. De eerste BPF-toon, geassocieerd met stabiele belasting, neemt af naarmate de voortstuwingscoëfficiënt toeneemt, als gevolg van de vermindering van de stuwkracht. In zweefcondities wordt een hogere tonale geluidsproductie waargenomen tussen BPF 5 en 10, gekoppeld aan onstabiele belasting die wordt gegenereerd door bladwerveling interactie (BVI) en ongewenste stromingsrecirculatie in de anechoïsche windtunnel.

Een belangrijke bevinding van dit proefschrift is de identificatie van een significante hoge frequentiegeluidsemissie, die zich voordoet als een piek rond BPF 50 (7 kHz), die

wordt toegeschreven aan wervelafstoting afkomstig van een laminaire scheidingsbel (LSB). Visualisaties van de oliestroom en snelheidscontouren bevestigen een sterke correlatie tussen deze hoge frequentiegeluid en de LSB aan de zuigzijde van het blad. Naarmate de voortstuwingscoëfficiënt toeneemt, beweegt de LSB zich richting de achterrand en neemt de akkoordwijdte toe. Dit resulteert in meer coherente, grootschaligere wervelafstoting met verhoogde snelheidsschommelingen (tot 22% van de vrije stromingssnelheid) in de kielzog, in vergelijking met omstandigheden met een lagere J. Dientengevolge neemt het hoge frequentiegeluid toe met ongeveer 5 dB bij ($J = 0.4$) en 10 dB bij ($J = 0.6$) ten opzichte van de zweefconditie ($J = 0$). Het aanbrengen van een turbulator aan de zuigzijde onderdrukte de vorming van de LSB en de daarmee gepaard gaande geluidsemissie. Een semi-empirisch geluidsmodel wordt ook gebruikt om de geluidsafgifte door de LSB-wervelafstoting verder te analyseren, wat aangeeft dat de piek op hoge frequentie het resultaat is van de superpositie van tonen met verschillende amplitudes en frequenties, die afkomstig zijn van verschillende spanwijdtelocaties langs het blad.

In het laatste deel van dit proefschrift worden Lattice-Boltzmann simulaties gebruikt om twee co-roterende rotorconfiguraties in zweefvlucht te bestuderen, elk bestaande uit twee 2-bladige rotoren met azimutale scheidingen ($\Delta\phi$) van 84° en 12°. Geïsoleerde 2- en 4-bladige rotoren dienden als aerodynamische en aeroakoestische benchmarks. De stromingsanalyse richtte zich op het gedrag van de vleugelpuntwervels en de verdeling van de oppervlaktedruk. Voor beide configuraties werden de vleugelpuntwervels van de bovenste rotor versneld stroomafwaarts door inductie van de onderste rotor, waardoor BVI werd voorkomen. Daarentegen stagneerden de vleugelpuntwervels van de onderste rotor in de buurt van het rotorvlak, wat leidde tot BVI bij $\Delta\phi = 12°$. De onderste rotor van beide configuraties, die in de kielzog van de bovenste rotor werkt, vertoonde verminderde aerodynamische prestaties: de stuwkracht nam af met 36% en 66% ten opzichte van de bovenste rotor bij respectievelijk $\Delta\phi = 84°$ en 12°. Bovendien fungeerden de onderste bladen bij $\Delta\phi = 12°$ als vleugelkleppen, waardoor de stuwkracht van de bovenste rotor werd vergroot. De tonale geluidsemissie voor de co-roterende rotoren wordt veroorzaakt door de interferentie tussen de akoestische golfvormen van de bovenste en onderste rotoren. Deze golfvormen (na laagdoorlaatfiltering) lijken vergelijkbaar, maar zijn in de tijd verschoven, waarbij de verschuiving gecorreleerd is met de azimutale scheiding. Als gevolg hiervan leidde destructieve interferentie tot een reductie van 15 dB in de eerste harmonische voor de $\Delta\phi = 84°$ configuratie in vergelijking met $\Delta\phi = 12°$. Deze was echter nog steeds 4,5 dB hoger dan de enkele 4-bladige rotor, die het laagste totale tonale geluidsniveau produceerde. De 12° configuratie vertoonde een verhoogd tonale geluidsniveau als gevolg van de BVI die bij de onderste rotor ontstond.

1

INTRODUCTION

In recent years, Unmanned Aerial Vehicles (UAVs) and Urban Air Mobility (UAM) vehicles have emerged as promising solutions for providing, among various applications, efficient transportation solutions and addressing traffic congestion. Nevertheless, the noise pollution generated by these vehicles in urban areas constitutes a limiting factor to their expansion. This chapter provides an overview of these technologies and their applications, alongside an analysis of their noise-related environmental impact. It then outlines the challenges of predicting the aeroacoustic noise generated by propeller-driven UAVs and UAM vehicles, establishing the scope of this research. Finally, the thesis structure is presented.

1

1.1. THESIS BACKGROUND

Currently, a variety of electric and autonomous aerial technologies are being developed, with the potential to revolutionize the future of aviation. These innovations include Unmanned Aerial Vehicles (UAVs), which vary in size from just a few grams to several hundred kilograms and are available in both multi-rotor and fixed-wing configurations, and Urban Air Mobility (UAM) vehicles, represented by electric Vertical Take-Off and Landing (eVTOL) concepts, designed to transport people within urban areas, alleviating ground congestion.

UAVs are aircraft that operate without a human pilot onboard, using advanced autonomous systems for navigation and control. The applications of UAVs are diverse and rapidly expanding across various sectors [23]. In the commercial domain, UAVs have emerged as a revolutionary solution for package delivery due to their potential to significantly reduce delivery times compared to traditional ground transportation methods [29]. In agriculture, UAVs provide farmers with aerial imagery and data collection capabilities for crop monitoring, precision agriculture, and pest management [37]. The healthcare sector has also seen the emergence of UAV applications, with drones facilitating the rapid transport of medical supplies, vaccines, and even organs for transplantation [24]. Additionally, drones are utilized in environmental monitoring to collect data on wildlife, assess the impact of natural disasters, and conduct search and rescue operations [13]. The construction industry benefits from UAVs through site surveys, real-time monitoring, and progress tracking. In the area of surveillance and security, UAVs offer an effective solution for law enforcement and military applications by providing reconnaissance capabilities, including nighttime operations through the use of thermal cameras. Figure 1.1 presents examples of two UAVs: the DJI Flycart 30 (Fig. 1.1a), a cargo drone capable of delivering heavy packages in challenging conditions. It cover a range of 16 km with a 30 kg payload and can operate in temperatures ranging from $-20°$ to $45°$, as well as wind speeds up to 43 km/h. The DJI Agras T50 (1.2b) is an agricultural drone featuring a 40 kg spraying payload and a dual atomizing spraying system, capable of covering up to 21 hectares per hour. Both UAVs depicted in the figure are equipped with a propulsive system consisting of four contra-rotating rotors.

(a) DJI Flycart 30 [12]

(b) DJI Agras T50 [11]

Figure 1.1: Recent UAVs for package delivery and agriculture.

On the horizon, UAM promises to revolutionize inner-city transportation by providing on-demand air travel options through the use of flying vehicles. On-demand mobility refers to personal transportation solutions where users can select the details of their trip, including the origin, destination, and departure time [26]. One of the primary motivations behind developing alternatives to conventional car-based ground mobility is to reduce traffic congestion and shorten travel times. In this context, several companies are actively engaged in developing and prototyping electric Vertical Take-Off and Landing (eVTOL) concepts, which are also referred to as Personal Aerial Vehicles (PAVs). These fully electric vehicles aim not only to ease road traffic but also to produce zero in-flight gas emissions, thereby significantly contributing to reducing fossil fuel emissions [17]. Figure 1.2 shows two recent eVTOL concepts: the first is the CityAirbus NextGen (Fig. 1.2a), an eVTOL capable of carrying four passengers with an anticipated range of 80 km and a cruising speed of 120 km/h; the second is the Bell Nexus 6HX (Fig. 1.2b), a concept eVTOL designed for five passengers, with an expected range of 241 km and a top speed of 288 km/h.

(a) CityAirbus NextGen [1]

(b) Bell Nexus 6HX [14]

Figure 1.2: Recent eVTOL concepts for Urban Air Mobility.

1.2. NOISE IMPACT OF UAVS AND UAM VEHICLES

As these innovative aerial platforms increasingly populate our skies, concerns regarding their environmental impact, particularly noise emissions, have arisen. The noise signature of UAVs [1] differs from that of traditional aircraft [7]. Hence, they constitute a novel noise source unfamiliar to the human ear. Furthermore, UAVs will affect larger areas, including urban regions where road traffic noise is minimal. Torija et al. [31] found that in such areas, the same UAV operation producing the same noise level is perceived as significantly more annoying compared to areas with high road traffic. Given the public's strong concerns about UAV noise [36], effective noise mitigation strategies are crucial to ensure the technology's widespread acceptance.

[1] For brevity, only UAVs are addressed throughout this section, but the discussion is equally applicable to UAM vehicles.

1

1.2.1. ACOUSTIC SPECTRUM CHARACTERISTICS

Figure 1.3 presents the noise spectra from two UAVs during level flyover: a DJI M200 quadcopter and a Yuneec Typhoon hexacopter. The spectra reveal two distinct characteristics:

- significant noise radiation at high frequencies;
- the presence of multiple tones in a large frequency range.

The high-frequency noise content in UAVs is primarily due to airfoil blade self-noise (resulting from the interaction between airflow and rotor blades) [20], interactions between multiple rotors, and electric motor noise [18, 16]. In commercial aircraft, high-frequency noise is reduced due to atmospheric absorption in long-range propagation. In contrast, for UAVs flying much closer to the ground, atmospheric absorption has a negligible impact. Consequently, high-frequency noise is likely to be a significant source of annoyance during UAV operations.

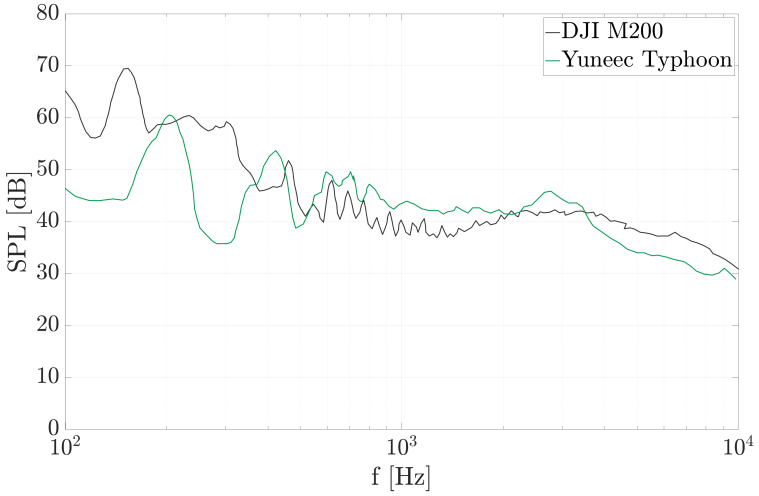

Figure 1.3: Noise spectra for DJI M200 and Yuneec Typhoon UAVs during flyover at an altitude of 45.7 meters [30]. Spectra are normalized to 65 dB(A).

The multiple tones originate from the periodic interactions of the propeller blades with the airflow and occur at multiples of the blade passing frequencies (BPFs) of each rotor [32]. Under steady conditions, such as hovering in laboratory settings, the noise spectrum displays clear tonal components, with the first harmonic being the most prominent, and decreasing levels for the higher harmonics [25]. However, during maneuvers (as flyover or landing in real scenarios), the propellers experience uneven loading, which alters the composition of the tonal components and directivity. Additionally, atmospheric conditions, including wind gusts, significantly impact tonal noise emission [33]. When the UAV encounters a wind gust, it rapidly adjusts the rotational frequency

of the propellers to maintain stability, resulting in an unsteady acoustic response characterized by fluctuations in the tonal components. The changes in rotational speed also cause a reduction of the maximum amplitude of the tonal components and a dispersion at higher harmonics [25].

1.2.2. REGULATION AND METRICS

Depending on the type of noise certification procedure, different frequency-weighted noise metrics are used for commercial aircraft. These include the maximum A-weighted sound power level $L_{wA,max}$, the Day-Night Average Sound Level (L_{DN}), which adds a penalty to nighttime noise levels, and the Sound Exposure Level (L_{AE}), which is useful for comparing noise events of varying durations by normalizing total energy to a one-second equivalent. These metrics do not adequately account for tonal noise. The only metric that includes a penalty for tonal noise is the Effective Perceived Noise Level (EPNL), which is the primary standard used in aviation for the certification of both fixed-wing and rotary-wing aircraft [10]. EPNL measures human annoyance to aircraft noise by means of the Perceived Noise Level (PNL) and adding corrections for the duration of the event and pure tones. Table 1.1 compares EPNL values for two commercial aircraft with target EPNL values for two UAM vehicles (note that UAM noise standards are not yet fully established, hence only target values are provided).

Aircraft type	Model	Noise Level (EPNdB)
Civil aircraft	Airbus 330-600R	Take-off: 92.1, Landing: 101.7
	Boeing 737-800	Take-off: 88.6, Landing: 96.4
UAM	Bell Nexus (5-seater)	67 (target)
	CityAirbus (4-seater)	70 (target)

Table 1.1: EPNdB levels for various aircraft types [21]. For commercial aircraft, the levels are measured on the runway, whereas for UAM vehicles, they represent target values.

The EPNL metric is insufficient for assessing human annoyance from UAV noise for several reasons [21]. To begin with, it specifies the maximum allowable noise during takeoff and landing and defines zones around airports with varying noise exposure levels. While commercial aircraft fly at low altitudes only during takeoff and landing, UAVs operate close to urban areas throughout their entire missions, leading to a wider impact on urban residents than commercial aircraft. Cussen et al. [9] modeled the noise emission of a small-scale UAV during a flyover in an urban area with background noise levels of $L_{DN} = 60 - 64$ dB(A). This level was exceeded by up to 10 dB, partly due to building surfaces that further amplified noise levels through reflection. Additionally, the EPNL metric assumes a relatively constant noise source and cannot account for the continuous adjustments in rotor rotational frequency made to maintain stability, which cause fluctuating tones. Although EPNL includes a tonal penalty, it inadequately addresses the perceptual effects of the complex series of tones distributed across a wide frequency range. Moreover, EPNL is based on one-third octave spectra with center frequency bands ranging from 50 Hz to 10 kHz, thereby completely omitting significant high-frequency noise above 10 kHz present in the UAV noise signature.

The EU has recently implemented regulations that establish testing standards and

limits for the maximum A-weighted sound power level ($L_{wA,max}$) for various classes of UAVs [8]. The measurement procedure adheres to the ISO 3744:2010 [19] standard and requires that the UAV must be tested in an anechoic chamber while hovering at its maximum takeoff mass above a reflecting surface. Noise measurements must be taken on a hemispherical surface. The regulations also specify requirements for reductions in $L_{wA,max}$ two and four years after the regulations came into effect. However, this testing methodology may not adequately capture the noise produced by UAVs during real flight operations. As previously discussed, noise generated by a drone hovering in a controlled environment significantly differs in directivity and tonal component characteristics from that of the same drone performing maneuvers such as takeoff, landing, and flyover. Additionally, there are concerns regarding the use of $L_{wA,max}$ as a noise metric, as it does not sufficiently represent noise spectrum characteristics like high-frequency noise and tonal components [30].

There is a need to tailor existing metrics (or develop new ones) specifically for UAV noise. These metrics should include a finer frequency resolution and effectively account for multiple tones. Sound quality metrics, such as loudness, tonality, sharpness [38], and others, could be applied to UAV noise to provide a more comprehensive evaluation of how it is perceived. Loudness would quantify the intensity of UAV noise as perceived by people on the ground, while sharpness could assess discomfort or annoyance from high-frequency components. Gwak et al. [15] demonstrated that UAV annoyance is strongly tied to these two metrics. Tonality would evaluate the presence and dominance of tonal components within the noise spectrum, and impulsiveness would help understand the perceived disruption from sudden noise level changes as a UAV appears quickly. The last metric is crucial given the intermittent and unpredictable nature of UAVs, which often operate beyond the line of sight due to obstructions from buildings, complicating the determination of their exact locations. This can increase sensory discomfort by creating anxiety from the perceived proximity of an unseen vehicle and concerns about uncontrollable incidents [21].

1.3. RESEARCH OBJECTIVES

As highlighted in Sect. 1.1, despite the diversity of UAV and UAM vehicle designs, a common feature across these platforms is their reliance on propeller-based propulsion systems. These systems consist of either isolated or distributed propellers, which facilitate vertical take-off, landing, and hovering capabilities.

The aeroacoustic prediction of noise generated by these propellers presents several challenges [4, 3]. Firstly, these vehicles operate under diverse conditions due to different mission profiles and flight phases, each affecting the noise level differently. Secondly, the unconventional integration of propellers with the airframe results in complex aerodynamic behaviour. One key difficulty arises from the fact that these propellers frequently operate in distorted [27] and turbulent flow environments, particularly in the wakes of other propellers or behind lifting surfaces (see the schematic of the eVTOL in Fig. 1.4). Additionally, in multi-propeller configurations, the interaction between the propellers induces unsteady flow conditions, and the overall noise pattern experiences constructive or destructive interference, adding complexity to noise modeling. Finally, besides single rotor systems, also unconventional rotor configurations such as contra- and co-

rotating rotors, are being explored with the aim of increasing the thrust-to-weight ratio and reducing tonal noise.

In addition to the challenges arising from interactions between the propeller and the airframe or between multiple propellers, the small size of the propellers and their low blade-tip speed, expose them to low-Reynolds number phenomena. At a chord-based Reynolds number Re_c ranging from 10^4 to 10^5, the boundary layer on the blade surface exhibits complex behaviours such as laminar separation, transition and potential reattachment, leading to the formation of a laminar separation bubble (LSB). Under these conditions, vortex shedding is frequently observed [35]. These intricate flow mechanisms drive the airfoil self-noise generation, significantly influencing the acoustic properties of the propellers and adding complexity to noise prediction efforts.

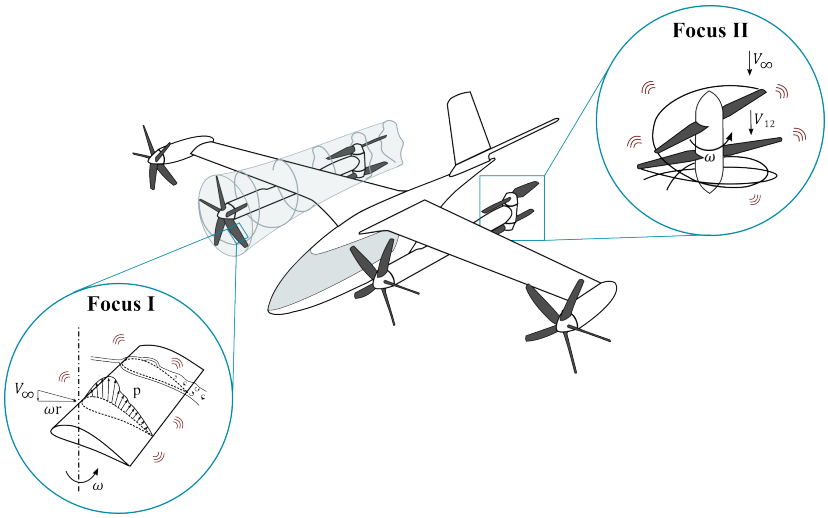

Figure 1.4: Schematic of a eVTOL aircraft highlighting the research focus areas: (I) noise generation from isolated propellers at low Reynolds numbers, including transitional boundary layer effects, and (II) co-rotating rotor noise.

Given the challenges outlined above, existing prediction tools, originally developed for traditional helicopters and fixed-wing aircraft, offer only limited applicability. While they can provide rough estimates of noise emissions from UAV and UAM systems, they do not adequately capture the unique noise generation mechanisms associated with these new classes of vehicles, often resulting in substantial inaccuracies [22].

In this context, this research specifically focuses on the fundamental aspects of noise generation mechanisms from conventional and unconventional propellers operating at low-Reynolds numbers, intentionally discarding the effects of flow distortion and turbulence resulting from the interaction with other propellers and the airframe. These two research focus areas are highlighted in Fig. 1.4. The first part of the study (Focus I) investigates an isolated small-scale rotor, delving into the behaviour of the transitional boundary layer which occurs under these unique conditions to establish a foundational

understanding of noise generation mechanisms and provide insights into noise mitigation strategies. The second part (Focus II) transitions to the investigation of unconventional configurations, specifically co-rotating rotor systems. Applying insights obtained from the isolated propeller analysis, it examines the aeroacoustic properties of co-rotating rotors and assesses their potential for noise reduction.

The isolated propeller research is carried out through experiments in an anechoic wind tunnel. Far-field noise measurements are integrated with flow visualizations and load measurements. An experimental approach is preferred over high-fidelity simulations due to the challenges that CFD solvers face in accurately predicting transitional flow characteristics [28, 2]. Nonetheless, several experimental challenges are faced, such as the small chordwise dimensions of the blades complicating flow visualizations, and the potential influence of electric motor noise [18, 16] and test-rig vibrations on acoustic measurements.

Conversely, a numerical approach based on the Lattice-Boltzmann/Very-Large Eddy Simulation (LB/VLES) method [5, 6], coupled with the Ffowcs Williams and Hawkings (FW-H) acoustic analogy [34], is employed in the second part of the thesis to investigate the co-rotating rotor configurations. The LB/VLES method, known for its low dissipation and capability to provide unsteady flow solutions, is particularly well-suited for studying the fundamental physics of the flow fields generated by co-rotating rotors. It is especially effective at capturing the interactions between the upper and lower rotors of the co-rotating systems, which are the primary phenomena driving noise generation.

Thus, the main scope of this research is encapsulated in the following statement:

To assess the noise emitted by conventional and unconventional propeller configurations operating at low-Reynolds numbers under clean inflow conditions.

Achieving this objective involves addressing the following key points:

- Characterize the primary tonal and broadband noise sources in isolated propellers operating at low-Reynolds numbers;
- Investigate the unique flow phenomena at low-Reynolds numbers, such as the behavior of the transitional boundary layer, and quantify their effects on the far-field noise spectrum;
- Determine how these characteristic low-Reynolds noise sources can be modelled using low-fidelity methods;
- Analyze the aeroacoustic characteristics of unconventional rotor configurations, such as co-rotating rotors, and evaluate their potential to reduce noise while enhancing the aerodynamic performance in comparison to traditional isolated rotors.

1.4. THESIS OUTLINE

The thesis is organized into seven chapters, structured as follows:

- Chapter 1 establishes the context for the research, outlining the objectives and the general approach chosen to achieve them.
- Chapter 2 offers a detailed description of the main noise sources for an isolated propeller operating at low Reynolds numbers. Initially, it provides an understanding of low-Reynolds airfoil blade aerodynamics, emphasizing boundary layer behavior and lift and drag characteristics. Then it details the primary tonal and broadband rotor noise sources. The chapter concludes by exploring unconventional rotor configurations, particularly co-rotating rotors, detailing their geometry and potential for noise reduction.
- Chapter 3 presents an overview of the experimental and numerical methodologies utilized throughout the thesis. It describes the flow and acoustic measurement techniques employed during the experimental campaign and the numerical formulation applied, based on the Lattice Boltzmann Method (LBM) coupled with the Ffowcs-Williams and Hawkings (FW-H) acoustic analogy.
- Chapters 4 to 6 constitute the original contribution to the thesis and are derived from the journal articles published by the authors during the PhD. In particular:
  - Chapter 4 presents an experimental investigation of an isolated propeller operating at low Reynolds numbers. It first offers a detailed analysis of the flow behavior on the blade surface and around a specific blade section, followed by an analysis of the noise spectra under different operating conditions.
  - Chapter 5 continues the experimental investigation using the same propeller as in Chapter 4, focusing on quantifying the noise radiation caused by a LSB. It begins with an analysis of LSB behavior at different advance ratios, linking these findings to the far-field noise spectra. Additionally, a semi-empirical noise model provides a physical interpretation of the acoustic spectra.
  - Chapter 6 uses Lattice-Boltzmann simulations to investigate the flow field and far-field noise of two coaxial co-rotating rotor configurations. It includes a detailed examination of the aerodynamic performance and flow interaction between the upper and lower rotors within these co-rotating configurations. Finally, the results are compared to an isolated rotor case to determine whether the co-rotating rotors can simultaneously achieve higher thrust and lower noise.
- Chapter 7 summarizes the key findings of the research and offers recommendations for future work.

BIBLIOGRAPHY

[1] Airbus. *CityAirbus NextGen*. https://www.airbus.com/en/innovation/energy-transition/hybrid-and-electric-flight/cityairbus-nextgen. 2024.

[2] Damiano Casalino, Gianluca Romani, Raoyang Zhang, and Hudong Chen. "Lattice-Boltzmann calculations of rotor aeroacoustics in transitional boundary layer regime". In: *Aerospace Science and Technology* 130 (2022), p. 107953.

[3] Damiano Casalino, Wouter van der Velden, and Gianluca Romani. "Community Noise of Urban Air Transportation Vehicles". In: *2019 AIAA Aerospace Sciences Meeting*. Jan. 2019. DOI: 10.2514/6.2019-1834.

[4] Damiano Casalino, Wouter van der Velden, Gianluca Romani, and Ignacio Gonzalez-Martino. "Aeroacoustic Analysis of Urban Air Operations using the LB/VLES Method". In: *25th AIAA/CEAS Aeroacoustics Conference*. May 2019. DOI: 10.2514/6.2019-2662.

[5] H. Chen, S. Chen, and W. H. Matthaeus. "Recovery of the Navier-Stokes equations using a lattice-gas Boltzmann method". In: *Physical Review A* 45 (1992), R5339–R5342. DOI: 10.1103/PhysRevA.45.R5339.

[6] Hudong Chen, Steven A Orszag, Ilya Staroselsky, and Sauro Succi. "Expanded analogy between Boltzmann kinetic theory of fluids and turbulence". In: *Journal of Fluid Mechanics* 519 (2004), pp. 301–314.

[7] Andrew W Christian and Randolph Cabell. "Initial investigation into the psychoacoustic properties of small unmanned aerial system noise". In: *23rd AIAA/CEAS aeroacoustics conference*. 2017, p. 4051.

[8] *Commission Delegated Regulation (EU) 2020/1058 of 27 April 2020 amending Delegated Regulation (EU) 2019/945 as regards the introduction of two new unmanned aircraft systems classes*. Official Journal of the European Union. 2020. URL: https://eur-lex.europa.eu/eli/reg_del/2020/1058/oj.

[9] Kai Cussen, Simone Garruccio, and John Kennedy. "UAV noise emission. A combined experimental and numerical assessment". In: *Acoustics*. Vol. 4. 2. MDPI. 2022, pp. 297–312.

[10] Neil Dickson. "ICAO noise standards". In: *ICAO Symposium on Aviation and Climate Change*. Vol. 202. 2013.

[11] DJI. *DJI Agras T50*. https://www.dji.com/it. 2026.

[12] DJI. *DJI Flycart 30*. https://www.dji.com/it. 2026.

[13] Mario Arturo Ruiz Estrada and Abrahim Ndoma. “The uses of unmanned aerial vehicles–UAV’s-(or drones) in social logistic: Natural disasters response and humanitarian relief aid”. In: *Procedia Computer Science* 149 (2019), pp. 375–383.

[14] eVTOL news. *Bell Nexus 6HX*. https://evtol.news/bell-air-taxi. 2025.

[15] Doo Young Gwak, Dongyeon Han, and Soogab Lee. “Sound quality factors influencing annoyance from hovering UAV”. In: *Journal of sound and vibration* 489 (2020), p. 115651.

[16] Brenda S. Henderson and Dennis Huff. “Electric Motor Noise for Small Quadcopters: Part II - Source Characteristics and Predictions”. In: *2018 AIAA/CEAS Aeroacoustics Conference*. 2018. DOI: 10.2514/6.2018-2953. URL: https://arc.aiaa.org/doi/abs/10.2514/6.2018-2953.

[17] Jeff Holden and Nikhil Goel. “Fast-forwarding to a future of on-demand urban air transportation”. In: *San Francisco, CA* (2016).

[18] Dennis L. Huff and Brenda S. Henderson. “Electric Motor Noise for Small Quadcopters: Part 1 – Acoustic Measurements”. In: *2018 AIAA/CEAS Aeroacoustics Conference*. 2018. DOI: 10.2514/6.2018-2952. URL: https://arc.aiaa.org/doi/abs/10.2514/6.2018-2952.

[19] *ISO 3744:2010 - Acoustics — Determination of sound power levels and sound energy levels of noise sources using sound pressure — Engineering methods for an essentially free field over a reflecting plane*. International Organization for Standardization, 2010.

[20] William A Jordan, Shreyas Narsipur, and Robert Deters. “Aerodynamic and aeroacoustic performance of small uav propellers in static conditions”. In: *Aiaa Aviation 2020 Forum*. 2020, p. 2595.

[21] JungHoon Kim. “Urban air mobility noise: Further considerations on indoor space”. In: *International Journal of Environmental Research and Public Health* 19.18 (2022), p. 11298.

[22] Stefan Letica and Stephen Rizzi. “On the modeling of urban air mobility vehicle takeoff and landing operations in the FAA Aviation Environmental Design Tool”. In: *INTER-NOISE and NOISE-CON Congress and Conference Proceedings*. Vol. 269. 2. Institute of Noise Control Engineering. 2024, pp. 270–282.

[23] Syed Agha Hassnain Mohsan, Nawaf Qasem Hamood Othman, Yanlong Li, Mohammed H Alsharif, and Muhammad Asghar Khan. “Unmanned aerial vehicles (UAVs): Practical aspects, applications, open challenges, security issues, and future trends”. In: *Intelligent Service Robotics* 16.1 (2023), pp. 109–137.

[24] Albert Apotele Nyaaba and Matthew Ayamga. “Intricacies of medical drones in healthcare delivery: Implications for Africa”. In: *Technology in Society* 66 (2021), p. 101624.

[25] Carlos Ramos-Romero, Nathan Green, Antonio J Torija, and César Asensio. "On-field noise measurements and acoustic characterisation of multi-rotor small unmanned aerial systems". In: *Aerospace Science and Technology* 141 (2023), p. 108537.

[26] AD Rohn. "NASA aeronautics: overview & ODM". In: *On-Demand Mobility Forum*. 2015.

[27] Gianluca Romani, Edoardo Grande, Francesco Avallone, Daniele Ragni, and Damiano Casalino. "Computational study of flow incidence effects on the aeroacoustics of low blade-tip Mach number propellers". In: *Aerospace Science and Technology* 120 (2022), p. 107275.

[28] Gianluca Romani, Edoardo Grande, Francesco Avallone, Daniele Ragni, and Damiano Casalino. "Performance and noise prediction of low-Reynolds number propellers using the Lattice-Boltzmann method". In: *Aerospace Science and Technology* (Sept. 2021), p. 107086. DOI: 10.1016/j.ast.2021.107086.

[29] Jack Saunders, Sajad Saeedi, and Wenbin Li. "Autonomous aerial robotics for package delivery: A technical review". In: *Journal of Field Robotics* 41.1 (2024), pp. 3–49.

[30] Antonio J Torija and Charlotte Clark. "A psychoacoustic approach to building knowledge about human response to noise of unmanned aerial vehicles". In: *International Journal of Environmental Research and Public Health* 18.2 (2021), p. 682.

[31] Antonio J Torija, Zhengguang Li, and Rod H Self. "Effects of a hovering unmanned aerial vehicle on urban soundscapes perception". In: *Transportation Research Part D: Transport and Environment* 78 (2020), p. 102195.

[32] Antonio J Torija and Rory K Nicholls. "Investigation of metrics for assessing human response to drone noise". In: *International Journal of Environmental Research and Public Health* 19.6 (2022), p. 3152.

[33] Antonio J Torija, Rod H Self, and Jack LT Lawrence. "Psychoacoustic characterisation of a small fixed-pitch quadcopter". In: *Inter-Noise and Noise-Con Congress and Conference Proceedings*. Vol. 259. 8. Institute of Noise Control Engineering. 2019, pp. 1884–1894.

[34] J. E. Ffowcs Williams and D. L. Hawkings. "Sound Generation by Turbulence and Surfaces in Arbitrary Motion". In: *Philosophical Transactions of the Royal Society of London* 264.1151 (1969), pp. 321–342.

[35] Serhiy Yarusevych, Pierre Sullivan, and John Kawall. "Coherent structures in an airfoil boundary layer and wake at low Reynolds numbers". In: *Physics of Fluids* 18 (Apr. 2006), p. 044101. DOI: 10.1063/1.2187069.

[36] Pavan Yedavalli and Jessie Mooberry. "An assessment of public perception of urban air mobility (UAM)". In: *Airbus UTM: Defining Future Skies* (2019), 2046738-072–1580045281.

[37] Chunhua Zhang and John M Kovacs. “The application of small unmanned aerial systems for precision agriculture: a review”. In: *Precision agriculture* 13 (2012), pp. 693–712.

[38] Eberhard Zwicker and Hugo Fastl. *Psychoacoustics: Facts and models*. Vol. 22. Springer Science & Business Media, 2013.

2

AIRFOILS AND ROTORS CHARACTERISTICS AT LOW-REYNOLDS NUMBERS

Small-scale propellers operating at low-Reynolds numbers encounter distinctive aerodynamic challenges that significantly influence their noise emission. This chapter begins with an in-depth overview of the aerodynamics of low-Reynolds airfoil blades, with a focus on the lift and drag characteristic and the behavior of transitional boundary layer. This forms the foundation for Sect. 2.3, which examines the main tonal and broadband noise generation mechanisms in these propellers, with emphasis on the noise from laminar boundary layer vortex shedding. The final section shifts the focus to non-traditional rotor designs, specifically introducing the concept of co-rotating rotors, which will be the primary subject of the concluding part of the thesis.

2.1. PROPELLER NOISE SOURCES: AN OVERVIEW

As described in Sect. 1.3, the different concepts of UAVs and UAMs vehicles proposed so far have in common the type of propulsion system, which consists of either isolated or distributed propellers. The far-field noise spectrum associated with these propellers includes spectral characteristics common to all types of rotors, as well as features specific to unique low-Reynolds aerodynamic phenomena. Generally, both tonal (or rotational) and broadband components can be recognized in the noise spectrum. Fig. 2.1 provides a sketch of a potential far-field noise spectrum from a small-scale rotor.

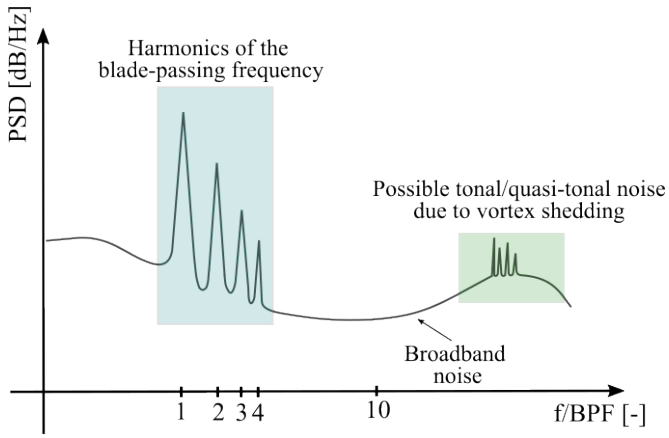

Figure 2.1: Example of a propeller far-field noise spectrum. The frequency axis is normalized relative to the blade passing frequency $BPF = Bn$, where B is the number of blades and n is the propeller rotational frequency in Hz.

Tonal noise is due to all the periodic interactions of the rotor blades with the flow itself. At low blade-tip Mach numbers, the primary tonal noise source is represented by steady and unsteady loading (in a blade-based reference system) and referred as *loading noise*. If the propeller operates in a uniform and stationary inflow, the pressure, and thus the loading, remains steady in a blade-based coordinate system. For a fixed observer near the rotor plane, this results in a force that changes direction periodically, generating a sound wave. The frequency of this sound wave corresponds to the frequency at which a blade passes that point, known as the blade passing frequency $BPF = Bn$, where B represents the number of blades and n is the propeller rotational frequency in Hz. In many cases, the propeller operates in a unsteady inflow which cause a rapid change in loading and constituting a very efficient source of sound [17]. This situation occurs, for example, when a rotor is subject to blade vortex interaction [66]. Additionally, at low Reynolds numbers, the flow is highly sensitive to even minor changes in conditions, such as variations in angle of attack or irregularities in blade shape, which result in unsteady loading. Another source of tonal noise, less significant compared to loading noise at low blade-tip Mach numbers, is linked with the motion of the blade surface and is referred as *thickness noise*. As the rotor blade rotates, a fixed observer perceives a time-varying displacement

of air, which generates a sound wave in the far-field. In Fig. 2.1, loading and thickness noise are identified with the discrete frequencies at the BPF and its harmonics.

Broadband rotor noise is linked to disturbances that are inherently random, meaning they do not repeat exactly with each revolution. These disturbances typically result from the rotor's interaction with turbulence, which can be either ingested from the surrounding atmosphere or originate within the blade boundary layer and at the blade tip. The first case is common for a rotor since a blade can encounter the turbulent wake generated from the previous blade (*leading edge* or *turbulent impingement noise*) [1]. The second case represents an efficient noise source when a turbulent boundary layer develops over the blade, originating sound from the interaction of the airflow with the blades trailing edge (*turbulent boundary layer trailing edge noise*) [19]. At low Reynolds numbers, however, the boundary layer typically remains laminar, making it susceptible to flow separation, which in turn leads to vortex shedding. The resulting noise spectrum shows a broadband part along with a series of tonal peaks (*laminar boundary layer vortex shedding noise*) [38], as shown in Fig. 2.1. It's important to note that vortex shedding tones have been documented for steady wings, but this phenomenon remains an open question for rotors, where variations in angle of attack along the blade can significantly impact noise generation. Addressing this aspect will be a focus of the thesis. //

The primary mechanisms responsible for propeller noise generation have been summarized above. In the following sections, prior to exploring these noise sources in more detail, a comprehensive understanding of low-Reynolds number airfoil aerodynamics, particularly focusing on boundary layer dynamics, will be presented.

2.2. LOW-REYNOLDS AIRFOIL BLADE AERODYNAMICS

MOST of the researchers in the last decades focused on studying the flow around large-scale airfoils operating at relatively high chord Reynolds numbers Re_c above 10^6 (where $Re_c = \rho U_\infty c/\mu$ with ρ being the fluid density, U_∞ the free-stream flow velocity and μ the dynamic viscosity), to improve their aerodynamic efficiency. The methodologies developed in these studies are inadequate for airfoils operating at low Reynolds numbers, i.e. $Re_c < 5 \cdot 10^5$, because of the predominance of the viscous effects compared to the inertial ones. The dependence of the airfoil´s aerodynamic characteristics from the Reynolds number at which it operated is known as *scale effect*.

A common parameter to evaluate the effectiveness of an airfoil is given by its maximum lift-to-drag ratio $(c_L/c_D)_{max}$. As shown in Fig. 2.2, for conventional "smooth" airfoils there is a critical Re_c of approximately $7 \cdot 10^4$ below which $(c_L/c_D)_{max}$ quickly deteriorates [31]. Interestingly, a rough airfoil (or an airfoil equipped with a turbulator) does not show this sudden drop in aerodynamic performance. Additionally, below $Re_c = 10^5$ the aerodynamic performance of a thin flat plate is higher than a conventional airfoil and invariant to the Reynolds number. This is investigated by Winslow et al. [62], who compare the flow characteristics around a NACA 0012 airfoil and a flat plate (2% chord thickness) at a $Re_c = 2 \cdot 10^4$. For angles of attack ranging from 0° to 5°, the NACA 0012 airfoil experiences significant trailing-edge separation, leading to reduced lift due to a reduction in suction peak. In contrast, the flat plate does not exhibit separation at its trailing edge. Rather, the flow separates at the sharp leading edge and subsequently reattaches to the plate's surface.

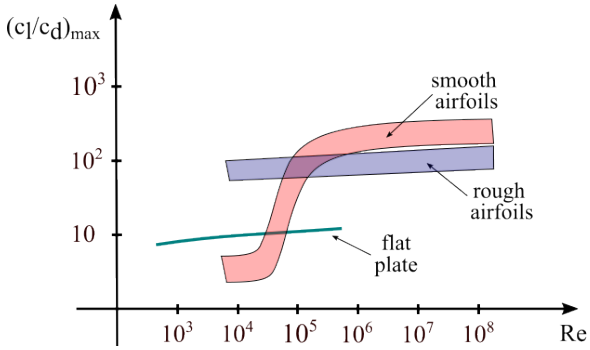

Figure 2.2: Variation of maximum lift-to-drag ratio with Reynolds number. Adapted from [31].

2.2.1. BOUNDARY LAYER BAHAVIOUR

All the airfoils create a region of accelerated flow and low pressure. The accelerated flow must return to free-stream conditions, hence experiencing an adverse pressure gradient ($dp/dx > 0$). For high Reynolds numbers, the boundary layer most likely undergoes turbulent transition beforehand. A turbulent boundary layer can withstand severe adverse pressure gradients without separating. At low Reynolds numbers instead, the boundary layer is usually still laminar when it encounters an adverse pressure gradient and it is much less capable of resisting separation. Consequently, the aerodynamic performance of the airfoil are dictated by the complicated boundary layer evolution, involving phenomena such as laminar separation, transition of the separated shear layer from laminar to turbulent flow and possible reattachment [62, 16, 53].

At Re_c in the range of approximately $5 \cdot 10^4$ to $5 \cdot 10^5$ and moderate angles of attack the boundary layer on the airfoil is initially laminar but, due to a strong pressure gradient, a laminar separation usually occurs (see Fig. 2.3). The separated shear layer, gaining momentum from the freestream, undergoes turbulent transition and reattaches on the airfoil surface, forming a laminar separation bubble (LSB) [27]. As shown in Fig. 2.3 the LSB length corresponds to the distance between the laminar separation point (S) and the turbulent reattachment (R) point. Within the LSB, the flow is recirculating and its velocity is significantly reduced compared to the free-stream velocity. The bottom of Fig. 2.3 illustrates a typical behaviour of the surface pressure coefficient c_P in the presence of a LSB. The separated flow creates a plateau (or slight increase) in the pressure [55] distribution. The transition of the separated shear layer from laminar to turbulent results in a sharp increase in pressure due to turbulent mixing. Finally, the shear layer reattachment is characterized by a gradual recovery of pressure. From the c_P distribution is possible to identify the position of the separation and transition points, marked by the start and end of the pressure plateau, respectively, and the reattachment point as the end of the region of rapid pressure rise [34]. Consequently, the LSB length can also be calculated from the pressure coefficient plot.

At lower Re_c, typically ranging from 10^4 to $5 \cdot 10^4$, and low angles of attack, a laminar separation is still present but the separated shear layer may be unable to reattach.

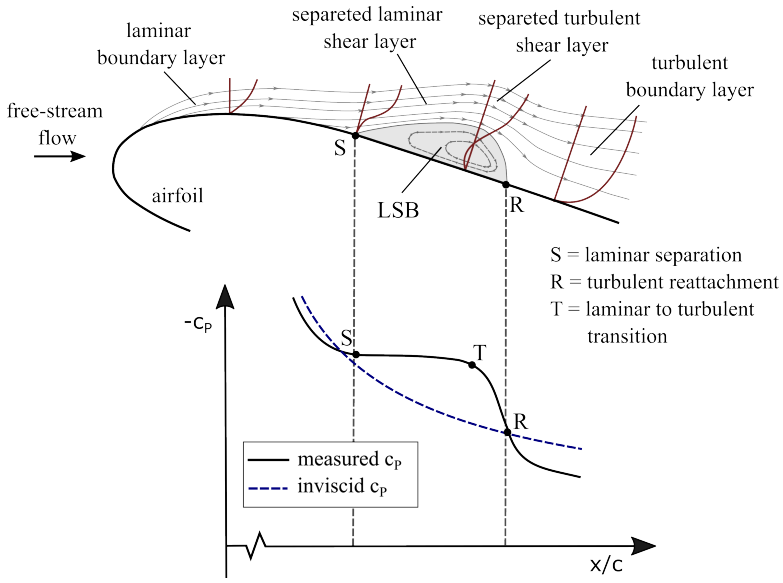

Figure 2.3: Schematic of a laminar separation bubble and corresponding surface pressure distribution.

This condition is often indicated as "bubble bursting" and referred as "long bubble". Therefore, the airfoil is effectively in trailing edge stall. If the angle of attack is further increased, a LSB is formed.

The position and size of the LSB vary based on factors such as airfoil shape, angle of attack, Reynolds number and free-stream turbulence. The sketch in Fig. 2.4 illustrates the general trends of the separation and reattachment points versus the angle of attack, for varying Reynolds numbers ($Re_{c1} < Re_{c2} < Re_{c3}$). As the angle of attack, or Reynolds number, increases, the LSB moves toward the leading edge and decreases in length [7]. This shortening of the LSB with increasing angle of attack and Reynolds number is due to an upstream shift of both the separation and reattachment points. The movement of the separation point exhibits a more gradual change. The upstream movement of the LSB continues until transition and separation points coincide at the leading edge, leading to the burst of the bubble. There is a minimum angle of attack at which the LSB starts forming, which decreases with the Reynolds number. Indeed, for the three Re_c represented in Fig. 2.4 the reattachment curve starts from a different α. As an example, the right side of the figure shows the flow conditions around the airfoil corresponding to two angles of attack α_1 and $\alpha_2 > \alpha_1$ for Re_{c1} and Re_{c3}. For Re_{c1}, the flow is separated at α_1 and a LSB is formed at α_2. For Re_{c3} instead, a LSB is present for both angles of attack and decreases in size (while moving upstream) when α increases from α_1 to α_2.

Bastedo et al. [5] studied the flow characteristics over a Wortmann FX63-137 airfoil at $Re_c = 8 \cdot 10^4$ and $2 \cdot 10^5$. In the first case, the LSB bursts for angles of attack less than 6°, whereas for $\alpha > 6°$ a short bubble is formed. In the second case, a LSB is present from $\alpha = -7°$ to 21°, where it bursts. Park et al. [37] showed that the flow over a DAE51 airfoil at $Re_c = 3.9 \cdot 10^4$ does not reattach up to $\alpha = 10°$. Finally, the study of [65] et al.

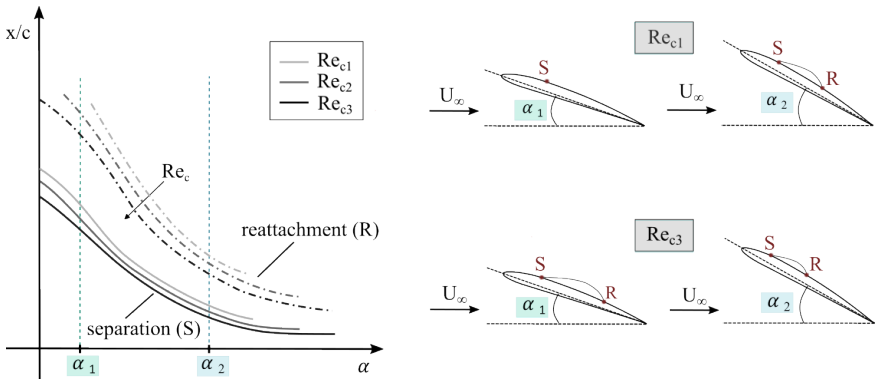

Figure 2.4: Chordwise locations of separation and reattachment points with respect to the angle of attack (for varying Reynolds numbers).

showed a similar trend for a NACA0025 airfoil: at $\alpha = 5°$ and $Re_c = 5.5 \cdot 10^4$ a boundary layer separation without reattachment is observed, when the Reynolds is increased to 10^5 a LSB is formed. For a given airfoil, the lowest angle of attack at which the LSB forms is strongly dependent on the Reynolds number.

To summarize, the presence of an adverse pressure gradient is a necessary but not sufficient condition for the formation of an LSB. A sufficiently high Re_c will cause the boundary layer to transition from laminar to turbulent before the theoretical laminar separation point, preventing the formation of a LSB. Conversely, when the Re_c is sufficiently low, the boundary layer fails to reattach after separation. Thus, the LSB exists only within a certain range of Reynolds numbers. Tani [55], based on experimental evidence, postulated that the reattachment occurs if Re_θ (Reynolds number based on the boundary layer momentum thickness) at the separation exceeds a critical value of 210. Owen et al. [36] found instead that the reattachment occurs if Re_δ (Reynolds number based on the boundary layer displacement thickness) exceed the range 400-500.

The presence of a LSB results also in significant variations in integral boundary layer parameters. Brandel and Muller [9] showed that, for an airfoil at $Re_c = 10^5$, the displacement thickness increases rapidly following a laminar separation, then decreases at transition onset. The momentum thickness grows at a nearly identical rate after a separation and suddenly increases near the transition location. Kim et al. [22] observed overall a similar trend for the displacement thickness on an airfoil at a maximum $Re_c = 4.8 \cdot 10^4$, although they noted that the transition point is located slightly downstream from the point of maximum displacement thickness.

2.2.2. LIFT AND DRAG CHARACTERISTICS

The boundary layer features outlined in Sect. 2.2.1 have a significant influence on the lift and drag characteristics of low Reynolds numbers airfoils. The lift and drag polars exhibit the following common features:

- high non-linearity

- decrease of maximum lift and increase of minimum drag (with respect to high Reynolds number cases)
- hysteresis

For airfoils at Reynolds numbers exceeding 10^5, the drag and lift polars are nearly insensitive to variations in Reynolds number. On the other side, experiments conducted on various airfoils at Reynolds numbers below 10^5 [31, 50] revealed a high degree of non-linearity in both drag and lift polars. The latter are particularly sensitive to changes in airfoil geometry and Reynolds number. Ohtake et al. [35], in their investigation on a NACA 0012 airfoil at Re = $3 \cdot 10^5$, showed a significant deviation of the lift-curve slope from the value predicted by the thin wing theory [3], demonstrating that a single slope assumption cannot be made. This is attributed to the complex flow separation characteristics on the suction side of the airfoil. For an angle of attack between 0° and 8° a separation bubble is observed. As the angle of attack is increased, the bubble moves toward the leading edge, changing the position of the laminar-to-turbulent transition point. Above 8°, there is a simultaneous presence of trailing edge separation, culminating in the complete airfoil stall which occurs between 12° and 14°.

A lower Reynolds number typically results in reduced lift and markedly increased drag, as documented by Selig et al. [51], who measured the drag polars of over 60 airfoil types at Reynolds numbers between $5 \cdot 10^4$ and $5 \cdot 10^5$. The reduction in lift is primarily due to a decrease in the suction peak, while the significant increase in drag is caused by the early separation of the boundary layer. Sheldhal et al. [52] measured 46% of maximum lift coefficient $c_{L_{max}}$ reduction for a TURNS2D airfoil when Re_c is decreased from 10^5 to 10^4. Winslow et al. [62] found instead a 23% drop in $c_{L_{max}}$ for a NACA0012 airfoil subject to a Re_c reduction from 10^6 to 10^5.

Typical trends for the lift and drag polars at three Reynolds numbers ($Re_{c1} < Re_{c2} < Re_{c3}$) are sketched in Fig. 2.5. At the highest Reynolds number Re_{c1}, the slope of c_L decreases with increasing α because of the movement of the LSB toward the leading edge, which reduces the suction peak. The abrupt decrease in lift and increase in drag corresponds to the bubble bursting. The polars at Re_{c2} show a similar behaviour, but the bubble bursts earlier because of the lower Reynolds number. Finally, at the lowest Reynolds number (Re_{c3}), the bubble burst at low α and the large region of separated flow dramatically decrease the lift and increase the drag.

Aerodynamic hysteresis refers to the phenomenon by which the aerodynamic characteristics, such as lift and drag coefficients, are loading history-dependent, i.e. exhibit different behaviour depending on the direction of change of the angle of attack. It's important to note that this phenomenon occurs under steady-state conditions and differs from the hysteresis associated with the pitching motion of an airfoil, which involves rapid changes in lift and drag coefficients due to unsteady flow conditions [28]. Hu et al. [20] found for a NASA low-speed GA-(W)-1 airfoil at $Re_c = 1.6 \cdot 10^5$ a clockwise hysteresis loop for c_L and counterclockwise for c_D, for α between 13° and 15°. Depending on whether the angle of attack is increasing or decreasing, c_L (c_L/c_D) at $\alpha = 14°$, was found to be 1.33 (23.5) and 0.80 (3.66), respectively. In the former case ($\alpha = 14°$ on the increasing angle branch), the flow over the airfoil suction side exhibited a separation followed by a reattachment, i.e. a LSB is formed. Conversely, in the latter case ($\alpha = 14°$ on the

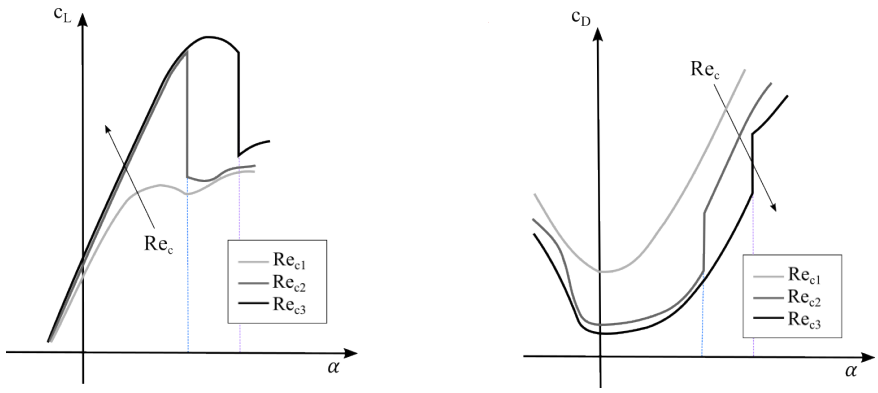

Figure 2.5: Trend of c_l and c_d polars for varying Reynolds numbers.

decreasing branch) the airfoil experienced stall. The strong reverse flow from the airfoil trailing edge prevented the flow from reattaching on the airfoil suction side. In essence, inside the hysteresis loop, the aerodynamic characteristics are determined not only by the current flow conditions but also by its past history.

Muller [30] demonstrated that the hysteresis loop in the lift coefficient can be both clockwise and counterclockwise, depending on the characteristics of the airfoil boundary layer. If there is laminar separation without reattachment as α is increases, a counterclockwise hysteresis occurrs (with c_L higher for decreasing α). Conversely, if transition, such as that caused by a LSB, occurs during increasing α, the resulting hysteresis is clockwise (c_L is higher for decreasing α). Note that a clockwise hysteresis for the lift force corresponds to a counterclockwise hysteresis for the drag force, and vice-versa. The aerodynamic measurements conducted by Muller [30] on a Miley M06-13-128 airfoil exhibit a clockwise hysteresis in the lift coefficient at a chord Reynolds number ranging between $7 \cdot 10^4$ and $1.5 \cdot 10^5$. As α increases whithin the hysteresis loop (between 10° and 17°), there is a LSB on the airfoil upper side that moves toward the leading edge. Decreasing α from about 20° results in a higher lift because, in this case, transition occurs downstream of the maximum thickness point, allowing the boundary layer to stay attached almost to the trailing edge.

2.2.3. GENERATION OF COHERENT STRUCTURES

The separated shear layer which develops over an airfoil at low Reynolds number is inherently unstable and undergoes laminar to turbulent transition (as explained in Sect. 2.2.1) due to the amplification of flow disturbances. Boutilier et al. [8] attributed the primary amplification mechanism for these disturbances to the inviscid Kelvin Helmholtz instability. The growing instabilities cause the shear layer to roll-up and form vortices that are shed into the airfoil wake. The characteristics of these vortices depend on the pressure distribution over the airfoil and ultimately on the airfoil geometry, angle of attack and Reynolds number.

Yarusevych et al. [65] investigated two flow regimes over a NACA 0025 airfoil at $\alpha = 5°$: (a) boundary layer separation without reattachment, i.e. bubble bursting ($Re_c = 5.5 \cdot 10^4$

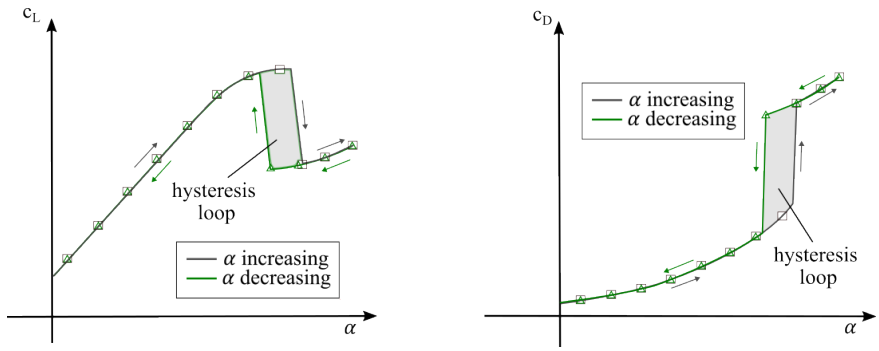

Figure 2.6: Hysteresis loop for lift (left) and drag (right) coefficients.

and 10^5) and (b) LSB formation ($Re_c = 1.5 \cdot 10^5$). The flow visualizations corresponding to these two flow regimes, shown in Fig. 2.7, exhibit a different wake development. In case (a), the vortices originate from the roll-up of the separated shear layer, forming a Kármán-type vortex street in the wake. In case (b), the vortices are visible only in the wake, exhibiting lower coherence and smaller length scales.

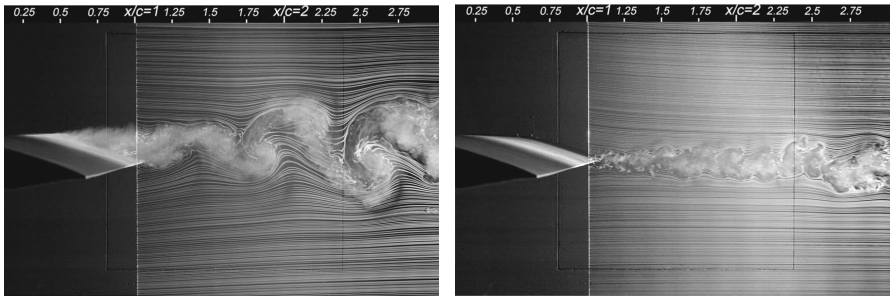

(a) (b)

Figure 2.7: Flow visualizations around a NACA 0025 airfoil at $\alpha = 5°$: (a) $Re_c = 5.5 \cdot 10^4$, (b) and $Re_c = 1.5 \cdot 10^5$ [65].

The impact of Reynolds number on vortex shedding characteristics is further explored by Yarusevych et al. [65] through spectral analysis of the boundary layer and wake at an angle of attack $\alpha = 5°$ and varying Reynolds numbers. Figure 2.8 depicts the Strouhal number $St_s = f_s d / U_0$, based on the vortex shedding frequency f_s and the length of the airfoil projection on a cross-stream plane d, as a function of Reynolds number. For the lower Reynolds number branch, corresponding to boundary layer separation without reattachment, St_s remains approximately constant and is similar to the value found for vortex shedding behind a cylinder, which is 0.21 [48]. In contrast, for the higher Reynolds number branch, corresponding to laminar separation bubble (LSB) formation, St_s exhibits a sharp increase starting from a value of 0.63.

The formation of vortex structres from a separated shear layer is also studied numerically. Pauley et al. [39] and Riplay et al. [45] found the occurrence of vortex shedding for

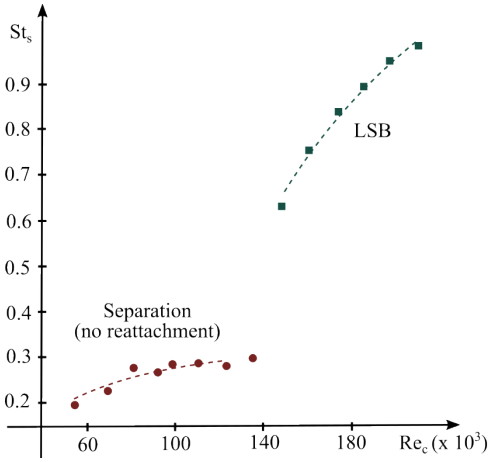

Figure 2.8: Strouhal number St_s based on the vortex shadding frequency as a function of the Reynolds number for a NACA 0025 at $\alpha = 5°$. Adapted from [65].

a flat plate with externally applied adverse pressure gradient. Lin et al. [27] conducted numerical simulations on an Eppler 387 airfoil at low Reynolds number. They showed the presence of large-scale structure, in the form of vortex shedding, originating from the separated shear layer. When the Reynolds number is decreased, vortex pairing take place, increasing the length scale of the shed vortices. [8]. Ribeiro et al. conducted high-fidelity direct numerical simulations (DNS) on a NACA0012 airfoil at $Re_c = 5 \cdot 10^4$ and revealed intriguing near-wall dynamics, characterized by intermittent vortex shedding originating from the LSB. Visualization of instantaneous spanwise vorticity illustrates various patterns of structures shed from the LSB, which can be single vortices that maintain coherence up to the trailing edge (see Fig. 2.9 right), or pairs of coherent vortices, as well as counterparts that break down into smaller-scale turbulent structures (see Fig. 2.9 left).

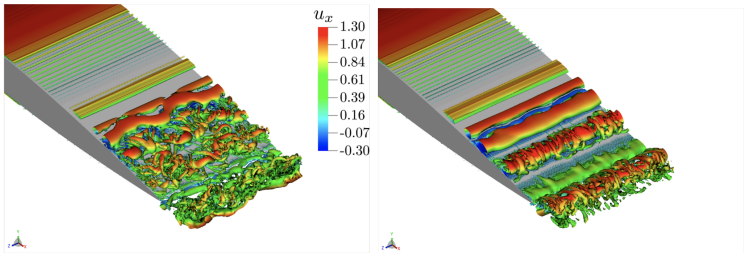

Figure 2.9: Isosurfaces of λ_2 criterion (colored by the streamwise velocity u_x) for a NACA0012 airfoil at $Re_c = 5 \cdot 10^4$ and $\alpha = 3°$ illustrate uncoherent turbulent structures (left) and spanwise coherent structures (right) [44].

2.3. AIRFOIL BLADE SELF-NOISE

This section addresses airfoil self-noise, which refers to the noise generated from the interaction between the airfoil blade and the turbulence produced in its own boundary layer and near wake [10]. Among the various mechanisms, this section will emphasize those most relevant to the study. At low Reynolds numbers, the boundary layer over most of the blade is expected to remain laminar (see Sect. 2.2), hence the discussion will focus on the noise mechanisms linked to a laminar boundary layer, specifically vortex shedding noise. However, in some areas of the blade, particularly near the tip where the Reynolds number increases, the boundary layer may completely transition from laminar to turbulent. Therefore, an illustration of trailing edge noise (linked to a turbulent boundary layer) will also be included. Other mechanisms, considered less significant for this study, will be briefly mentioned.

2.3.1. LAMINAR BOUNDARY LAYER VORTEX SHEDDING (LBL-VS) NOISE

The study by Paterson et al. [38] was among the first to characterize the effects of vortex shedding from an airfoil on far-field noise spectra. Conducting experiments on NACA airfoils for varying Reynolds numbers, they found that a strong tonal component appears in the noise spectra when vortex shedding occurred. Fig. 2.10 represents the Re_c-α region in which tones were measured for NACA 0012 and 0018 airfoils. The range of Reynolds numbers over which tones were measured expanded with increasing angles of attack and, for the NACA 0018 airfoil, the tonal regime extends to higher angles of attack due to delayed stall. Furthermore, the researchers demonstrated that the frequency of the observed tones exhibits a "ladder-type" behaviour (see Fig. 2.11): locally the frequency increases as $U_\infty^{0.8}$ and, at certain velocities, it abruptly jumps to higher frequencies, again following a $U_\infty^{0.8}$ power relationship with the velocity. The overall trend of the tone frequency, determined by fitting a straight line through all data points, follows a 3/2 power law of the free-stream velocity, resulting in $f \propto U_\infty^{1.5}$. At certain velocities, multiple discrete frequencies were detected, although the cause remained unknown.

Arbey and Bataille [4] shed more light on the presence of multiple tones. They showed that, in presence of airfoil vortex shedding, the spectrum of the radiated noise consists of a broadband hump, centered at a frequency f_s, and a dominant (or central) tone, at a frequency $f_{n_{MAX}}$, surrounded by a series of regularly spaced tones at frequencies f_n (see Fig. 2.12). Regardless the airfoil used, they found that the peak frequency of the broadband contribution f_s follows Paterson´s $U_\infty^{1.5}$ law [38]:

$$f_s = k\sqrt{Re_c} = k\frac{U_\infty^{1.5}}{(c\nu)^{1/2}} \tag{2.1}$$

where ν is the kinematic viscosity of the fluid and $k = 0.011$. The broadband contribution results from the diffraction of the hydrodynamic fluctuations induced by the instability of the boundary layer (also found by Fink [15]).

ACOUSTIC FEEDBACK LOOP

The frequency selection for the discrete tones f_n is linked to the concept of "feedback loop". This concept was first introduced by Tam [54], as an aerodynamic, self-excited feedback mechanism, which establishes between the airfoil trailing edge (point A) and

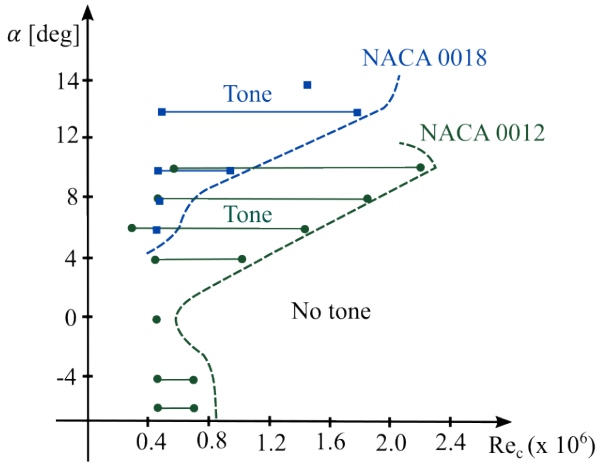

Figure 2.10: Vortex shedding noise regimes for NACA 0012 and 0018 airfoils (adapted from Paterson et al [38]). For each α, the markers and solid lines indicate the Reynolds range over which tonal noise was measured.

a point in the wake (point B), followed by Wright [64]. According to Tam, disturbances originate at the sharp trailing edge and amplify as they travel into the wake. Once they reach a sufficient magnitude, they cause lateral vibrations in the wake, resulting in the emission of acoustic waves. Part of these waves propagate upstream to the trailing edge, inducing oscillations in the boundary layer. In order for the loop to be self-sustaining, the acoustic and hydrodynamic signals must be in phase at point A. This means that the total change in phase over the feedback loop has to be equal to an integer multiple of 2π. By denoting L as the length of the feedback loop, i.e. the distance between A (point of receptivity) and B (noise source location), the phase condition is expressed by the following equation:

$$2\pi f_n L\left(\frac{1}{u_c}+\frac{1}{c_0}\right)=n2\pi \tag{2.2}$$

where u_c and c_0 are the convective velocity of the instability waves in the wake and the speed of sound, respectively and n is an integer that identifies the n-th tone. The two terms on the left side of the equation represent the phase change of the convecting instability waves ($2\pi f_n L/u_c$) and the upstream propagating acoustic waves ($2\pi f_n L/c_0$). Solving for f_n:

$$f_n=\frac{n}{L}\left(\frac{1}{1/u_c+1/c_0}\right) \tag{2.3}$$

Subsequently, Arbey and Bataille [4] introduced modifications to Tam's feedback loop concept. They suggested that the aerodynamic instabilities develop within the bound-

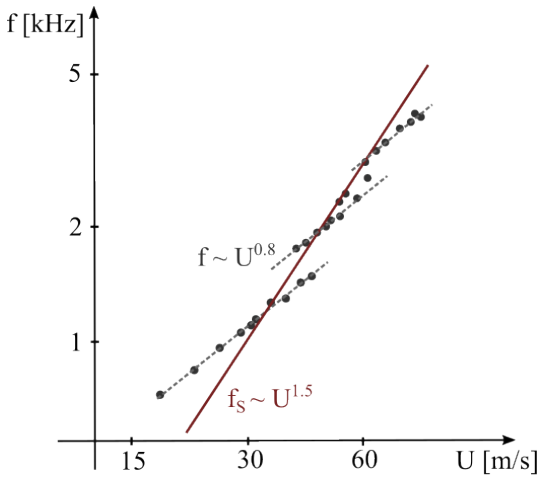

Figure 2.11: Trend of vortex shedding tone frequencies. Adapted from Paterson et al. [38].

ary layer and considered the feedback loop length to be the distance between the point of maximum velocity and the trailing edge. Additionally, they revised Tam's phase condition, deriving the following equation:

$$f_n = \frac{1}{L}\left(n+\frac{1}{2}\right)\left(\frac{1}{1/u_c + 1/(c_0 - U_\infty)}\right) \tag{2.4}$$

The differences from Eq. 2.3 include substituting n with $\left(n+\frac{1}{2}\right)$, which corresponds to a phase difference of π over the feedback loop, providing better agreement with the data of Arbey and Bataille. Additionally, a convection velocity correction is applied to the sound speed, using $(c_0 - U_\infty)$. Arbey and Bataille proposed also the following empirical relation for the frequency selection of tones:

$$f_n = \left(n+\frac{1}{2}\right)\frac{K}{L}U^{0.85} \tag{2.5}$$

where K is an empirical constant. The "ladder-type" behaviour introduced by Paterson can be explained by the analysis of Eqs. 2.1 and 2.5. As the flow velocity U_∞ increases, both f_s and f_n rise, but at different rates. When U_∞ reaches a point where f_s equals f_n, this shared value becomes the dominant frequency of the spectrum, making $f_n = f_{n_{MAX}}$. Hence, $f_{n_{MAX}}$ is a discontinuous function of the flow velocity. There is no consensus on the precise location where the feedback loop is closed. As mentioned above, Arbey and Bataille [4] proposed that it is at the point of maximum velocity, while Nash et al. [33] suggests it is located at the half chord point. In contrast, Nakano et al. [32] and Chang et al. [13] argue that it is at the point where boundary layer instabilities originate.

The physics of the feedback loop is further elucidated in the more recent work of Pröbsting and Yarusevych [42] by the help of flow visualizations. They demonstrated that tonal noise is generated by the passage of coherent vortical structures, formed over

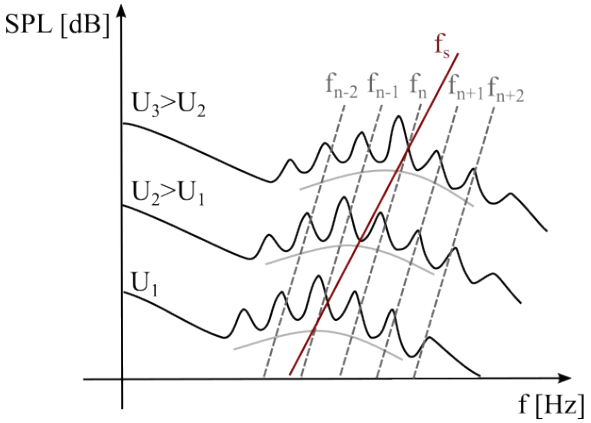

Figure 2.12: Example of acoustic spectra due to vortex shedding noise. Adapted from Pröbsting [40].

a LSB, as they travel over the trailing edge of the airfoil. The acoustic pressure waves, scattered at the trailing edge, propagate upstream and trigger the transition of the separated shear layer by amplifying disturbances and, hence, the shedding frequency, within a narrow frequency range. This creates a feedback loop between the trailing edge and the upstream location where hydrodynamic instabilities originate. A schematic illustration of this feedback loop mechanism is presented in Fig 2.13. As the Reynolds number increases, the vortical structures become less coherent, and the amplitude of the scattered acoustic waves at the trailing edge diminishes. Consequently, the amplification of disturbances occurs over a broader frequency range, as expected for natural transition.

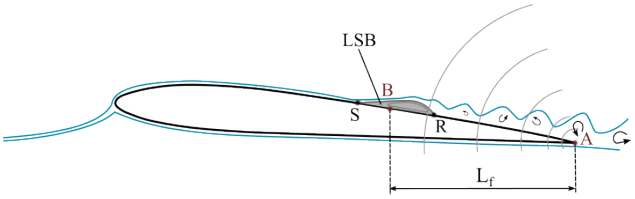

Figure 2.13: Schematic of a feedback loop originating at the suction side of the airfoil due to the generation of coherent vortices from a LSB.

Pröbsing et al. [41] carried out comprehensive acoustic measurements on a NACA 0012 airfoil with various boundary layer tripping devices applied to either the suction side, the pressure side, or both sides. The aim was to determine whether the generation of tonal noise is dominated by vortical structures originating from the suction side or the pressure side of the airfoil, referred to as suction side and pressure side events, respectively. The tripping device, which was made up of randomly distributed roughness elements, forced laminar-to-turbulent boundary layer transition, suppressing the generation of tones. Fig. 2.14 shows narrowband SPL spectra at $\alpha = 4°$ for two Reynolds

numbers. The case $Re_c = 0.6{\cdot}10^5$ represents a suction-side-dominated caseas evidenced by the disappearance of tones when tripping is applied to this side, whereas when Re_c is increased to $2.1 \cdot 10^5$ a transition to a pressure-side-dominated case is observed. The findings indicate the existence of a characteristic Reynolds number, Re_{ch} (dependent on the angle of attack α), such as if $Re_c < Re_{ch}$, tonal noise generation is primarily dominated by suction side events, whereas if $Re_c > Re_{ch}$, it is dominated by pressure side events. Additionally, there is an interaction between events from both sides, which becomes more significant at low angles of attack.

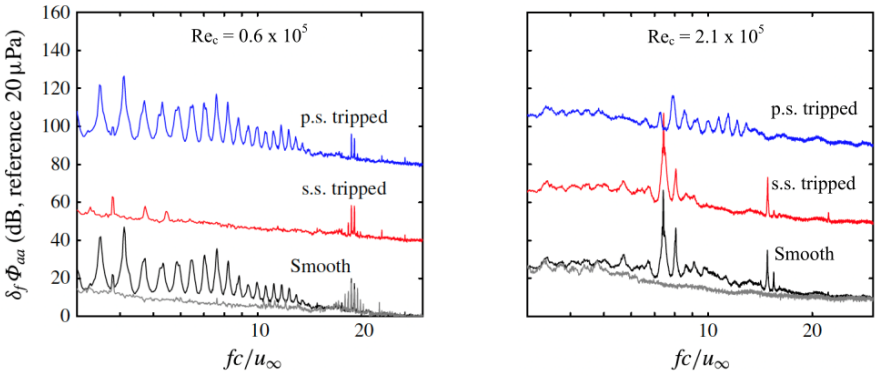

Figure 2.14: Narrowband SPL spectra for a NACA0012 at $\alpha = 4°$, shown for $Re_c = 0.6{\cdot}10^5$ (left) and $Re_c = 2.1{\cdot}10^5$ (right). An offset is applied to the cases with tripping. Adapted from Pröbsing et al. [41]

THE METHOD OF BROOKS, POPE AND MARCOLINI (BPM)

While the previously mentioned studies predict the frequencies of the multiple tones appearing in noise spectra due to airfoil vortex shedding, the only method currently available to estimate the tonal noise amplitude is the Brooks, Pope, and Marcolini (BPM) [11] semi-empirical model. In their research, BPM measured the airfoil self-noise of various NACA 0012 airfoils with different chord lengths under several wind tunnel speeds and angles of attack in an anechoic tunnel. From these measurements, they derived a spectral curve fit expressed as the SPL noise spectrum in 1/3 octave bands:

$$SPL_{LBL-VS} = 10\log\left(\frac{L\delta_p M^5 \overline{D_h}}{r_e^2}\right) + G_1\left(\frac{St'}{St'_{peak}}\right) + G_2\left[\frac{Re_c}{(Re_c)_0}\right] + G_3(\alpha) \qquad (2.6)$$

The first term of the equation is a scaling parameter that depends on the spanwise length of the airfoil L, the boundary layer thickness on the pressure side δ_p, the free-stream Mach number M, the directivity function for the high-frequency limit $\overline{D_h}$, and the absolute distance from the source to the observer r_e. The term G_1 defines the spectral shape in terms of the ratio of the Strouhal number St' (based on δ_p) to its peak value St'_{peak}. The term G_2 represents the peak scaled level shape curve, which depends on the chord-based Reynolds number Re_c and a reference Reynolds number $(Re_c)_0$, the latter being a function of the angle of attack α. Lastly, the term G_3 is a linear function of

α. The complete expressions for these terms can be found in Brooks et al. [11]. The BPM method is not limited to self-noise generated by vortex shedding; it also addresses other mechanisms such as trailing edge noise and stalled flow in a similar manner. Additionally, the model is commonly applied to airfoils other than the NACA0012 (as demonstrated by BPM in Appendix C of Ref. [11]), which can be achieved by using the boundary layer thickness calculated for the specific airfoil. However, this extrapolation may result in significant errors. In this work, the BPM model is utilized for the isolated propeller study of Chapter 5, extending its application to a rotating blade.

2.3.2. TURBULENT BOUNDARY LAYER TRAILING EDGE (TBL-TE) NOISE

At sufficiently high Re_c, the boundary layer over the airfoil blade fully transitions from laminar to turbulent, preventing the formation of a LSB (see the schematic illustration in Fig. 2.15). In this scenario, the boundary layer consists of a wide range of eddies of different sizes and strengths. When the turbulence-induced pressure fluctuations within the boundary layer encounter the sharp trailing edge, they undergo a sudden change in boundary conditions, resulting in the scattering of sound. Because of the random and chaotic nature of turbulence within the boundary layer, the resulting far-field noise spectrum is typically broadband.

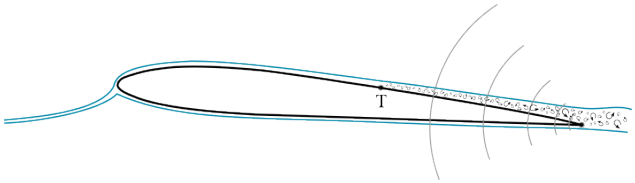

Figure 2.15: Schematic illustrating the mechanism of turbulent boundary layer trailing edge noise. The point labeled "T" indicates the location of the laminar-to-turbulent transition.

Ffowcs Williams and Hall [61] addressed the trailing edge noise problem by modelling the trailing edge as a semi-infinite flat plate of zero thickness immersed in a uniform turbulent flow of mean velocity U and sweep angle Λ_0, as sketched in Fig. 2.16. This approximation, which disregards the airfoil's leading edge, is valid if the airfoil chord is large compared to the acoustic wavelength of the radiated sound (non-compact surface). They employed an analytic, tailored Green function (which satisfied the rigid wall boundary condition on the flat plate) to solve Lightill's equation and characterize the acoustic pressure fluctuation scattered at the trailing edge. They hence found that the far-field noise spectrum scale scale as:

$$S_{pp}(\mathbf{x},\omega) \propto \frac{\rho_0^2 U^3 u^2 L b \cos^2(\Lambda_0)\sin(\phi_x)\cos^2(\theta_x/2)}{|\mathbf{x}|^2 c_\infty} S(\omega) \tag{2.7}$$

where ω is the angular frequency, $\mathbf{x}$ is the observer position, ρ_0 is the undisturbed fluid density, u is the velocity scale of the turbulent fluctuations (scaling as U), b is the trailing edge span, L is the length scale of the turbulent eddies, ϕ_x and θ_x are the observer angles measured from the edge and form a plate in a plane perpendicular to the edge,

respectively, and $S(\omega)$ is the two-point velocity cross spectrum. Equation 2.7 shows that trailing edge noise scales as the fifth power of flow velocity ($\sim u^5$). At low Mach number, the noise generated in the presence of a surface is higher than that generated in an unbounded medium, which scale with the eight power of the flow velocity ($\sim u^8$) [26]. The term $\cos^2(\theta_x/2)$ indicates that, in a plane normal to the trailing edge, the source has a cardioid directivity. This results in maximum radiation in the upstream direction and no radiation downstream. Another significant term in Eqn. 2.7 is $\cos^2(\Lambda_0)$, which reveals that the noise scattering is more efficient if the turbulent eddies travel perpendicular to the trailing edge ($\Lambda_0 = 0°$). The most intriguing findings from the Ffowcs Williams and Hall's equation are the noise scaling and directivity patterns. However, a significant limitation for conducting a more in-depth analysis is the complex estimation of the two-point velocity cross spectrum $S(\omega)$.

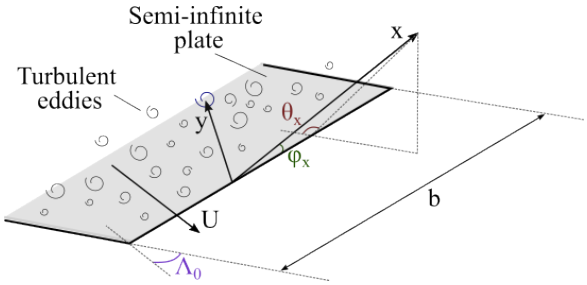

Figure 2.16: Geometry of a semj-infinite flat plate immersed in a turbulent flow with mean velocity U and sweep angle Λ_0.

Several years later, Amiet [2] modeled the trailing edge noise problem by considering a pressure disturbance traveling over a semi-infinite flat plate. The analysis assumes that the turbulence remains statistically identical as it moves past the trailing edge. The scattered pressure field at the trailing edge, determined based on Schwartzschild's solution [49], is an irrotational response caused by a change of boundary conditions and the imposition of the Kutta condition (at the trailing edge). One of the strengths of Amiet's formulation is that well-established empirical expressions can be used to calculate the surface pressure spectrum near the trailing edge. Amiet's results are consistent with those obtained by Ffowcs Williams and Hall. Roger and Moreau [46, 29] revisited Amiet's work by incorporating a leading edge back-scattering correction to account for compact chord effects. Additionally, Roger and Moreau introduced 3D gusts to predict far-field radiation for a receiver located off the mid-span plane.

Finally, the BPM [11] method introduced in Sect. 2.3.1 also accounts for turbulent boundary layer trailing edge noise. In this case the SPL spectrum in 1/3 octave bands can be expressed as follows:

$$SPL_{TBL-TE} = 10\log\left(10^{(SPL_p/10)} + 10^{(SPL_s/10)} + 10^{(SPL_\alpha/10)}\right) \tag{2.8}$$

where SPL_p and SPL_s denote the contributions from the pressure and suction side boundary layers, respectively, while SPL_α represents an additional contribution from a sepa-

rated portion of the boundary layer on the suction side of the airfoil. The complete expressions for these terms are provided in Brooks et al. [11]. Glegg and Devenport [18] provide a comparison of predictions for a NACA 0012 at zero angle of attack using both the BPM and Amiet models. The two models show a satisfactory agreement above 1 kHz, with a more considerable discrepancy at lower frequencies.

2.3.3. BOUNDARY LAYER SEPARATION AND STALL NOISE

At sufficiently high angles of attack, the boundary layer over the airfoil blade separates and can no longer remain attached to the surface. As the angle of attack increases further, the flow becomes highly separated or stalled, resulting in a notable drop in lift and a rise in drag. Research on noise associated with separated flow compared to TBL-TE noise is limited. However, Fink and Baley showed that, in stall conditions, noise levels increase by over 10 dB relative to TBL-TE noise. According to the semi-empirical model by Brooks et al. [10], the far-field noise spectrum for separated flow is marked by a spectral hump at mid- to high frequencies, attributed to the scattering of relatively small and coherent vortices separating from the airfoil surface.

Turner and Kim [57] studied the airfoil self-noise generated by a NACA0012 at $Re_c = 5 \cdot 10^4$ at $\alpha = 5°$, $10°$ and $15°$. At $\alpha = 10°$, the flow shows signs of separation, while at $\alpha = 15°$ is fully stalled. At low frequencies, both of these angles of attack exhibit noise increase of up to 20 dB compared to $\alpha = 5°$. Moreover, narrowband peaks emerge in the full stall case, with the dominant peak linked to von Kármán vortex shedding in the wake. In fact, vortical structures form within the separated shear layer and travel to the trailing edge, where they pair and generate a Kármán vortex street that sheds into the wake. These structures cause strong pressure fluctuations on the wall as they convect towards the trailing edge before being scattered as a dipole pulse. This is in agreement with the stall mechanism described by Lacagnina et al [24].

2.4. ROTATIONAL NOISE

This section describes rotational noise, which encompasses all sound associated with the blade rotation and is characterized by discrete frequencies (tones) occurring at harmonics of the BPF [23]. Specifically, the section focuses on loading and thickness noise sources, which are related to the periodic variation of aerodynamic forces and displacement of air, respectively.

2.4.1. LOADING NOISE

Loading noise is generated by the time-varying pressure on a blade surface as it moves through the air. As mentioned in Sect. 2.1, from the perspective of a stationary observer, a steady pressure distribution in a blade-based reference system appears as unsteady due to the periodic changes of its component projected in the observer's direction, thus generating noise. Additionally, the pressure distribution over the blade typically includes an unsteady component in the blade-based reference system, contributing to noise generation. This unsteadiness can occur, for example, when the rotor operates in a distorted inflow or experiences blade vortex interaction. Loading noise can be calculated using the Ffowcs Williams and Hawkings (FW-H) equation [60], which provides the radiated

acoustic pressure as:

$$p'_L(\mathbf{x},t) = -\frac{\partial}{\partial x_i}\int_S \left[\frac{p_{ij}\hat{n}_j}{4\pi r\,|1-M_r|}\right]_{ret} dS(\mathbf{y}) \tag{2.9}$$

where $\mathbf{x}$ and $\mathbf{y}$ are the observer and source positions, respectively, r is equal to $|x-y|$, $\mathbf{n}$ is the surface normal (pointing outward) and M_r being the component of the source Mach number vector in the direction of the observer. The integral 2.9 needs to be computed on the entire blade surface but for thin blades, it can be simplified to an integral over the blade platform Σ (i.e. the projection into the rotor disk plane) [18]. Furthermore, taking into account the integral of $p_{ij}\hat{n}_j$ represents the surface loading f_i, it follows:

$$p'_L(\mathbf{x},t) = -\frac{\partial}{\partial x_i}\int_\Sigma \left[\frac{f_i(\mathbf{y},\tau)}{4\pi r\,|1-M_r|}\right]_{ret} d\Sigma(\mathbf{y}) \tag{2.10}$$

The subscript ret denotes that the integrand is computed at the retarded time, i.e. the emission or source time τ, and the noise is related to the variation of f_i over the blade platform as a function of the emission time τ. The integral 2.10 can be further manipulated by transforming the spatial derivatives into source time derivatives [14], obtaining:

$$p'_L(\mathbf{x},t) \approx \frac{1}{4\pi c_0}\int_\Sigma \left[\frac{x_i}{|\mathbf{x}^2|\,(1-M_r)^2}\left\{\frac{\partial f_i}{\partial \tau}+\frac{f_i}{(1-M_r)}\frac{\partial M_r}{\partial \tau}\right\}\right]_{ret} d\Sigma(\mathbf{y}) \tag{2.11}$$

where the noise signature is now related to the source time derivative of the loading and the source Mach number vector. The analysis of the result in Eq.2.11 highlights several interesting features. First, the loading near the blade tip generates most of the sound due to a higher rate of change of M_r, specifically $\partial M_r/\partial\tau$, at the tip. Secondly, the presence of an unsteady component in the loading significantly amplifies the far-field noise. Lastly, particularly for observers situated in the rotor plane, the frequency of the sound signature shifts during the blade's rotation due to the Doppler effect, which is represented by the term $(1-M_r)$ in the denominator. When the blades are moving away from the observer, the frequency is lower than the source frequency, while it is higher when the blades are approaching the observer.

2.4.2. THICKNESS NOISE

Thickness noise is generated by the time-varying displacement of air that occurs as the rotor blades move through the air. To a fixed observer, it appears as an apparent variation of blade volume, causing a sound wave generation. The thickness noise efficiency is related to the blade shape and thickness distribution along the radius. An expression for thickness noise is given by one of the terms of the FW-H equation [60] for an impermeable moving surface:

$$p'_T(\mathbf{x},t) = \frac{\partial}{\partial t}\int_S \left[\frac{p_0 v_j \hat{n}_j}{4\pi r\,|1-M_r|}\right]_{ret} dS(\mathbf{y}) \tag{2.12}$$

where v is the velocity of the integration surface S and the other quantities are the same of Eq. 2.9. Following the same approach described in Sect. 2.4.1, for thin blades the surface integral can be replaced by an integral over the blade platform Σ, obtaining:

$$p'_T(\mathbf{x},t) = -\frac{\partial}{\partial t}\int_S \left[\frac{p_0 \mathbf{v}\nabla h}{4\pi r\,|1-M_r|}\right]_{ret} d\Sigma(\mathbf{y}) \tag{2.13}$$

where $h = y_u + -y_l$ is the blade thickness (with y_u and y_l denoting the upper and lower surface coordinates, respectively) and $\nabla h = \nabla y_u - \nabla y_l$. This result highlights the dependence of the source strength on the blade thickness and not on the angle of attack or camber. Thickness noise produces a distinct pulse in the noise signature time history and, for high tip Mach number (typically greater than about 0.7), its level exceeds the one for steady loading noise. Additionally, thickness noise is mainly oriented along the rotor plane and can become considerable in rotors with a high blade count, where the load on each blade may be relatively low. However, it is often negligible for highly loaded rotors and in the presence of efficient unsteady loading noise sources. Generally, thickness noise can be reduced by decreasing the thickness of the blades in the tip area, with a reduction of 6 dB for every halving of blade thickness [18].

2.5. UNCONVENTIONAL ROTOR CONFIGURATIONS

After examining in the previous sections the aerodynamic characteristic of an airfoil blade at low-Reynolds numbers and investigating noise generation mechanisms for an isolated propeller, this section introduces the unconventional rotor configuration, specifically a co-rotating rotor, which will be further analyzed in Sect. 6.

Co-rotating rotors are a type of multi-rotor system for eVTOL aircraft, using two coaxial rotors. Coaxial rotors can be either counter-rotating, where the two rotors spin in opposite directions, and co-rotating rotors, where both rotors spin in the same direction. Unlike counter-rotating configurations, research on co-rotating setups is relatively limited. This concept can function as a lifting rotor and potentially offers quieter operation than traditional rotors, along with enhanced overall aerodynamic performance. Moreover, co-rotating systems mitigate the wake interference problem commonly associated with the noise generated by contra-rotating rotors [12, 63].

2.5.1. CO-ROTATING ROTORS

Co-rotating (or stacked) rotors are characterized by two rotors, connected to the same shaft, rotating in the same direction. They offer flexibility in adjusting the axial distance Δx between the rotors and the azimuthal separation $\Delta\phi$ between the propeller blades (also known as the phase or index angle). This design flexibility plays a crucial role in optimizing aerodynamic efficiency and reducing noise emissions, potentially surpassing the performance of isolated rotor configurations.

Most of the research on co-rotating focused on investigating the effect of the azimuthal and axial separations on aerodynamic performance and noise emission. Jacobellis et al. [21] observed a total thrust decrease by 10% as the azimuthal separation reached 0^o. Landgrebe et al. [25] carried out experiments with a small scale 2×3-bladed co-rotating rotor in hover and showed that, with azimuthal separations of 30^o and 45^o, improvements in thrust when compared to a co-planar configuration can be obtained. Rorke et al. [47], by testing a full-scale co-rotating rotor in hover with 4 different az-

Figure 2.17: Co-rotating rotor geometry: Δx and $\Delta\phi$ indicate the axial distance and azimuthal separation, respectively.

imuthal separations of 25.2°, 34.4°, 43.6° and 62.1°, measured 4 dB noise reduction at the first BPF for the 43.6° configuration and 6.1% thrust increase for 34.4° configuration. The latter was achieved by setting a differential collective pitch between the two rotors, with the upper rotor pitch angle being 1° higher than the lower one.

Tinney et al. [56] performed experiments on a 2×2-bladed co-rotating rotor in hover at several rotational speeds, showing that the rotor thrust and sound pressure levels are more dependent on the azimuthal than on the axial separation. Interestingly, they also found that various combinations of rotor speed and phase angle can produce the same rotor thrust but result in different sound pressure levels. The thrust trend as a function of azimuthal separation $\Delta\phi$ for different rotational speeds, as extrapolated from experimental data by Tinney et al. [56], is shown in Fig. 2.18. Table 2.1 summarizes the azimuthal separation $\Delta\phi$ at which maximum thrust was observed in the studies discussed above, along with the corresponding noise trends. These studies suggest that the optimal $\Delta\phi$ for both maximum thrust and minimum noise is influenced by several factors, including rotor number, axial distance, blade design, and rotational speed.

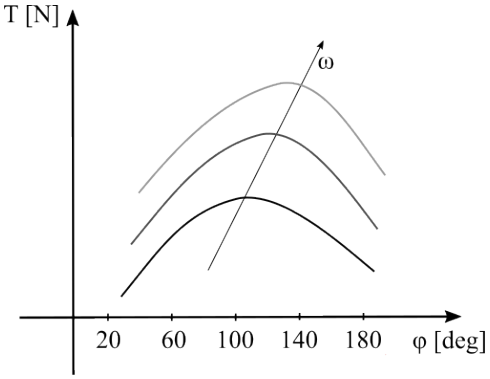

Figure 2.18: Thrust as a function of azimuthal separation $\Delta\phi$ for a 2×2 bladed co-rotating rotor at various rotational speeds, extrapolated from experimental data by Tinney et al. [56].

In a follow-up campaign, Valdez et al. [58] employed high-speed Schlieren and particle image velocimetry to study the wake on the same rotor configuration. The key finding is that the maximum thrust coefficient corresponds to the index angle where the tip vortex from the upper rotor is located above the suction (low-pressure) side of the lower rotor. As an example, Fig 2.19 presents a series of Schlieren images of the near-wake region of a co-rotating rotor configuration with $\Delta\phi = 120°$ at different wake ages. Red

markers trace the trajectory of the tip vortices. This technique highlights the complexity of the flow field around the blades, and at a wake age of 146°, it shows that the tip vortex from the upper rotor travels over the upper surface of the lower rotor.

Table 2.1: Azimuthal separation $\Delta\phi$ for maximum thrust in various co-rotating rotor studies and associated noise trends.

Study	**Rotor geometry**	$\Delta\phi[^\circ]$ **max thrust**	**Noise trend**
Tinney [56]	2 × 2-bladed	100–120	$\Delta\phi \uparrow$ OASPL $\downarrow$
Landgrebe [25]	2 × 3-bladed	30, 45	$\Delta\phi \uparrow$ OASPL $\downarrow$
Whiteside [59]	2 × 3-bladed	60	$\Delta\phi \uparrow$ OASPL $\downarrow$
Rorke [47]	2 × 3-bladed	43.6, 62.1	$\Delta\phi \uparrow$ OASPL $\downarrow$

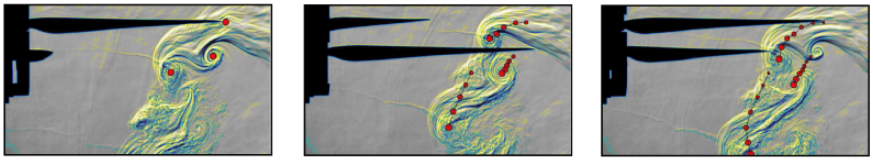

a) $\psi = 0^\circ$ (t = 0 ms) b) $\psi = 103^\circ$ (t = 4.08 ms) c) $\psi = 146^\circ$ (t = 5.7 ms)

Figure 2.19: Schlieren images of the near-wake region of a co-rotating rotor with $\Delta\phi = 120^\circ$ at different wake ages ψ. Red markers indicate the locations of the vortex cores, and the size of the markers decreases to denote previous vortex positions. Adapted from [58].

Landgrebe [25] and Tinney [56] conducted also experiments with different axial separations and they found that, as the axial separation increases, the thrust increases. This is probably related to a lower induced velocity at the lower rotor and a change in the blade-vortex interaction mechanism. A similar trend is obtained by other authors [6, 59, 43]. Conversely, the increase in thrust values corresponds to an increase in noise levels, which is in part related to an increase in loading noise.

BIBLIOGRAPHY

[1] Roy K Amiet. “Acoustic radiation from an airfoil in a turbulent stream”. In: *Journal of Sound and vibration* 41.4 (1975), pp. 407–420.

[2] Roy K Amiet. “Noise due to turbulent flow past a trailing edge”. In: *Journal of sound and vibration* 47.3 (1976), pp. 387–393.

[3] John D. Anderson. *Fundamentals of Aerodynamics*. 4th. New York: McGraw-Hill, 2007.

[4] H. Arbey and J. Bataille. “Noise generated by airfoil profiles placed in a uniform laminar flow”. In: *Journal of Fluid Mechanics* 134 (1983), pp. 33–47. DOI: 10.1017/S0022112083003201.

[5] William G Bastedo Jr and Thomas J Mueller. “Spanwise variation of laminar separation bubbles on wings at low Reynolds number”. In: *Journal of aircraft* 23.9 (1986), pp. 687–694.

[6] Mahendra Bhagwat. “Co-rotating and Counter-rotating Coaxial Rotor Performance”. In: *AHS Aeromechanics Design for Transformative Vertical Flight* (2018).

[7] Michael Boutilier and Serhiy Yarusevych. “Parametric study of separation and transition characteristics over an airfoil at low Reynolds numbers”. In: *Experiments in Fluids* 52 (June 2012). DOI: 10.1007/s00348-012-1270-z.

[8] Michael SH Boutilier and Serhiy Yarusevych. “Separated shear layer transition over an airfoil at a low Reynolds number”. In: *Physics of Fluids* 24.8 (2012).

[9] M. Brendel and T. Mueller. “Boundary-layer measurements on an airfoil at low Reynolds numbers”. In: *Journal of Aircraft* 25 (July 1988), pp. 612–617. DOI: 10.2514/3.45631.

[10] Thomas Brooks, Dennis Pope, and Michael Marcolini. “Airfoil self-noise and prediction”. In: *Nasa Reference Publication 1218* (Aug. 1989).

[11] Thomas Brooks, Dennis Pope, and Michael Marcolini. “Airfoil self-noise and prediction”. In: *Nasa Reference Publication 1218* (Aug. 1989).

[12] P Chaitanya, Phillip Joseph, SD Prior, and AB Parry. “On the optimum separation distance for minimum noise of contra-rotating rotors”. In: *Journal of Sound and Vibration* 535 (2022), p. 117032.

[13] Tze Pei Chong and Phillip Joseph. “An experimental study of tonal noise mechanism of laminar airfoils”. In: *15th AIAA/CEAS Aeroacoustics Conference (30th AIAA Aeroacoustics Conference)*. 2009, p. 3345.

[14] F. Farassat. “Linear Acoustic Formulas for Calculation of Rotating Blade Noise”. In: *AIAA Journal* 19.9 (1981), pp. 1122–1130. DOI: 10.2514/3.60051. URL: https://doi.org/10.2514/3.60051.

[15] Martin R Fink. “Prediction of airfoil tone frequencies”. In: *Journal of Aircraft* 12.2 (1975), pp. 118–120.

[16] Mustafa Genç, Kemal Koca, Halil Açıkel, Gökhan Özkan, Mehmet Kırış, and Rahime Yıldız. “Flow characteristics over NACA4412 airfoil at low Reynolds number”. In: *EPJ Web of Conferences* 114 (Jan. 2016), p. 02029. DOI: 10.1051/epjconf/201611402029.

[17] Stewart Glegg and William Devenport. *Aeroacoustics of low Mach number flows: fundamentals, analysis, and measurement*. Academic Press, 2017.

[18] Stewart Glegg and William Devenport. *Aeroacoustics of low Mach number flows: fundamentals, analysis, and measurement*. Academic Press, 2017.

[19] Michael S Howe. “Trailing edge noise at low Mach numbers”. In: *Journal of Sound and Vibration* 225.2 (1999), pp. 211–238.

[20] Hui Hu, Zifeng Yang, and Hirofumi Igarashi. “Aerodynamic hysteresis of a low-Reynolds-number airfoil”. In: *Journal of Aircraft* 44.6 (2007), pp. 2083–2086.

[21] George Jacobellis, Rajneesh Singh, Chloe Johnson, Jayant Sirohi, and Rob McDonald. “Experimental and computational investigation of stacked rotor performance in hover”. In: *Aerospace Science and Technology* 116 (2021), p. 106847.

[22] Dong-Ha Kim, Jae-hun Yang, Jo-Won Chang, and Joon Chung. “Boundary Layer and Near-Wake Measurements of NACA 0012 Airfoil at Low Reynolds Numbers”. In: Jan. 2009. ISBN: 978-1-60086-973-0. DOI: 10.2514/6.2009-1472.

[23] DW Kurtz and JE Marte. *A review of aerodynamic noise from propellers, rotors, and lift fans*. Tech. rep. Jet Propulsion Laboratory, California Institute of Technology, 1970.

[24] Giovanni Lacagnina, Paruchuri Chaitanya, Tim Berk, Jung-Hoon Kim, Phillip Joseph, Bharathram Ganapathisubramani, Seyed Mohammad Hasheminejad, Tze Pei Chong, Oksana Stalnov, Kwing-So Choi, et al. “Mechanisms of airfoil noise near stall conditions”. In: *Physical Review Fluids* 4.12 (2019), p. 123902.

[25] Anton J Landgrebe and E Dean Bellinger. “Experimental investigation of model variable-geometry and ogee tip rotors.[aerodynamic characteristics of variable geometry rotary wings]”. In: (1974).

[26] Michael James Lighthill. “On sound generated aerodynamically I. General theory”. In: *Proceedings of the Royal Society of London. Series A. Mathematical and Physical Sciences* 211.1107 (1952), pp. 564–587.

[27] J. Lin and L.L. Pauley. “Low-Reynolds-number separation on an airfoil”. In: *Aiaa Journal* 34 (Aug. 1996), pp. 1570–1577. DOI: 10.2514/3.13273.

[28] William J McCroskey. “Unsteady airfoils”. In: *Annual review of fluid mechanics* 14.1 (1982), pp. 285–311.

[29] Stéphane Moreau and Michel Roger. “Back-scattering correction and further extensions of Amiet’s trailing-edge noise model. Part II: Application”. In: *Journal of Sound and vibration* 323.1-2 (2009), pp. 397–425.

[30] Thomas J Mueller. “The influence of laminar separation and transition on low Reynolds number airfoil hysteresis”. In: *Journal of aircraft* 22.9 (1985), pp. 763–770.

[31] Thomas J Mueller and B JANSEN JR. “Aerodynamic measurements at low Reynolds numbers”. In: *12th Aerodynamic Testing Conference*. 1982, p. 598.

[32] T Nakano, N Fujisawa, and S Lee. “Measurement of tonal-noise characteristics and periodic flow structure around NACA0018 airfoil”. In: *Experiments in Fluids* 40 (2006), pp. 482–490.

[33] Emma C Nash, Martin V Lowson, and Alan McAlpine. “Boundary-layer instability noise on aerofoils”. In: *Journal of Fluid Mechanics* 382 (1999), pp. 27–61.

[34] MM O’meara and Thomas J Mueller. “Laminar separation bubble characteristics on an airfoil at low Reynolds numbers”. In: *AIAA journal* 25.8 (1987), pp. 1033–1041.

[35] Tomohisa Ohtake, Yusuke Nakae, and Tatsuo Motohashi. “Nonlinearity of the aerodynamic characteristics of NACA0012 aerofoil at low Reynolds numbers”. In: *Japan Society of Aeronautical Space Sciences* 55.644 (2007), pp. 439–445.

[36] PR Owen and L Klanfer. “On the laminar boundary layer separation from the leading edge of a thin aerofoil”. In: (1955).

[37] Donghun Park, Hojoon Shim, and Yunggyo Lee. “PIV Measurement of Separation Bubble on an Airfoil at Low Reynolds Numbers”. In: June 2019. DOI: 10.2514/6.2019-3644.

[38] Robert W. Paterson, Paul G. Vogt, Martin R. Fink, and C. Lee Munch. “Vortex Noise of Isolated Airfoils”. In: *Journal of Aircraft* 10.5 (1973), pp. 296–302. DOI: 10.2514/3.60229.

[39] Laura L Pauley, Parviz Moin, and William C Reynolds. “The structure of two-dimensional separation”. In: *Journal of fluid Mechanics* 220 (1990), pp. 397–411.

[40] S Pröbsting. “Airfoil self-noise-investigation with particle image velocimetry”. In: (2015).

[41] Stefan Pröbsting, Fulvio Scarano, and Scott Morris. “Regimes of tonal noise on an airfoil at moderate Reynolds number”. In: *Journal of Fluid Mechanics* 780 (Sept. 2015), pp. 407–438. DOI: 10.1017/jfm.2015.475.

[42] Stefan Pröbsting and S. Yarusevych. “Laminar separation bubble development on an airfoil emitting tonal noise”. In: *Journal of Fluid Mechanics* 780 (Oct. 2015), pp. 167–191. DOI: 10.1017/jfm.2015.427.

[43] Manikandan Ramasamy. “Hover performance measurements toward understanding aerodynamic interference in coaxial, tandem, and tilt rotors”. In: *Journal of the American Helicopter Society* 60.3 (2015), pp. 1–17.

[44] Bernardo Luiz Ribeiro, Cayan Dantas, and William Wolf. “Intermittency of a transitional airfoil flow with laminar separation bubble solved by the lattice-Boltzmann method”. In: *Aerospace Science and Technology* (2024), p. 109907.

[45] Matthew D Ripley and Laura L Pauley. “The unsteady structure of two-dimensional steady laminar separation”. In: *Physics of Fluids A: Fluid Dynamics* 5.12 (1993), pp. 3099–3106.

[46] Michel Roger and Stéphane Moreau. “Back-scattering correction and further extensions of Amiet’s trailing-edge noise model. Part 1: theory”. In: *Journal of Sound and vibration* 286.3 (2005), pp. 477–506.

[47] James B Rorke. “Hover performance tests of full scale variable geometry rotors”. In: (1976).

[48] Anatol Roshko. “On the Development of Turbulent Wakes from Vortex Streets”. In: *Journal of the Aeronautical Sciences* 22.2 (1955), pp. 124–132. DOI: 10.2514/8.3380.

[49] Karl Schwarzschild. “Die beugung und polarisation des lichts durch einen spalt. i”. In: *Mathematische Annalen* 55.2 (1901), pp. 177–247.

[50] Michael Selig, Robert Deters, and Gregory Wiliamson. “Wind tunnel testing airfoils at low Reynolds numbers”. In: *49th AIAA Aerospace Sciences Meeting including the New Horizons Forum and Aerospace Exposition*. 2011, p. 875.

[51] Michael S. Selig, John F. Donovan, and David B. Fraser. *Airfoils at Low Speeds*. Virginia Beach, VA: SoarTech Publications, 1996.

[52] Robert E Sheldahl and Paul C Klimas. *Aerodynamic characteristics of seven symmetrical airfoil sections through 180-degree angle of attack for use in aerodynamic analysis of vertical axis wind turbines*. Tech. rep. Sandia National Lab.(SNL-NM), Albuquerque, NM (United States), 1981.

[53] S. Sunada, K. Ozaki, M. Tanaka, T. Yasuda, K. Yasuda, and Keiji Kawachi. “Airfoil characteristics at a low Reynolds number”. In: *Journal of Flow Visualization and Image Processing* 7 (Jan. 2000), p. 10. DOI: 10.1615/JFlowVisImageProc.v7.i3.20.

[54] Christopher KW Tam. “Discrete tones of isolated airfoils”. In: *The Journal of the Acoustical Society of America* 55.6 (1974), pp. 1173–1177.

[55] Itiro Tani. “Low-speed flows involving bubble separations”. In: *Progress in Aerospace Sciences* 5 (1964), pp. 70–103.

[56] Charles E Tinney and John Valdez. “Thrust and Acoustic Performance of Small-Scale, Coaxial, Corotating Rotors in Hover”. In: *AIAA Journal* (2019), pp. 1–11.

[57] Jacob M Turner and Jae Wook Kim. “Aerofoil dipole noise due to flow separation and stall at a low Reynolds number”. In: *International Journal of Heat and Fluid Flow* 86 (2020), p. 108715.

[58] John A. Valdez and Charles E. Tinney. “Wake of a Coaxial Corotating Rotor in Hover”. In: *AIAA Journal* 60.8 (2022), pp. 4829–4839. DOI: 10.2514/1.J061651. eprint: https://doi.org/10.2514/1.J061651. URL: https://doi.org/10.2514/1.J061651.

[59] Siena Whiteside, Nikolas Zawodny, Xiaofan Fei, Nicole A Pettingill, Michael D Patterson, and Paul Rothhaar. “An Exploration of the Performance and Acoustic Characteristics of UAV-Scale Stacked Rotor Configurations”. In: *AIAA Scitech 2019 Forum*. 2019, p. 1071.

[60] J. E. Ffowcs Williams and D. L. Hawkings. “Sound Generation by Turbulence and Surfaces in Arbitrary Motion”. In: *Philosophical Transactions of the Royal Society of London* 264.1151 (1969), pp. 321–342.

[61] JE Ffowcs Williams and LH Hall. “Aerodynamic sound generation by turbulent flow in the vicinity of a scattering half plane”. In: *Journal of fluid mechanics* 40.4 (1970), pp. 657–670.

[62] Justin Winslow, Hikaru Otsuka, Bharath Govindarajan, and Inderjit Chopra. “Basic Understanding of Airfoil Characteristics at Low Reynolds Numbers (104–105)”. In: *Journal of Aircraft* 55 (Dec. 2017), pp. 1–12. DOI: 10.2514/1.C034415.

[63] Richard Woodward. “Noise of a model high speed counterrotation propeller at simulated takeoff/approach conditions (F7/A7)”. In: *11th Aeroacoustics Conference*. 1987, p. 2657.

[64] SE Wright. “The acoustic spectrum of axial flow machines”. In: *Journal of Sound and Vibration* 45.2 (1976), pp. 165–223.

[65] Serhiy Yarusevych, Pierre Sullivan, and John Kawall. “Coherent structures in an airfoil boundary layer and wake at low Reynolds numbers”. In: *Physics of Fluids* 18 (Apr. 2006), p. 044101. DOI: 10.1063/1.2187069.

[66] Yung H. Yu. “Rotor blade–vortex interaction noise”. In: *Progress in Aerospace Sciences* 36.2 (2000), pp. 97–115. ISSN: 0376-0421. DOI: https://doi.org/10.1016/S0376-0421(99)00012-3.

3

EXPERIMENTAL AND NUMERICAL METHODOLOGY

This chapter outlines the numerical and experimental methods utilized throughout this thesis. Specifically, Sect. 3.1 details the hybrid computational aeroacoustic strategy applied in this study, which combines the Lattice-Boltzmann method for near-field aerodynamic calculations with the Ffowcs-Williams and Hawkings acoustic analogy for for far-field noise prediction. Conversely, Sect. 3.2 describes the experimental techniques employed to measure flow fields, including particle image velocimetry and acoustic measurements methods.

3.1. NUMERICAL APPROACH

Direct methods in computational aeroacoustics (CAA) refers to numerical techniques in which both the unsteady turbulent flow and the resulting acoustic radiation are derived from solving compressible flow equations [28]. These methods require a large computational domain that spans from the noise source to the observer location, needing high spatial resolution to accurately resolve high-frequency acoustic waveforms. This often results in prohibitive computational costs, making direct methods impractical for industrial-scale aeroacoustic problems [29].

In contrast, hybrid methods separate the noise computation process into two main parts [31]:

1. Flow simulation: the unsteady flow field in the near-field region responsible for noise generation is computed using a scale-resolving CFD method, such as for instance Reynolds-Averaged Navier-Stokes (RANS), Large Eddy Simulation (LES) or Lattice Boltzmann Method (LBM) [31, 15].

2. Acoustic propagation: the previously computed flow data is then used for noise prediction by applying an acoustic analogy or propagation model. Commonly used models include the Ffowcs Williams and Hawkings (FW-H) analogy [34], Kirchhoff's method [4], or linearized Euler equations [31].

Hybrid methods offer substantial savings in computational resources compared to direct methods. They require a fine computational grid only in the near-field of the body, hence the computational cost is not linked to the propagation distance.

The numerical aeroacoustic simulations conducted Sect. 6 of this thesis utilize a hybrid approach, specifically the lattice-Boltzmann method coupled with the Ffowcs Williams and Hawkings acoustic analogy. The lattice-Boltzmann method is employed to capture the unsteady aerodynamics in the near-field region, while the Ffowcs Williams and Hawkings analogy is used to calculate the resulting far-field noise radiation. These two computational methods are detailed in the subsequent sections.

3.1.1. THE LATTICE BOLTZMANN METHOD

The numerical approach employed throughout this thesis is the Lattice-Boltzmann Method (LBM), which is implemented in the commercial software Simulia PowerFLOW 6-2021. The LBM is based on the Boltzmann's kinetic theory, often referred to as the Boltzmann Transport Equation (BTE), which describes the statistical behavior of a thermodynamic system out of equilibrium. The system is seen as a collection of particles and the instantaneous state of the system is defined by using a probability distribution function $F(\mathbf{x}, t, \mathbf{V})$, which represents the probability of finding a particle at the position $\mathbf{x}$ and time t, while having velocity $\mathbf{V}$. The microscopic motion of individual particles is linked to the macroscopic properties of the system, such as pressure, momentum and temperature.

The LBM solves the BTE on a cartesian mesh, the lattice, made up of uniform cells where the particles move along discrete directions. The mathematical expression of the lattice Boltzmann equation is given as:

$$F_q\left(\mathbf{x}+\mathbf{V_q}\Delta t, t+\Delta t\right)-F_q\left(\mathbf{x}, t\right)=\kappa_q\left(\mathbf{x}, t\right) \tag{3.1}$$

where F_q represents the particle distribution function along the q-th direction of the lattice, $\mathbf{V_q}$ is the discrete particle velocity vector at the time t and position $\mathbf{x}$, $V_q\Delta t$ and Δt are the space and time velocity increments, respectively. The term κ_q on the right-hand side is the collision term, which represents the variations in the particle velocity distribution due to momentum exchange between particles. The macroscopic fluid properties, such as density ρ, velocity $\mathbf{u}$ and total energy E are obtained from the particle distribution function F_q [27]:

$$\rho\left(\mathbf{x}, t\right)=\sum_q F_q\left(\mathbf{x}, t\right) \tag{3.2}$$

$$\rho\mathbf{u}\left(\mathbf{x}, t\right)=\sum_q V_q F_q\left(\mathbf{x}, t\right) \tag{3.3}$$

$$\rho E\left(\mathbf{x}, t\right)=\sum_q \frac{1}{2} V_q^2 F_q\left(\mathbf{x}, t\right) \tag{3.4}$$

It can also be demonstrated that the Navier-Stokes equations can be derived from the BTE by calculating the zeroth, first, and trace of the second-order moments of Eqn. 3.1. The solution is known as the Chapman-Enskog expansion [8] and involves expanding the distribution function in terms of Knudsen number (a ratio between the mean free path of the particle and the characteristic length-scale in the flow).

The LBM algorithm is made by four main steps:

1. Initialization: the simulation domain is discretized and the particle distribution function is initialized at each lattice point based on the initial conditions.

2. Advection: during this phase, the particle distribution function at each lattice point is shifted to the adjacent ones, following the discrete velocity directions. From a mathematical point of view, this step is computed by means of Eq. 3.1 with the collision term set to zero, hence:

$$F_q\left(\mathbf{x}+\mathbf{V_q}\Delta t, t+\Delta t\right)=F_q\left(\mathbf{x}, t\right) \tag{3.5}$$

3. Collision: after computing the macroscopic quantities using F_q from Eq. 3.6, the local equilibrium distribution function is calculated and, subsequently, the collision term κ_q is determined. The latter is finally used to update the local distribution function as:

$$F_q^*\left(\mathbf{x}+\mathbf{V_q}\Delta t, t+\Delta t\right)=F_q\left(\mathbf{x}+\mathbf{V_q}\Delta t, t+\Delta t\right)+\kappa_q\left(\mathbf{x}, t\right) \tag{3.6}$$

The collision step occurs locally at each node, making each nodal computation independent of the others. This characteristic allows for highly efficient parallelization of the computation.

4. Application of boundary conditions: the distribution functions at the domain boundaries are defined by the type of boundary conditions. For example, a no-slip condition at solid walls is modelled with a bounce-back method which implies that particles that hits the wall are reflected back along the same path (normal and tangential component of F_q are inverted). For inlet/outlet conditions instead, macroscopic quantities such as velocity or pressure are prescribed and used to reconstruct the unknown distribution functions.

The LBM scheme is solved on a lattice consisting of cubic volumetric elements known as voxels. Within the simulation domain, different variable resolution (VR) regions can be defined to use finer grids in regions where detailed flow information is crucial, such as areas with high-velocity gradients or complex geometry, while employing coarser grids in less critical areas. The voxel resolution, i.e. the number of voxels along a characteristic length, vary by a factor of 2 between adjacent VRs. Additionally, since the solver employs an explicit time-marching scheme based on a unitary Courant number, the time-step also changes by a factor of two between adjacent VRs. For the finest VR region, the distribution function in each voxel is updated at every time-step, whereas in coarser VRs, it is updated every 2^M time-steps, where M represents the difference between the finest VR level and the current level. Solid walls are facetized into planar surface elements, known as surfels, within each voxel that intersects with the wall geometry. This allows the LBM solver to handle complex geometries automatically, thus simplifying the tedious manual work typically required for the volume meshing step in body-fitted CFD methods.

3.1.2. VELOCITY-SPACE DISCRETIZATION AND THE COLLISION OPERATOR

The collision operator employed in the LBM is the Bhatnagar-Gross-Krook (BKG) approximation [3], given by:

$$\kappa_q(\mathbf{x},t) = -\frac{1}{\tau}\left[F_q(\mathbf{x},t) - F_q^{eq}(\mathbf{x},t)\right] \tag{3.7}$$

The BKG collision operator simplifies the process of particle collision by assuming that the distribution functions F_q relax toward their local equilibrium values F_q^{eq} at a rate determined by the relaxation time τ. F_q^{eq} is the Maxwell-Boltzmann equilibrium distribution function [9]:

$$F_q^{eq} = \frac{1}{(2\pi RT)^{D/2}} e^{\left(-\frac{|\mathbf{V_q}-\mathbf{u}|^2}{2RT}\right)} \tag{3.8}$$

where R is the ideal gas constant, T the gas temperature and D the number of spatial dimensions. The Boltzmann equation is discretized not only in the spatial and temporal domains but also in the velocity space, by means of a Gauss-Hermite quadrature method. The distribution function is expanded instead into Hermite polynomials, as the expansion coefficients correspond to the velocity moments of the distribution function. Therefore, Eq. 3.1 can be reformulated as [10]:

$$\frac{\partial F_q}{\partial t} + \mathbf{V_q}\cdot\nabla F_q = \frac{F_q^{eq} - F_q}{\tau} \tag{3.9}$$

and the Hermite expansion of F_q^{eq} for a set of discrete velocities $\mathbf{V_q}$ is expressed as:

$$F_q = w_q \sum_{n=0}^{\infty} \frac{1}{n!} a^{(n)} \mathscr{H}^{(n)}(\mathbf{V_q}) \tag{3.10}$$

where w_q is a weight function, $\mathscr{H}^{(n)}$ is the n-th order Hermite polynomial and $a^{(n)}$ the Hermite expansion coefficients, given by:

$$a^{(n)} = \sum_{q=1}^{Q} F_q^{eq} \mathscr{H}^{(n)}(\mathbf{V_q}) \tag{3.11}$$

The truncation order n of the Hermite expansion determine the accuracy of the approximation. A fourth-order truncation ($n = 4$) is required to fully recover the Navier-Stokes equations, ensuring both momentum and energy conservation laws are satisfied. With a third-order truncation ($n = 3$), energy conservation is not maintained, but the Navier-Stokes equations can still be accurately recovered under isothermal conditions without introducing an error term. For the present study, since no significant thermal effects are expected, the distribution function is approximated with a third-order expansion:

$$F_q \approx \rho w_q \left[1 + \frac{\mathbf{V_q} \cdot \mathbf{u}}{\Theta} + \frac{(\mathbf{V_q} \cdot \mathbf{u})^2}{2\Theta^2} - \frac{\mathbf{u}^2}{2\Theta} + \frac{(\mathbf{V_q} \cdot \mathbf{u})^3}{6\Theta^3} - \frac{(\mathbf{V_q} \cdot \mathbf{u})\mathbf{u}^2}{2\Theta^2} \right] \tag{3.12}$$

where Θ is the non dimensional lattice temperature. This formulation is used within the low-Mach number solver for a three-dimensional lattice with 19 discrete velocity vectors, referred to as D3Q19 model. For the latter, Θ is equal to $1/3$, while $w_q = 1/3$ for the rest velocity, $1/18$ for the main axis and $1/36$ for the diagonals.

Lastly, it is important to highlight the relation between the relaxation time τ in Eq. 3.7 and the kinematic viscosity ν. By employing a Chapman-Enskog expansion and considering a lattice with a grid spacing of Δx and a time-step Δt, the relationship is given by:

$$\nu = \frac{1}{3} \left(\frac{\Delta x}{\Delta t} \right)^2 \left(\tau - \frac{\Delta t}{2} \right) \tag{3.13}$$

Using a single relaxation time simplifies the computational model, enhancing the algorithm's efficiency. However, the BGK model cannot distinguish between momentum exchanges through viscosity and energy exchanges through thermal conduction, leading to an incorrect assumption of a unit Prandtl number (the ratio between viscosity and thermal conduction). Therefore, other approaches, such as the multiple relaxation time collision operators or double distribution functions [2], are preferred for accurate thermal simulations.

3.1.3. VLES TURBULENCE MODEL

The LBM implemented in PowerFLOW is integrated with a very large eddy simulation (VLES) approach for turbulence modelling. In particular, a two-equations $k-\epsilon$ renormalization group (RNG) formulation is used on the unresolved scales of turbulence [35],

which are selected by meand of a model based on the local flow swirl. The two equations $k-\epsilon$ RNG model is solved on the same LBM grid with a second-order finite-difference scheme and is used to compute a turbulent relaxation time (τ_{turb}) that is added to the viscous relaxation time (τ):

$$\tau_{turb} = \tau + C_{\mu}\frac{k^2/\epsilon}{(1+\eta^2)^{1/2}} \tag{3.14}$$

where C_{μ} is equal to 0.09, k and ϵ are the tubulent kinetic energy and dissipation, respectively, and η is a function based on the local strain, vorticity and helicity parameters. This approach is not the same as using a $k-\epsilon$ RNG model in a RANS method. In the present method, the eddy viscosity is not explicitly altered; hence, the modeled Reynolds stresses are not directly added to the flow-governing equations (as a closure of the system of equations) as they are in RANS. Instead, the $k-\epsilon$ RNG model influences the particle system's progression toward thermodynamic equilibrium by adjusting the relaxation time, aligning it with the characteristic time scales of the turbulent flow motion. Thus, the Reynolds stresses arise from the LBM computation rather than from semi-empirical modeling.

Because LBM utilizes a Cartesian mesh, it does not support differing cell sizes across the three spatial dimensions or grid stretching solely. Consequently, resolving the boundary layer on the no-slip wall would become prohibitively expensive for high Reynolds number applications. in the wall-normal direction. Hence, PowerFLOW applies a wall function from the first voxel adjacent to a no-slip solid surface to model the boundary layer. The wall function is based on the generalized law-of-the-wall model [16], extended to consider the effects of pressure gradient and surface roughness and it is expressed in terms of dimensionless velocity u^+ and wall-distance coordinate y^+:

$$u^+ = \frac{1}{\kappa}\ln\left(\frac{y^+}{A}\right) + B \tag{3.15}$$

with:

$$y^+ = \frac{yu_{\tau}}{\nu}, \qquad u_{\tau} = \sqrt{\frac{\tau_w}{\rho}}, \qquad u^+ = \frac{u}{u_{\tau}}, \qquad A = 1 + g\left(\frac{dp}{ds}\right)$$

where u_{τ} and τ_w are the friction velocity and the wall shear stress, respectively, A is a function of the streamwise pressure gradient dp/ds, κ and B are empirical constants equal to 0.41 and 5, respectively. The wall model provides also the boundary conditions for the $k-\epsilon$ RNG turbulence model.

3.1.4. ACOUSTIC PREDICTIONS

As the LBM is inherently compressible and time-dependent, it enables the direct recording from the simulation domain of the time history of the radiated acoustic pressure. Brès et al. [6] examined the acoustic characteristics of the LBM as implemented in PowerFLOW. Their comparison with theoretical predictions demonstrated the method's low dispersive and dissipative errors, indicating that LBM can potentially be used for simulating acoustic propagation in the time-domain. However, as explained above, due to the

prohibitively computational cost, an hybrid method based on the Ffowcs-Williams and Hawkings (FW-H) acoustic analogy [34] for far-field noise computation is used throughout this thesis

3.1.5. FFOWCS-WILLIAMS AND HAWKINGS ACOUSTIC ANALOGY

The Ffowcs Williams-Hawkings (FW-H) analogy [34] is an extension of Lighthill's acoustic analogy [17], designed to predict sound generated by turbulent flows, particularly in the presence of solid boundaries in arbitrary motion. It provides a framework to account for noise sources in unsteady fluid flows, including contributions from both volume sources (such as turbulence) and surface sources (such as moving boundaries). The derivation of the FW-H analogy starts from the definition of a function $f(\mathbf{x}, t)$, such that $f > 0$ outside a volume enclosed by a surface S and $f < 0$ inside the volume. The integration surface S, encompassing the source region, is defined by $f = 0$. The surface S is depicted in Fig. 3.1, with $\mathbf{u}$ and $\mathbf{v}$ being the flow and surface velocity, $\hat{\mathbf{n}} = \nabla f$ the surface outward normal, $\mathbf{y}$ indicating the source position, $\mathbf{x}$ and $\mathbf{v_0}$ the observer position and velocity, respectively. Within this control surface, the flow is replaced by a quiescent fluid with mass and momentum sources distributed across the surface. This is accomplished by introducing the generalized derivative (which adopts the Dirac $\delta(f)$ and Heaviside $H(f)$ functions) into the continuity and momentum equations, leading to the FW-H equation for the acoustic pressure p' in differential form:

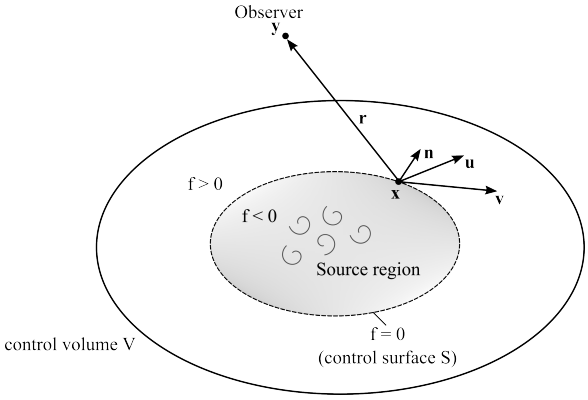

Figure 3.1: Sketch of the notation used for the FW-H acoustic analogy formulation.

$$\Box^2 \left[p' H(S)\right] = \frac{\partial}{\partial t}\left[Q\delta(S)\right] - \frac{\partial}{\partial x_i}\left[L_i \delta(S)\right] + \frac{\partial^2}{\partial x_i x_j}\left[T_{ij} H(S)\right] \tag{3.16}$$

where:

$$Q = \rho_0 U_i \hat{n}_i = \left[\rho_0 v_i + \rho(u_i - v_i)\right]\hat{n}_i \tag{3.17}$$

$$L_i = L_{ij}\hat{n}_j = \left[P_{ij} + \rho u_i (u_j - v_j)\right]\hat{n}_j \tag{3.18}$$

$$P_{ij} = (p - p_0)\delta_{ij} - \tau_{ij} \tag{3.19}$$

In Eq. 3.16 $\Box$ is the wave (or D'Alambertian) operator in three dimensional space, $p' = c_0^2\rho' = c_0^2(\rho - \rho_0)$ with c_0 and ρ_0 being the speed of sound and density of the fluid at rest, respectively. Note that p' can be interpreted as acoustic pressure if $p'/\rho_0 << 1$, a condition typically met at a sufficient distance from the source (far-field). Eq. 3.16 resembles the Lighthill analogy, with the left-hand side describing the wave propagation and the source terms on the right-hand side. The first term is referred to as the thickness (monopole) source term, which accounts for the fluid displaced by the movement of the control surface. The second term represents the loading (dipole) source term and accounts for the unsteady forces exerted by the control surface onto the surrounding fluid. Finally, the third term, containing the Lighthill stress tensor T_{ij}, is the quadrupole source term, accounting for all the flow non-linearities (e.g. turbulence) throughout the control volume.

A solution of the FW-H Eq. 3.16 in the acoustic far-field can be obtained by convoluting it with the free-space Green function and exploiting the properties of the Dirac and Heaviside functions:

$$\begin{aligned} 4\pi\rho' = &\frac{\partial}{\partial t}\int_{S=0}\left[\frac{Q}{r(1-M_r)}\right]_{ret} dS \\ &-\frac{\partial}{\partial x_i}\int_{S=0}\left[\frac{L_i}{r(1-M_r)}\right]_{ret} dS \\ &+\int_{S>0}\frac{\partial^2}{\partial x_i x_j}\left[\frac{T_{ij}}{r(1-M_r)}\right]_{ret} dV \end{aligned} \tag{3.20}$$

where the subscript ret denotes that the integrals are evaluated at the retarded time $\tau = t - \left|\mathbf{x}(t) - \mathbf{y}(\tau)\right|/c_0$, $r = \left|x - y\right|$ and the term $1 - M_r$ at the denominator of each source term (with M_r being the component of the source Mach number vector in the direction of the observer) account for the Doppler effect due to the relative motion between source and observer. Transforming in Eq. 3.20 the spatial derivatives into time derivatives and moving them inside the integrals (refer to Refs. [7, 13, 5] for more details), while neglecting the quadruple contribution (less significant than the other terms in low-speed flows), the Farassat's formulation 1A [12] of the FW-H equation (used throughout this thesis) is obtained:

$$p'(\mathbf{x}, t) = p'_L(\mathbf{x}, t) + p'_T(\mathbf{x}, t) \tag{3.21}$$

where the expressions for the thickness p'_T and loading p'_L noise are reported below:

$$\begin{aligned} 4\pi p'_T(\mathbf{x}, t) = &\int_{f=0}\left[\frac{\rho_0\left(\dot{U}_n + U_{\dot{n}}\right)}{r(1-M_r)^2}\right]_{ret} \mathrm{dS}(\mathbf{y}) \\ &+\int_{f=0}\left[\frac{\rho_0 U_n\left(r\dot{M}_r + c_0(M_r - M_r^2)\right)}{r^2(1-M_r)^3}\right]_{ret} \mathrm{dS}(\mathbf{y}) \end{aligned} \tag{3.22}$$

$$4\pi p'_L(\mathbf{x},t) = \frac{1}{c_0}\int_{f=0}\left[\frac{\dot{L_r}}{r(1-M_r)^2}\right]_{ret} \mathrm{dS}(\mathbf{y}) + \int_{f=0}\left[\frac{L_r - L_M}{r^2(1-M_r)^2}\right]_{ret} \mathrm{dS}(\mathbf{y}) + \int_{f=0}\left[\frac{L_r\left(r\dot{M}_r + c_0(M_r - M^2)\right)}{r^2(1-M_r)^3}\right]_{ret} \mathrm{dS}(\mathbf{y}) \tag{3.23}$$

where the dots on quantities indicate the time derivative with respect to the source time τ, the subscripts n and r represent the projection along the surface normal $\hat{\mathbf{n}}$ and observer $\hat{\mathbf{r}}$ directions, respectively (e.g. $U_n = U_i\hat{n}_i$, $L_r = L_i\hat{r}_i$). Finally $L_M = L_i M_i$ and $U_{\dot{n}} = U_i\dot{\hat{n}}_i$.

The integrals in Eqs. 3.23 and 3.22 can be computed with two different methods, referred as "retarded time" and "advanced time" approaches. In the retarded time approach the computational time is the reception time, i.e. the observer time t. The acoustic disturbances that contribute to the signal received by the observer at the time t are emitted at an earlier (retarded) time τ, which is determined by the distance $\left|\mathbf{x}(t) - \mathbf{y}(\tau)\right| / c_0$ between the source and the observer. In the advanced time approach instead, the computation time is the emission time, i.e. the source time τ. For each source element and at each computational time, the future (advanced) time at which the disturbance will reach the observer is determined as $t = \tau + \left|\mathbf{x}(t) - \mathbf{y}(\tau)\right| / c_0$. Finally, the acoustic signal is constructed in the observer's time domain by summing all the contributions. One of the main advantages of the advanced time approach is that the contribution from the integration surface at any given time is calculated using the current aerodynamic data, eliminating the need for interpolating flow data from earlier time steps as required by the retarded time approach. This enables acoustic predictions to be computed in parallel to the flow field computations. For this reason, the FW-H solver used in the thesis is based on the advanced time solution.

In the definition of the FW-H the integration surface S does not need to be necessarily coincident with the physical surface of a body. If this is the case, the flow velocity on a point on the surface is equal to the surface velocity itself ($u_i = v_i$), and the resulting formulation is referred as *solid FW-H*. An alternative approach, referred as *permeable FW-H*, is proposed by Francescantonio [11]. This method consists of positioning a permeable integration surface at a distance from the body's physical surface. The permeable surface encompasses all the significant flow non-linearities (quadrupole). Consequently, the quadrupole term in Eq. 3.20 vanishes because the Lighthill's stress tensor is, by definition, zero outside the permeable surface. All the quadruple contributions within the permeable surface are taken into account by a distribution of monopoles and dipoles on this surface.

The main issue of this approach is related to the positioning of the permeable surface. Inevitably, vortical structures cross the surface and spurious noise (also known as "pseudo-sound") is generated [18]. This occurs because the permeable surface does not contain all the quadrupole sources, which would otherwise be included in the volume integral in Eq. 3.20. To overcome this issue and limit the generation of pseudo-sound,

several methods are proposed in literature [26]. One approach involves extending the permeable surface far from the body and defining an area where the simulation domain is intentionally coarsened to dissipate small-scale vortical structures before they cross the surface [26]. However, if this region is too close to the body, the non-physical damping of the vortical structures can potentially alter the aerodynamic solution of the body. A second strategy consists of using an open surface, thereby eliminating the portion of the surface intersected by turbulent eddies. Alternatively, multiple permeable surfaces with different downstream terminations (end-caps), separated by a certain distance, can be used. The noise computed from the different surfaces is then averaged, effectively canceling the pseudo-sound generated by the passage of the vortical structures through the end-caps, which is not consistent from one surface to another. Mendez et al. [19] compared these latter two approaches for a jet-noise application, concluding that the use of end-caps provides better agreement with the experimental results compared to the open surface approach. The latter showed a significant error in the low-frequency region.

3.2. EXPERIMENTAL APPROACH

This section provides an overview of the experimental methods employed to examine flow and acoustics in this research. It details the application of particle image velocimetry and oil flow techniques for flow visualization and analysis, along with the acoustic measurement methods used to assess the far-field noise generated by the propellers under investigation.

3.3. PARTICLE IMAGE VELOCIMETRY (PIV)

In the experiments presented in this report, Particle Image Velocimetry (PIV) has been extensively utilized as flow-field measurement technique. Consequently, a brief overview of the key features of this technique is provided here, while a more comprehensive explanation can be found in References [1, 22].

PIV is a laser optical measurement method that allows the quantification of velocity components within a specific section of the flow field by introducing seeding particles into the flow. The planar PIV technique measures only the in-plane velocity components, whereas stereoscopic PIV can capture the out-of-plane velocity component as well. Being based on optical principles, PIV is a non-intrusive method, allowing velocity measurements without disturbing the flow field, unlike other techniques such as pressure probes and hot wires. Secondly, PIV enables measurements across entire areas of the flow with high spatial resolution, while conventional techniques typically provide data at discrete points in the flow.

A typical PIV setup is depicted in Fig. 3.2. It consists of a pulsed light source (double-head pulsed laser) which is collimated in a thin light sheet and directed toward the flow through a sequence of lenses (light sheet optics) and mirrors. The thin laser sheet is used to illuminate a portion of the flow field and define the measurement domain. The investigated flow is seeded with tracer particles, which are sufficiently small to accurately follow the fluid motion and not alter the flow characteristics. The particles flowing in the measurement plane are illuminated at least twice through short light pulses separated by a short time interval. The scattered light from the particles is recorded on a double-

frame CCD camera placed perpendicular to the measurement frame.

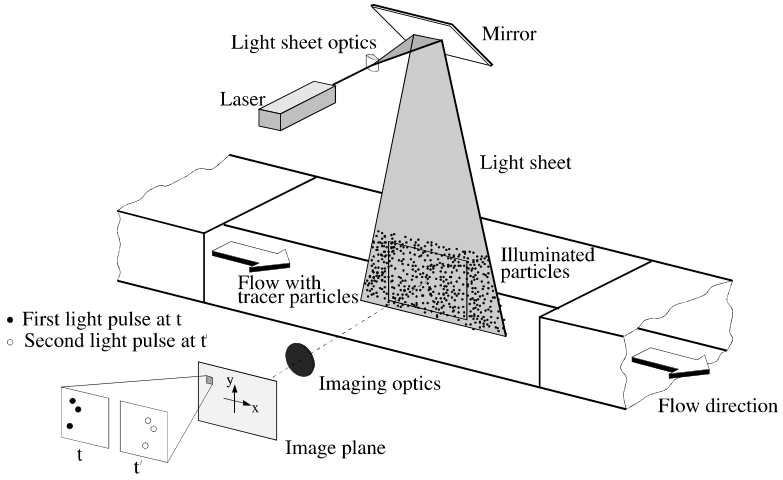

Figure 3.2: Schematic of a planar Particle Image Velocimetry setup (reproduced from [22])

The stereoscopic PIV technique allows the measurement of both in-plane and out-of-plane velocity components in the measurement plane [33]. Fig. 3.3 represents a sketch of a stereoscopic PIV setup with lenses in transitional system (the axis of both cameras are perpendicular to the light sheet). In this case, two distinct cameras are used to observe the same measurement region from different angles of view. Since the optical axis of the cameras are not perpendicular to the object plane, displacements perpendicular to the plane also affect the recorded particle displacements on the camera sensors (apparent in-plane displacement). The addition of a second view provides two additional equations which are used to solve for the three-dimensional displacement vector [21].

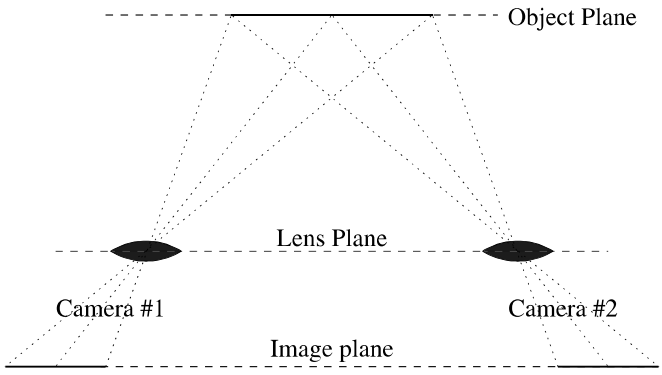

Figure 3.3: Stereoscopic PIV system in transitional configuration (reproduced from [22])

The recorded images are divided into small sub-domains or interrogation windows, which are small enough to assume that all the particles within a window move homogeneously between the two illuminations. A single displacement vector is obtained for each interrogation window using a statistical cross-correlation algorithm between the two frames. The displacement is determined by locating the highest peak in the correlation plane. The velocity of the moving particles is then calculated by considering the time delay between the two pulses and the optical magnification factor. This procedure is repeated across the entire image domain, resulting in the instantaneous velocity measurement in a planar cross-section of the observed flow [30].

The accuracy of the cross-correlation step can be enhanced through the use of iterative schemes. One such method known as window deformation, is carried out as a two-step analysis within a predictor-corrector loop. In this approach, the interrogation is repeated a second time using a shifted window derived from the first pass [23]. Another iterative method is the multigrid approach, in which the correlation process is conducted multiple times while progressively reducing the size of the interrogation window [25]. Following the cross-correlation step, erroneous vectors are eliminated using the universal outlier detection method [32]. This filtering process is based on the principle that the measured displacements at each location should be statistically comparable to neighboring vectors. The discarded vectors are subsequently replaced by interpolating adjacent data.

3.4. PIV MEASUREMENTS APPARATUS

Stereoscopic PIV measurements are conducted for the isolated propeller study which will be detailed in Sections 4 and 5. Specifically, two PIV setups are utilized to examine the flow around the blade cross-section of the blade at $r/R = 60\%$ (Fig. 3.4) and in the propeller wake (Fig. 3.5). In both setups, the flow is seeded with particles of 1 micrometer median diameter produced by a SAFEX Twin Fog generator with SAFEX-Inside-Nebelfluid, a mixture of dyethelene glycol and water. These particles are introduced into the wind tunnel circuit to ensure a uniform concentration as they recirculate within the test section. Illumination of the field of view is provided by a double cavity Quantel Evergreen EVG00200 Nd:YAG laser with 200 mJ/pulse energy.

To measure the flow over a cross-section of the airfoil, two laser sheets about 1 mm thick are created: one illuminating the suction side and the other the pressure side, to eliminate shadow regions within the field of view (FOV). This configuration is achieved by combining two fields of view, labeled as FOV 1 and FOV 2 in Fig. 3.4b. The white area shown in the schematic represents the part combined for the full field of view visualization. For the cross-section measurements, four Imager sCMOS cameras (two for the suction side and two for the pressure side) with a resolution of 2560 x 2160 pixels and equipped with four Nikon lenses of 200 mm focal length at f# 11 are used. Scheimpflug adapters are mounted on each camera to ensure focus on the measurement plane. Sets of 500 images are recorded in phase-locked mode. To achieve phase-locked measurements, a trigger signal from an encoder mounted on the motor shaft controls the timing of the laser and cameras. By specifying a trigger delay in the software, images are captured when the propeller section aligns with the laser plane, as shown in Fig. 3.4a.

For the propeller wake measurements, two imager sCMOS camera (2560 x 2160 px)

equipped with Scheimpflug adapters and two Nikon lenses with 60 mm focal length at f# 8 are used. Also for this case, sets of 500 images are recorded in phase-locked mode. Three propeller phases are selected: $\Psi = 0°$, $\Psi = 45°$, $\Psi = 90°$ (refer to Fig. 3.5b).

The camera calibration, acquisition and post-processing are carried out using LaVision Davis 8.4 software. The images are processed with a cross-correlation algorithm employing the window deformation iterative multi-grid [24]. The final interrogation window sizes are 24 x 24 pixels for the propeller cross-section and 16 x 16 pixels for the wake measurements, with a 75% overlap. Spurious vectors are detected through a median filter and replaced by interpolation. Details of the PIV setup apparatus are summarized in Table 3.1.

Table 3.1: Details of PIV measurement setups.

Imaging Parameters	**Cross-section measurements**	**Wake measurements**
Camera	4 Imager sCMOS	2 Imager sCMOS
Number of pixels [px]	2560 x 2160	2560 x 2160
Pixel size [μm]	6.5 x 6.5	6.5 x 6.5
Focal length [mm]	200	60
Magnification	0.37	0.1
Imaging resolution [px/mm]	$\approx$ 56	$\approx$ 15
FOV [cm^2]	4.5 x 4	16 x 16
Spatial resolution [mm]	$\approx$ 0.4	$\approx$ 0.28
f#	11	8

Imaging Parameters	**Cross-section measurements**	**Wake measurements**
Software	LaVision Davis 8.4	LaVision Davis 8.4
Pulse separation [μs]	10	10
Number of recordings	500	500
Minimum window size [px^2]	24 x 24	16 x 16

3.4.1. OIL-FLOW VISUALIZATION

The PIV measurements described above are employed to visualize the flow around the propeller blade, while surface oil-flow visualizations are used to visualize flow patterns on the blade surface, specifically to highlight the boundary of flow separation, as the oil cannot penetrate the separation boundary.

The blade surface is sprayed with a fluorescent mixture, obtained from 50 mL of Shell Ondina Oil 15 liquid-paraffin wax and 15-25 drops of fluorescent-oil additive A-680, in order to cover the propeller surface with a continuous film of oil. The propeller is brought to the required operating conditions by combining the speed of the tunnel fan and of the propeller controller in order to have an almost constant thrust coefficient. Hence the propeller has been run for 8-10 min at constant operating conditions, allowing the paraffin to develop over the surface and reach the final configuration, and then slowly stopped. The propeller at rest has been illuminated by an ultraviolet lamp with a wide aperture, positioned perpendicular to the model and images are obtained by ac-

quiring snapshots of the blade surface at an angle of about 30°.

3.5. ACOUSTIC MEASUREMENTS

Acoustic measurements are performed using condenser microphones, i.e. electromechanical devices that convert sound waves into electrical signals. These microphones consist of a thin membrane (diaphragm) positioned near a stationary backplate, forming a capacitor. When a sound wave (pressure fluctuation) hits the diaphragm, it vibrates, causing a change in the distance between the diaphragm and the backplate. This leads to a variation in capacitance, which is recorded as a voltage proportional to the amplitude of the sound wave [20].

Condenser microphones offer several advantages. Notably, they have a flat amplitude response across a wide frequency range, allowing for quantitative sound measurements with only a single sensitivity value needed within this range. Their ability to detect slight variations in sound makes them ideal for aeroacoustic testing, where detailed sound pressure level data is required. Specifically, large-diameter microphones (greater than 1/2 inch) are more sensitive to acoustic pressure fluctuations because these fluctuations are averaged over a larger diaphragm area, making them suitable for measuring sources that are particularly quiet at a laboratory scale (e.g., roughness noise). In contrast, smaller diameter microphones (less than 1/2 inch) generally have lower sensitivity but can handle a broader frequency and amplitude range [14]. Additionally, they are built to withstand environmental factors such as temperature and humidity changes, ensuring consistent performance over time. Finally, condenser microphones are calibrated using a pistonphone, which generates pressure fluctuations of a prescribed amplitude and frequency via a vibrating piston. The microphone is exposed to these fluctuations to determine its sensitivity, typically expressed in millivolts per pascal (mV/Pa).

In this study, far-field noise measurements are conducted on the isolated propeller configuration, which will be described in detail in Sections 4 and 5. Due to updates in the acoustic array, which involved changes in both the microphone positions and types, the specifics of the acoustic measurement setup will be detailed in the relevant sections for clarity.

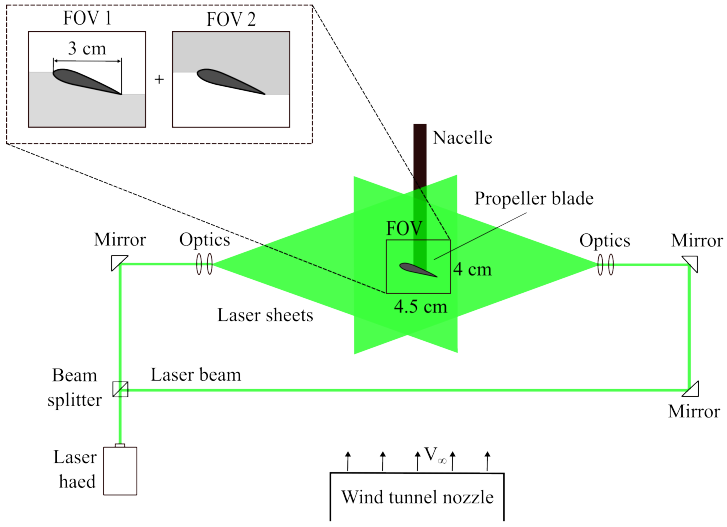

(a) Side view

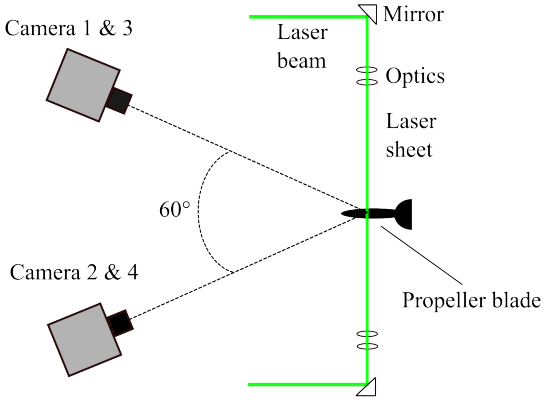

(b) Top view

Figure 3.4: Sketch of PIV laser and camera configurations for the propeller cross-section measurements. Some elements are not drawn to scale.

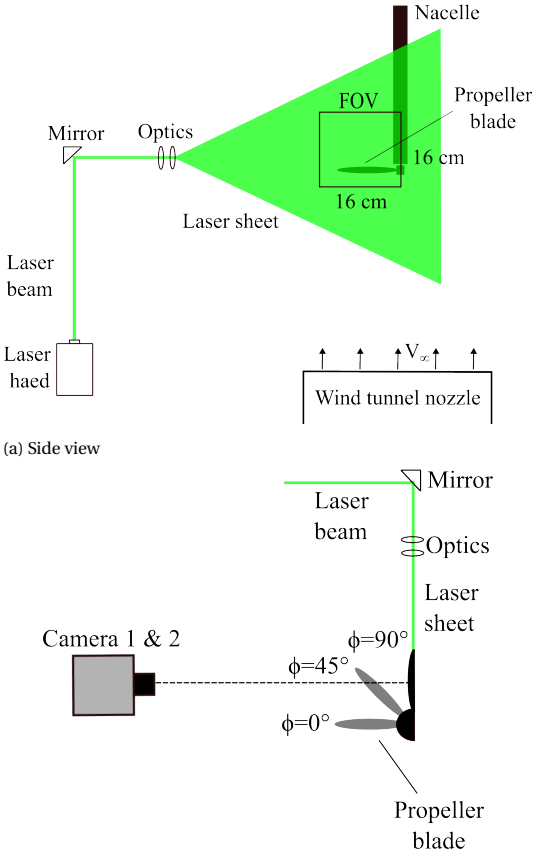

Figure 3.5: Sketch of PIV laser and camera configurations for propeller wake measurements. Some elements are not drawn to scale.

BIBLIOGRAPHY

[1] Ronald J Adrian et al. "Particle-imaging techniques for experimental fluid mechanics". In: *Annual review of fluid mechanics* 23.1 (1991), pp. 261–304.

[2] Thomas Astoul. "Towards improved lattice Boltzmann aeroacoustic simulations with non-uniform grids: Application to landing gears noise prediction". PhD thesis. Aix-Marseille, 2021.

[3] P. L. Bhatnagar, E. P. Gross, and M. Krook. "A Model for Collision Processes in Gases. I. Small Amplitude Processes in Charged and Neutral One-Component Systems". In: *Physical Review* 94 (1954), pp. 511–525. DOI: 10.1103/PhysRev.94.511.

[4] Kenneth S Brentner and Feri Farassat. "Analytical comparison of the acoustic analogy and Kirchhoff formulation for moving surfaces". In: *AIAA journal* 36.8 (1998), pp. 1379–1386.

[5] Kenneth S Brentner and Feridoun Farassat. "Modeling aerodynamically generated sound of helicopter rotors". In: *Progress in aerospace sciences* 39.2-3 (2003), pp. 83–120.

[6] Guillaume Bres, Franck Pérot, and David Freed. "Properties of the lattice Boltzmann method for acoustics". In: *15th AIAA/CEAS aeroacoustics conference (30th AIAA aeroacoustics conference)*. 2009, p. 3395.

[7] D Casalino. "An advanced time approach for acoustic analogy predictions". In: *Journal of Sound and Vibration* 261.4 (2003), pp. 583–612.

[8] S. Chapman and T. G. Cowling. *The Mathematical Theory of Non-uniform Gases*. 1st. Cambridge Mathematical Library, 1991.

[9] H. Chen, S. Chen, and W. H. Matthaeus. "Recovery of the Navier-Stokes equations using a lattice-gas Boltzmann method". In: *Physical Review A* 45 (1992), R5339–R5342. DOI: 10.1103/PhysRevA.45.R5339.

[10] Hudong Chen, Chris Teixeira, and Kim Molvig. "Realization of fluid boundary conditions via discrete Boltzmann dynamics". In: *International Journal of Modern Physics C* 9.08 (1998), pp. 1281–1292.

[11] P Di Francescantonio. "A new boundary integral formulation for the prediction of sound radiation". In: *Journal of Sound and Vibration* 202.4 (1997), pp. 491–509.

[12] Fereidoun Farassat. *Derivation of Formulations 1 and 1A of Farassat*. Tech. rep. 2007.

[13] Feri Farassat and George P Succi. “A review of propeller discrete frequency noise prediction technology with emphasis on two current methods for time domain calculations”. In: *Journal of Sound and Vibration* 71.3 (1980), pp. 399–419.

[14] Stewart Glegg and William Devenport. *Aeroacoustics of low Mach number flows: fundamentals, analysis, and measurement*. Academic Press, 2017.

[15] Timm Krüger, Halim Kusumaatmaja, Alexandr Kuzmin, Orest Shardt, Goncalo Silva, and Erlend Magnus Viggen. “The lattice Boltzmann method”. In: *Springer International Publishing* 10.978-3 (2017), pp. 4–15.

[16] B. E. Launder and D. B. Spalding. “The Numerical Computation of Turbulent Flows”. In: *Computer Methods in Applied Mechanics and Engineering* 3.2 (1974), pp. 269–289. DOI: 10.1016/0045-7825(74)90029-2.

[17] Michael James Lighthill. “On sound generated aerodynamically I. General theory”. In: *Proceedings of the Royal Society of London. Series A. Mathematical and Physical Sciences* 211.1107 (1952), pp. 564–587.

[18] Leonard V Lopes, David D Boyd Jr, Douglas M Nark, and Karl E Wiedemann. “Identification of spurious signals from permeable Ffowcs Williams and Hawkings surfaces”. In: *American Helicopter Society (AHS) International Annual Forum and Technology Display*. NF1676L-25336. 2017.

[19] S Mendez, M Shoeybi, SK Lele, and P Moin. “On the use of the Ffowcs Williams-Hawkings equation to predict far-field jet noise from large-eddy simulations”. In: *International Journal of Aeroacoustics* 12.1-2 (2013), pp. 1–20.

[20] Thomas J Mueller. *Aeroacoustic measurements*. Springer Science & Business Media, 2002.

[21] Ajay K Prasad. “Stereoscopic particle image velocimetry”. In: *Experiments in fluids* 29.2 (2000), pp. 103–116.

[22] Markus Raffel, Christian E Willert, Fulvio Scarano, Christian J Kähler, Steve T Wereley, and Jürgen Kompenhans. *Particle image velocimetry: a practical guide*. springer, 2018.

[23] Fulvio Scarano. “Iterative image deformation methods in PIV”. In: *Measurement science and technology* 13.1 (2001), R1.

[24] Fulvio Scarano and M.L. Riethmuller. “Advances in iterative multigrid PIV image processing”. In: *Experiments in Fluids* 29 (Apr. 2012), S051–S060. DOI: 10.1007/s003480070007.

[25] Fulvio Scarano and Michel L Riethmuller. “Advances in iterative multigrid PIV image processing”. In: *Experiments in fluids* 29.Suppl 1 (2000), S051–S060.

[26] Philippe R Spalart, Kirill V Belyaev, Mikhail L Shur, Mikhail Kh Strelets, and Andrey K Travin. “On the differences in noise predictions based on solid and permeable surface Ffowcs Williams-Hawkings integral solutions”. In: *International Journal of Aeroacoustics* 18.6-7 (2019), pp. 621–646.

[27] Sauro Succi. *The Lattice Boltzmann Equation for Fluid Dynamics and Beyond*. New York, NY, USA: Oxford University Press, 2001.

[28] Christopher KW Tam. "Computational aeroacoustics-Issues and methods". In: *AIAA journal* 33.10 (1995), pp. 1788–1796.

[29] Christopher KW Tam. "Computational aeroacoustics: An overview of computational challenges and applications". In: *International Journal of Computational Fluid Dynamics* 18.6 (2004), pp. 547–567.

[30] Cameron Tropea, Alexander L Yarin, John F Foss, et al. *Springer handbook of experimental fluid mechanics*. Vol. 1. Springer, 2007.

[31] C Wagner. *Large-Eddy Simulation for Acoustics*. Cambridge University Press, 2007.

[32] Jerry Westerweel and Fulvio Scarano. "Universal outlier detection for PIV data". In: *Experiments in fluids* 39 (2005), pp. 1096–1100.

[33] Christian Willert. "Stereoscopic digital particle image velocimetry for application in wind tunnel flows". In: *Measurement science and technology* 8.12 (1997), p. 1465.

[34] J. E. Ffowcs Williams and D. L. Hawkings. "Sound Generation by Turbulence and Surfaces in Arbitrary Motion". In: *Philosophical Transactions of the Royal Society of London* 264.1151 (1969), pp. 321–342.

[35] Victor Yakhot and Steven A Orszag. "Renormalization group analysis of turbulence. I. Basic theory". In: *Journal of scientific computing* 1.1 (1986), pp. 3–51.

4

ISOLATED PROPELLER: AEROACOUSTIC INVESTIGATION

This chapter presents an experimental investigation of a propeller operating at low-Reynolds numbers and provides insights into the role of aerodynamic flow features on both propeller performances and noise generation. A propeller operating at a tip Reynolds number regime of 43000-43800 is tested in an anechoic wind tunnel at advance ratio ranging from 0 to 0.6. Noise is measured by means of a microphone array, while aerodynamic forces with load and torque cells. Oil flow visualizations are used to show the flow patterns on the blade surface, whereas phase-locked stereoscopic Particle Image Velocimetry (PIV) measurements are carried out to analyse the flow at 60% of the blade radius. The pressure field around the blade section has been computed from the PIV velocity data. Results reveal a complex flow field with the appearance of a laminar separation bubble at the suction side of the blade. The separation bubble moves toward the leading edge and reduces in size as the advance ratio decreases. At an advance ratio equal to 0.6, the flow field is characterized by a laminar separation without reattachment. This causes vortex shedding responsible for a high-frequency hump in the far-field noise spectra.

Parts of this chapter have been published in AIAA Journal 2021 [13].

4.1. INTRODUCTION

As outlined in Chapter 1, the interest in the aeroacoustics of rotors operating at a chord Reynolds number Re_c ranging from 10^4 to 10^5 has considerably increased in recent years due to the proliferation of UAVs and PAVs. Propellers are the primary propulsion system for these vehicles, providing the thrust-to-weight ratio necessary for hovering and maneuvering near obstacles. The fast expansion of the drones market will be closely related to rotor noise abatement.

Several studies focusing on airfoils at low Reynolds numbers ($Re_c < 5 \cdot 10^5$) demonstrated their high sensitivity of the performance to the Reynolds number itself and complex boundary layer physics including laminar separation, transition and reattachment [35, 10, 31, 18]. Consequently, the design and optimization of propellers operating at low-Reynolds number are currently limited. Serre at al. [29] addressed the challenge of designing a quiet and efficient propeller by developing a numerical tool that combines a low-fidelity aerodynamic model (based on Xfoil [8]) with an acoustic model. A reduction of 10 dB is observed between the conventional rotor and the optimized one. Despite the satisfactory result, the authors highlight the limitations of using a low-fidelity method as aerodynamic solver for such low-Reynolds numbers. Comparisons with experimental data indicate that the airfoil drag coefficient is underestimated by nearly 30% over a wide range of angle of attacks and the lift coefficient is overestimated by up to approximately 40%. Moreover, the boundary layer thickness (an input parameter for the broadband noise model) exhibits a different trend compared to experimental results. The experimental works of Brandel and Mueller [4] and Kim et al. [16] on airfoils at a maximum $Re_c = 2 \cdot 10^5$ show that the integral boundary layer parameters are strongly influenced by the presence of a laminar separation bubble. The displacement thickness increases rapidly after a laminar separation and decreases at transition onset, whereas the momentum thickness exhibits a sudden increase near the transition location, trends typically not captured by low-fidelity methods.

In Chapter 2 is shown that at low Reynolds numbers and moderate angles of attack, airfoils frequently undergo laminar boundary layer separation. The resulting separated shear layer may transition to turbulence and reattach, forming a laminar separation bubble (LSB). The characteristics of the LSB, including its size and position, are influenced by the angle of attack, Reynolds number, and airfoil geometry. As the angle of attack or Reynolds number increases, the LSB shifts toward the leading edge and shortens until it bursts, leading to increased drag and decreased lift. On the other hand, lowering the Reynolds number can cause the LSB to burst at lower angles, negatively affecting the lift curve slope. The angle of attack at which the LSB burts depends heavily on Reynolds numbers and airfoil design. Various studies confirm these observations across different airfoils [1, 24, 38]. Coherent structures generated into the separated shear layer [14, 5, 16] can result in vortex shedding noise, which will be discussed in subsequent sections.

The above illustrated low-Reynolds number aerodynamic characteristics are expected to have also an influence on the noise generation. Research on the aeroacoustics of small-scale propellers [30, 23] show that noise spectra exhibit both tonal and broadband contributions from turbulent boundary layer trailing edge noise and turbulent ingestion noise at the leading edge. While these classical noise sources are well-studied, the impact of low Reynolds number phenomena such as LSB on propeller noise remains un-

certain. Studies on steady airfoils prove that the vortex shedding from a LSB can generate tonal or quasi-tonal noise. This is demonstrated by the experimental work of Pröbsting and Yarusevych [26], which found that on a NACA0012 airfoil the passage of coherent vortices (generated from a LSB) over the trailing edge produces tonal noise. Furthermore, Wu et al. [36] linked the near wake shedding from a LSB to a high-frequency hump in the far-field noise spectra.

Passive methods for noise reduction of small propellers are also of great interest. Yang et al. [37] adopted different design of sawtooth trailing edge serration on a UAV propeller. A broadband noise reduction is observed for all the serrated models, up to a maximum of 8 dB. Lee et al. [17] conducted experimental testing on rotors with flat tip trailing edge serration, i.e. the sawtooth serration where the sharp tip is cut in order to become flat, and rectangular serrations. The flat tip serrated propeller showed the highest broadband noise attenuation at 3000 rpm, corresponding to an overall noise reduction of 5.8 dBA. The main mechanism for noise reduction of serrated propellers is associated to destructive scattering efficiency.

This chapter study the flow around the blade of a propeller operating at low-Reynolds numbers, and evaluate if the flow is attached/separated, if a laminar-to-turbulent transition is present and a LSB is formed. The knowledge about the flow behavior is then linked to the global aerodynamic performance and the noise generation. In particular, an attempt to shed more light on the contribution of low-Reynolds phenomena on the noise emission is given. To this purpose, surface oil-flow visualizations and phase-locked stereoscopic PIV of a cross-sectional plane of the blade has been performed for the propeller operating at advance ratio ranging between 0 and 0.6. The characteristics of the boundary layer are retrieved from the analysis of the oil-flow patterns, rms velocity, spanwise vorticity distribution and static pressure, calculated from the PIV velocity. Far field noise measurements have been performed through a linear array of microphones. For each condition, thrust and torque time signals have also been acquired by means of load and torque cells. In addition, the experimental challenges faced in order to get accurate measurements, such as the uncertainty due to variations of rotational speed and motor noise contamination, are described.

The chapter is organized as follows. In Sect. 4.2 the propeller geometry,the experimental setup and the experimental test matrix are presented. In Sect. 4.3 the experimental uncertainties are illustrated. Finally, in Sect. 4.4 the characteristics of the flow around the blade, the aerodynamic performances and the noise emitted are discussed.

4.2. EXPERIMENTAL SETUP AND PROCEDURES

The experiments have been carried out in the Anechoic Tunnel (A-Tunnel) at the low speed laboratory of TU Delft. The A-Tunnel is a vertical, open-jet wind tunnel, where the surrounding of the nozzle exit consists of an anechoic chamber with the walls covered by melamine wedges. A circular exit nozzle with a diameter of 0.60 m and a contraction ratio of 15:1 has been employed for this study. The maximum flow speed that the A-Tunnel is able to provide with this nozzle is 35 m/s, the mean streamwise velocity is uniform whithin 0.6% of freestream velocity, the turbulence intensity is 0.14% at 2.5 m/s and decreases below 0.1% with a flow velocity above 10 m/s. A description of the tunnel, with details of the flow and acoustic characterizations, can be found in the paper

of Merino-Martinez et al. [20].

4.2.1. PROPELLER DESIGN

The propeller used for this study has been obtained from an APC 9x6, diameter of 9" (22.86 cm) and pitch of 6" (15.24 cm), a model aircraft two-bladed propeller which routinely operates at low Reynolds number. The diameter has been scaled up to D = 30 cm and each profile has been reshaped with a NACA 4412 airfoil. An elliptical section at the root has been merged with the first profile section starting from a radius of 1 cm (Fig. 4.1a). An in-house tool, made by a combination of Matlab and SolidWorks software, has been employed for the blade design. The chord and twist angle distributions of the blade over the radial distance r from the hub center are shown in Fig. 4.1b. The maximum chord is c_{max} = 3.4 cm and the maximum twist angle is β_{max} = 43.6 °.

The propeller, made of aluminium alloys, has been manufactured using CNC machining at TU-Delft with 0.4 to 0.8 μm Ra finish. This manufacturing method guarantees high accuracy and reduce at most the surface imperfections, which can induce vibrations during the measurements and can affect the quality of the flow around the blades.

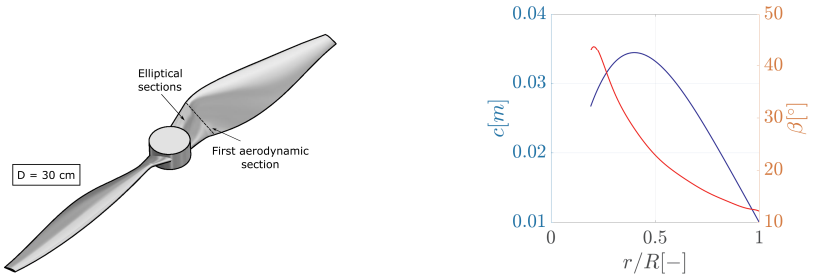

(a) (b)

Figure 4.1: Propeller CAD geometry (a). Blade chord and pitch angle distributions (b).

4.2.2. PROPELLER TEST RIG

The test rig, mounted in the A-Tunnel, is shown in Fig. 4.2a. The propeller is connected to a profiled aluminium nacelle of 5 cm diameter for minimum interference with the propeller flow. Within the nacelle, a motor, an encoder, a load cell and a torque cell are assembled. The nacelle is supported by stiffened hollow aluminum NACA 0012 profiles of 6 cm chord, inside which all the cablings are housed and remotely connected to the instrumentation outside the jet. The entire structure is held up above the nozzle of the tunnel by 4 steel-wire tubes of 2 cm diameter fixed to the tunnel to minimize vibrations and interference. The different parts of the rotor drive-train are shown in Fig. 4.2b with different colors: in yellow the encoder disk, in red the motor, in gold the torque cell, in violet a load cell, in grey connectors.

The propeller is driven by an electrical brushless motor Leopard Hobby 3536-5T 1520 KV with a diameter of 27.8 mm and maximum power of 550 W. The motor is powered by a Delta Elektronika DC power supply with a voltage range of 0 - 15 V and a current

range of 0 - 100 A. The motor rotational speed is measured by means of a US Digital EM1 transmissive optical encoder, coupled with a US Digital disk of 25.4 mm diameter and 200 cycles per revolution (1.8 deg of uncertainty on the position).

Rotor thrust is measured using a uniaxial Futek LSB200 load cell excited with 5 VDC. The load cell is characterized by a maximum capacity of 22.2 N, nonlinearity and histeresis of ± 0.1 % of RO and an operating temperature between -50 to 90 $^{\circ}C$. The torque is measured using a Transducer Techniques RTS-25 torque sensor excited with 10 VDC. It has a maximum capacity of 0.18 Nm, nonlinearity and histeresis of ± 0.1 % of RO and an operating temperature between -54 to 93 $^{\circ}C$. The thrust and torque signals are acquired by a National Instrument acquisition board with a sampling frequency of 5 KHz and an acquisition time of 15 s. Thrust and torque coefficients and propulsive efficiency are calculated using the following definitions:

$$C_T = \frac{T}{\rho n^2 D^4} \quad C_Q = \frac{Q}{\rho n^2 D^5} \quad \eta_{prop} = \frac{C_T J}{2\pi C_Q} \tag{4.1}$$

where T is the thrust in N, Q the torque in Nm, ρ the air density in kg/m^3, n the propeller rotational frequency in Hz, D the propeller diameter in m and $J = V_\infty / nD$ the advance ratio, being V_∞ the axial flow speed in m/s.

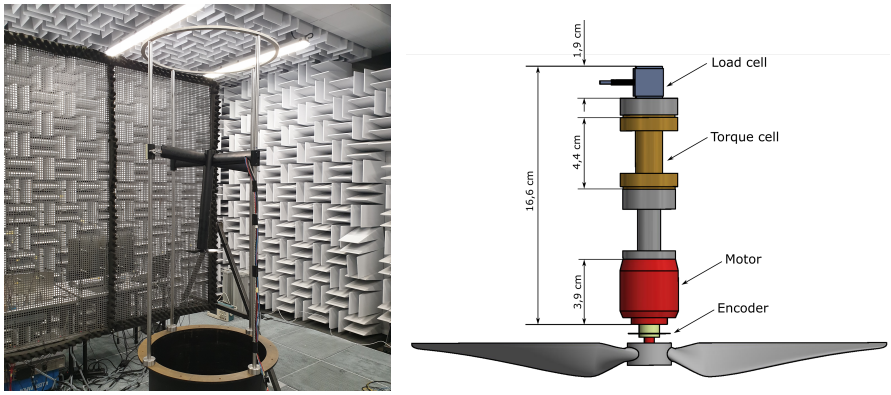

(a) (b)

Figure 4.2: Propeller setup mounted in the A-Tunnel at TU-Delft (a). View of the propeller drive train: from bottom to top, in yellow the encoder disk, in red the motor, in grey a connector, in gold the torque cell, in grey a second connector, in violet a load cell (b).

4.2.3. ACOUSTIC MEASUREMENTS APPARATUS

A planar microphone array, sketched in Fig. 5.1, located in a plane perpendicular to the propeller plane, has been used. The array is constituted by 13 G.R.A.S. 40PH analog free field microphones, having a diameter of 7 mm, a frequency range between 10 Hz and 20 KHz and a maximum SPL of 135 dB. The microphones have been calibrated using a G.R.A.S. 42AA pistonphone with a calibration level of 114 dB re. 20 μPa. The uncertainty of the calibration is less than 0.09 dB (99% confidence level). The data acquisition system consists of a National Instrument PXIe-4499 sound and vibrations data acquisition

module. As Fig. 5.1 shows, the array is at 4D (1.2 m) in the y direction with respect to the propeller axis. The distance between each microphone is 0.5D (0.15 m), the microphone 7 is at the propeller plane, the microphone 1 is 3D (0.9 m) above the propeller plane and the microphone 13 is 3D below. Microphone voltages have been recorded for a duration of 30 s at a frequency rate of 50 KHz. The acoustic signals are separated in 300 Welch blocks with 50% overlap, corresponding to a bandwidth of 10 Hz.

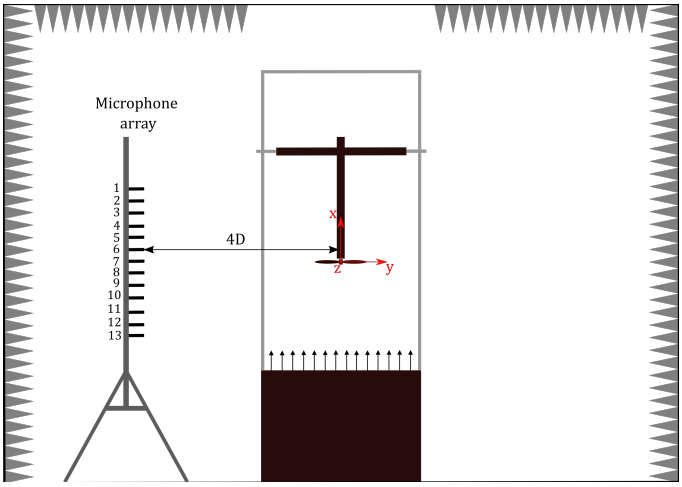

Figure 4.3: Microphone array configuration.

4.2.4. FLOW ANALYSIS AND PRESSURE COMPUTATION

Stereoscopic PIV measurements have been conducted to study the flow over the cross-section of the blade at $r/R = 60\%$ ($c = 3$ cm). The stereoscopic PIV setup is discussed in Sect. 3.4 and illustrated in Fig. 3.4.

Following the approach of Ragni et al. [27], the flow around the blade is assessed with respect to a non-inertial reference frame that rotates at the propeller's rotational speed ω. In this approach, the rotational velocity component of the blade section $\vec{V}_T = \vec{\omega} \times \vec{r}$ (with $\vec{r}$ being the position vector), is subtracted from the x-component of the PIV velocity fields. Given that the chord of the blade section is small compared to the propeller radius, $\vec{V}_T$ can be approximated as a translational motion aligned with the x-component of the flow velocity.

Assuming that no thermal energy is added, the total temperature in the relative frame is constant and the PIV velocity data can be used to compute the pressure field p around the blade section [22]. This indirectly gives information about the boundary layer characteristics.

The pressure is retrieved by integration of the pressure gradient as obtained from the Navier Stokes momentum equations (under incompressible flow conditions) with velocity input from PIV, neglecting the Reynolds turbulent stresses, which were found to give a negligible contribution in the pressure computation:

$$\nabla \cdot (\nabla p) = \nabla^2 p = -\rho \nabla \cdot (\vec{V}_R \cdot \nabla) \vec{V}_R \tag{4.2}$$

The integration is carried out by combining the pressure gradient via a Poisson equation and validated through a finite marching algorithm as described by Oudheusden [22]. As boundary conditions, the pressure is prescribed on the boundaries where the flow can be considered isentropic (Dirichlet boundary conditions) and the pressure gradient is imposed on the remaining boundaries (Neumann conditions). The final extrapolation on the airfoil geometry is carried out by using the gradient on the first point with finite differences. The blade section at 60% radius is selected as one of the most representative out-board profiles, where the out-of-plane gradients are negligible compared to the in-plane gradients. In the vicinity of the blade, the in-plane spatial velocity derivatives are on the order of $10^4\ s^{-1}$, while the expected changes in the out-of-plane velocity component v_z are approximately $10^2\ s^{-1}$ (assuming v_z doubles over a spanwise strip length equal to $R/10$). Consequently, the in-plane pressure can be reconstructed on the airfoil with sufficient accuracy. Once the pressure is integrated, the pressure coefficient can be calculated as follow:

$$c_P = \frac{p - p_\infty}{0.5 \rho_\infty V_{R\infty}^2} \tag{4.3}$$

where the subscript $_\infty$ refers to free-stream conditions.

4.2.5. EXPERIMENTAL CONDITIONS

The propeller has been operated both in hover and free-stream flow conditions. Hence, the rotational speed has been kept constant to 4000 rpm to limit the variation of Re number and the advance ratio J has been varied. When J increases (free-stream velocity V_∞ increases), the angle of attack over the blade decreases. This is evident from the drawing (see Fig. 4.4) of two velocity triangles for a generic blade section at the same tangential velocity and two different advance ratios $J_2 > J_1$, corresponding to $V_{\infty_2} > V_{\infty_1}$. In the figure θ is the pitch angle, α is the angle of attack, $\phi = \theta - \alpha$ is the inflow angle and a and a' are the tangential and radial induction coefficients. The experimental test matrix is summarized in Table 4.1. For each case the corresponding value of advance ratios J and Reynolds number Re_{60}, based on the chord at 60% of the span (which is the location chosen for the flow measurements), are indicated.

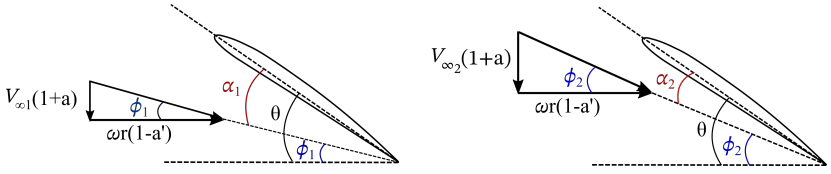

Figure 4.4: Velocity triangles for a fixed blade section at two different free-stream velocity $V_{\infty_1} > V_{\infty_2}$.

Table 4.1: Experimental test matrix.

Case	ω [rpm]	V_∞ [m/s]	J	Re_{60}
1	4000	0.0	0.0	$7.67 \cdot 10^4$
2	4000	2.4	0.12	$7.68 \cdot 10^4$
3	4000	4.8	0.24	$7.73 \cdot 10^4$
4	4000	8.0	0.4	$7.83 \cdot 10^4$
5	4000	12	0.6	$8.04 \cdot 10^4$

4.3. EXPERIMENTAL UNCERTAINTY

4.3.1. RPM VARIABILITY IN THE MEASUREMENTS

The first uncertainty that has been taken into account is the variation of the propeller rotational speed during the measurements. A variation of rpm causes a variation of the blades lift, which is directly associated to the loads and tonal noise emission. The rpm variation has been calculated from the encoder signal, acquired simultaneously with the loads and noise measurements. The encoder signal is constituted by a one-per-revolution signal and the rpm variation in time is retrieved from the time difference between two pulses. The hover condition exhibits the higher rpm variation, i.e. ±20 rpm of deviation from the mean value, at $J = 0.12$ the variation is ±6 rpm, while the other advance ratios show an rpm variation between 2 and 4.

4.3.2. LOADS AND NOISE UNCERTAINTIES

The uncertainty of thrust and torque have been computed from the scatter of the measurements on different days, and they have been found to be 0.1 % and 0.05 %, respectively. The uncertainty due to the variability of the propeller rotational speed is calculated retrieving the thrust and torque values from chunks of signals of 10-revolutions length and computing the standard deviation. The uncertainty found for the thrust measurements is equal to 4.8 % at $J = 0$, 3.6 % at $J = 0.12$ and between 0.6 % and 1.1 % for the other advance ratios. On the other side, the torque uncertainty is 0.1 % at $J = 0$ and between 0.02 % and 0.06 % for the other advance ratios.

The signal from the encoder, acquired simultaneously with the noise measurements, has also been used to calculate the uncertainty of the BPF 1 level associated to a variation of the propeller rotational speed during the measurements. Figure 4.5 (left) shows the pressure signals over time measured with microphone 7, at 4000 rpm and $J = 0.0$, 0.24 and 0.6 (from top to bottom) together with the encoder signals, while Fig. 4.5 (right) shows the propeller rpm variation in time. For clarity's sake, only 0.2 seconds out of 30 seconds of signals are shown. Following the same approach used for the loads uncertainty, the pressure signals have been cut in chunks of 10 revolutions and for each of them the first BPF tone SPL has been computed and the standard deviation evaluated. The results for each advance ratio and three microphones are reported in Table 4.2. The maximum uncertainty in hover is about 2 dB and is higher with respect to $J = 0.12$, 0.24,

0.4 cases, because of the higher variation of rpm over time. The J = 0.6 case presents uncertainty values similar to the hover case, this is due to the low frequency component in the pressure signal, clearly visible from Fig. 4.5 (bottom-right). It is supposed that this effect is associated with the tunnel flow jet noise, whose contribution is not negligible at low frequencies with increasing flow velocity.

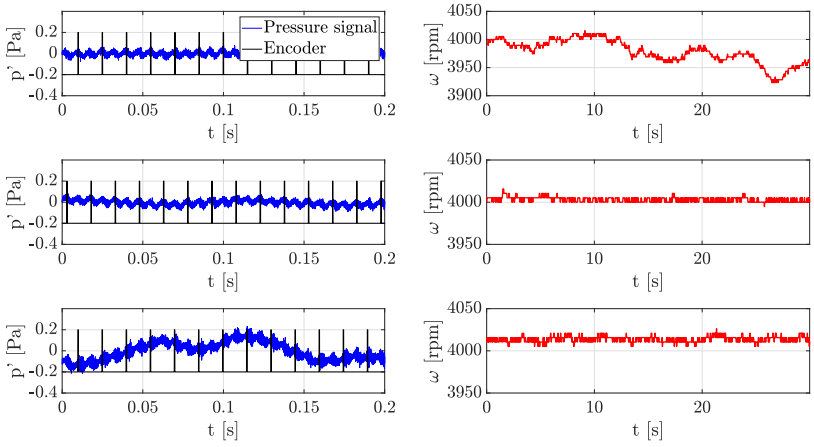

Figure 4.5: Pressure and encoder signal (left) and velocity signal (right) over time at 4000 rpm and J = 0.0, 0.24, 0.6 (from top to bottom).

4.3.3. PIV UNCERTAINTY

In the stereoscopic PIV measurements, a self-calibration through a disparity correction procedure is used [34], in order to refine the target calibration by correlation of the particle images between the two cameras. The residual average misalignment is equal to 0.03 px. The phase-locked PIV measurements of this study are mainly affected by random uncertainty, as the cross-correlation uncertainty. The effect of this error scales with $1/\sqrt{N}$ (where N is the number of images), due to statistical convergence. The cross-correlation uncertainty is expected to be in a range of 0.05-0.1 px [33], for a multi-pass algorithm ending with a windows size of 24 x 24 px. The corresponding error based on

Table 4.2: First BPF tone level uncertainty at 4000 rpm due to rotational speed variations.

Mic	**Std [dB]**				
	$J = 0.0$	$J = 0.12$	$J = 0.24$	$J = 0.4$	$J = 0.6$
1	2.13	1.54	0.65	1.37	2.38
7	1.08	0.94	0.42	0.88	1.89
13	1.34	0.87	0.44	1.05	2.06

the value of maximum instantaneous velocity, encountered at the airfoil suction side, is of the order of 0.9%, while for the minimum velocity, encountered at the airfoil leading edge, is equal to 5%. Therefore, the overall uncertainty on the maximum and minimum mean velocities are assessed at 0.04% and 0.22%. On the other side, the overall uncertainty relative to the maximum and minimum velocity fluctuations are of the order of 1.7% and 14%, respectively. The uncertainty due to spatial resolution depends on the size λ of the structures to be resolved and on the interrogation window size ws, in this case equal to 0.4 mm. The vortical structures identified in the instantaneous images and localized in the airfoil wake have a dimension of 0.8 to 1.5 mm, creating a mean wake profile of about 2.5 mm thickness. The normalized windows size of $ws/\lambda = 0.06$ can be converted into a spatial resolution error of <5% for such structures, as shown by Schrijer and Scarano [28].

4

4.3.4. MOTOR AND BACKGROUND NOISE

In Fig. 4.6 the combined propeller/motor noise at 4000 rpm and three different advance ratios, $J = 0$, 0.24, 0.6 (corresponding to $V_\infty = 0$, 4.8, 8 m/s), measured with microphone 7 of the array (see Fig 5.1), has been compared with the motor noise without propeller and with the background noise of the facility. The frequency axis of each plot is normalized with respect to the the blade passing frequency $BPF = Bn$, where B is the number of blades and n is the propeller rotational frequency in Hz. The background noise (dashed black line) is comparable with the propeller broadband noise in the low-frequency range at $J = 0.6$ ($V_\infty = 8$ m/s). When the advance ratio is below 0.6, the signal to noise ratio is higher than 10 dB over almost the entire spectrum. The electrical motor noise (dashed light blue line) exhibits a series of discrete tones in the range BPF 5 - BPF 100 (660 Hz - 13 kHz) and a broadband level that does not affect the noise measurements, being more than 10 dB lower of the propeller noise over the entire frequency range for all the cases. The imperfect blade loading balancing causes the rise of harmonics at BPF 0.5, 1.5 and 2.5.. As a final remark, an additional source of tonal noise in the experiment is constituted by vibrations of test-rig and rotor. The quantification of the latter is left for future experiments

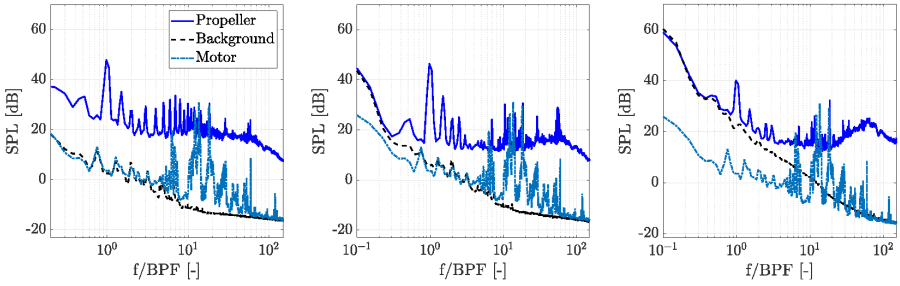

Figure 4.6: Comparison between propeller noise and background/motor noise at 4000 rpm and $J = 0$ (left), $J = 0.24$ (middle), $J = 0.6$ (right).

4.4. AERODYNAMIC AND AEROACOUSTIC CHARACTERIZATION

4.4.1. OIL FLOW VISUALIZATION

Oil flow visualizations of the suction side of the propeller blade at J = 0.24 (V_∞ = 4.8 m/s), (b) J = 0.4 (V_∞ = 8 m/s), (c) J = 0.6 (V_∞ = 12 m/s) are shown in Fig. 4.7. Beside the pronounced radial flow, the oil flow patterns clearly reveal the presence of a laminar separation bubble for the cases J = 0, 0.24, and 0.4. The thickness of the oil is larger in portions of the blade surface where the chordwise pressure gradient is almost zero, i.e. in LSB and regions where the flow is simply separated, as at the root. The chordwise size of the LSB is determined from the distance between the laminar separation and reattachment lines, indicated in the figure with S and R respectively. As the advance ratio increases from 0 to 0.4, the angle of attack over the entire blade decreases and the LSB is expected to increase in length and move toward the trailing edge. This trend has been observed for steady airfoils from several authors [2, 4]. For finite wing the similarity with airfoils in LSB topology is restricted to inboard regions with weakly three dimensional flow [32]. Near the tip, the wingtip vortex reduces the effective angle of attack and the LSB is delayed and enlarged [11, 1]. Moreover, the LSB is washed out in the tip region wet by the wingtip vortex.

At J = 0 the LSB is not present at the tip region and, as the outboard region is approached, the LSB has a curved separation line, i.e. it shortens and moves closer to the leading edge. The first phenomenon is hypothesized to be caused by the blade vortex interaction, that washes out the LSB at the tip. The curved separation line is also ascribed to a tip vortex effect, in fact, as soon as the vortex is released, it is convected mostly inward (following the streamtube), as shown in a complementary work from the authors about the same propeller [6]. This creates upwash on the blade outboard regions with a consequent increase of the angle of attack. The local change of α could explain the movement and shortening of the LSB. As J increases the tip vortex loose his strength and is convected downstream with and higher velocity. This could be the reason why the tip vortex does not seem to have any influence for the cases J = 0.24 and 0.4, showing a LSB that extends up to the tip. From a qualitative observation the length of the LSB increases in the spanwise direction (from the root to the tip) due to the decrease of α. Furthermore, the case J = 0.4 exhibits a wider LSB with respect to J = 0.24 due to the lower α over the entire blade. Finally, the case J = 0.6 does also not manifest any tip vortex effect. Since this case corresponds with the lowest α over the blade, the separation line is delayed toward the trailing edge. It is not clear if the shear layer reattaches at the thin black region at the trailing edge or stays separated. In the latter case, it would mean that the LSB bursts at low angles of attack, as found by Park et al. [24] and Kim at al. [16]. This will be further examinated in the following sections.

The separation bubble characteristics depend also on the Reynolds number, but the dependence on the angle of attack is stronger. In the present study, when the advance ratio increases from 0 to 0.6, the corresponding chord based Reynolds number increase is 3700 and it is considered negligible.

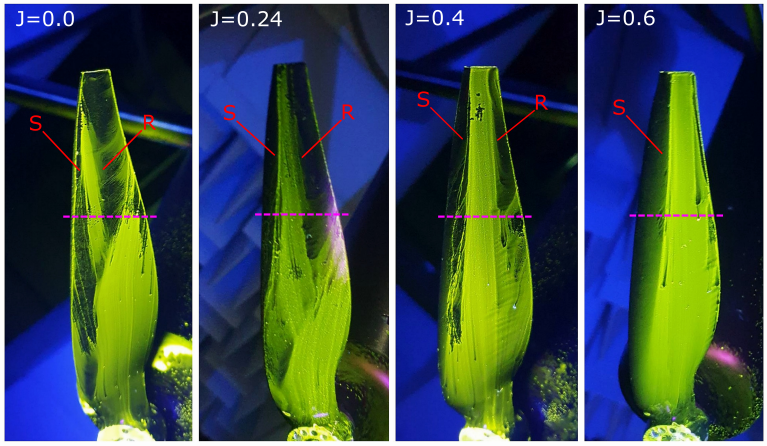

Figure 4.7: Oil flow visualizations of the suction side of the blade at 4000 rpm and J = 0, 0.24, 0.4 and 0.6.

4.4.2. AERODYNAMIC PERFORMANCE

Figure 4.8 shows the experimental thrust and torque coefficients and the propulsive efficiency as function of the advance ratio J. The parabolic relation between thrust coefficient and advance ratio for small-scale propellers has been found also from other authors [19, 3]. The torque coefficient exhibits an almost constant part between J = 0 and 0.4. At this regime, the sections of the blade closer to the root that are separated contribute to most of the torque with high drag values. As the advance ratio increases, the blades section angle of attack reduces below the stall angle and the torque decreases as a consequence of less drag. The propulsive efficiency is characterized, as expected, by an opposite trend: as the torque decreases, the propulsive efficiency increases (see Eq. 4.1). The maximum is equal to $\eta_{prop} = 0.78$ at $J = 0.6$.

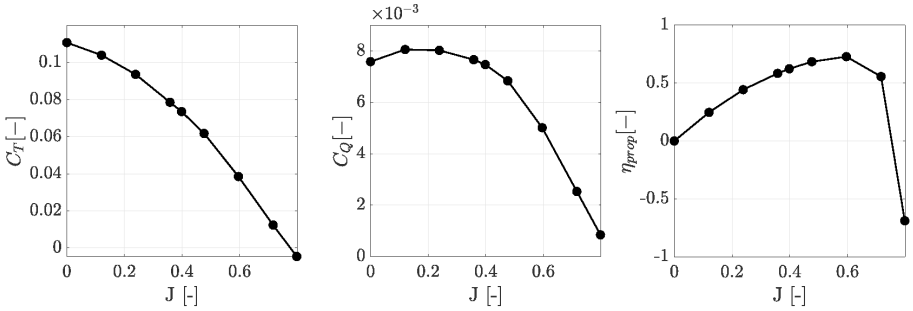

Figure 4.8: Thrust coefficient (left), torque coefficient (middle), propulsive efficiency (right) versus J at 4000 rpm.

4.4.3. MEAN AND RMS VELOCITY FIELDS

Figure 4.9 shows the distribution of dimensionless relative velocity and rms velocity around the cross-section at the 60% of the blade radius (highlighted by the dashed line in Fig. 4.7) at $J = 0$ (a), $J = 0.24$, (b) $J = 0.4$, (c) $J = 0.6$. The black region constitutes the airfoil surface, while the white parts adjacent to the surface represent regions where the velocity vectors are corrupted due to small movements of the blade during the phase-locked measurements or to surface reflections. As expected, most of the flow acceleration occurs at the suction side of the airfoil and only partially at the pressure side. The decrease of velocity in the wake region is also well captured. As J increases, the velocity at suction side decreases and the stagnation point moves toward the leading edge. This corresponds to a reduction of the angle of attack, in agreement with the description in Section 4.2.5. The maximum velocity reached at $J = 0$ (Fig. 4.9a) is equal to 1.58 times the relative free-stream velocity (V_{R_∞}) and at $J = 0.6$ (Fig. 4.9d) is 1.3 V_{R_∞}.

The rms velocity contours show a region at the suction side and in the wake of the airfoil where a considerable increase occurs. When the angle of attack decreases (J increases), the chordwise point where the rms velocity increases moves toward the trailing edge. The region where the rms velocity suddenly starts to increase may be associated with the location of boundary layer transition onset, which is in the vicinity of the reattachment point. Due to the poor near wall resolution, the exact location of boundary layer transition on the airfoil suction side cannot be estimated, however the following is evident. At $J = 0$ (Fig. 4.9a) the rms velocity starts increasing at about $x/c = 0.4$ with values exceeding the 10% of free stream velocity. The cases $J = 0.24$ (Fig. 4.9b) and $J = 0.4$ (Fig. 4.9c) present similar characteristics: the higher rms velocity values are confined in a thin region close to the trailing edge and wake, from about $x/c = 0.8$ for the first case and $x/c = 0.9$ for the second one. The values are around to 12% of free-stream velocity. Interestingly, the case $J = 0.6$ (Fig. 4.9d) exhibits a rms velocity amplification only in the wake with values reaching the 22% of free-stream velocity. This strengthens the idea of separation without reattachment for the case $J = 0.6$, as conjectured from the oil-flow results. The turbulent flow in the wake is in part associated with amplified unstable waves originated in the separated shear layer, which ultimately transforms in wake vortex shedding [25]. Figure 4.10 shows the instantaneous spanwise vorticity component around the trailing edge and wake for the cases $J = 0.4$ and 0.6. Coherent structure can be clearly identified in the wake region for both cases. At $J = 0.6$ the length scale of the vortices is approximately doubled. Indeed, when the flow fails to reattach, as at $J = 0.6$, the vortex structures increase in length, as observed by Yarusevich et al. [38] and this would explain the wider wake with higher velocity fluctuations with respect to the other cases.

4.4.4. PRESSURE FIELDS

The pressure fields have also been computed from the integration of the PIV velocity fields, by using the method described in 4.2.4. Figures 4.11a, 4.11c, 4.11e, 4.11g display the pressure coefficient C_p distributions around the blade section, respectively, at $J = 0$, $J = 0.24$, $J = 0.4$, $J = 0.6$. The results are consistent with the velocity distributions, in fact the intensity of the suction peak is increasing as the advance ratio increases. The minimum C_p is equal to -1.2 for the case $J = 0$ and -0.6 for $J = 0.6$. The pressure coefficient at the

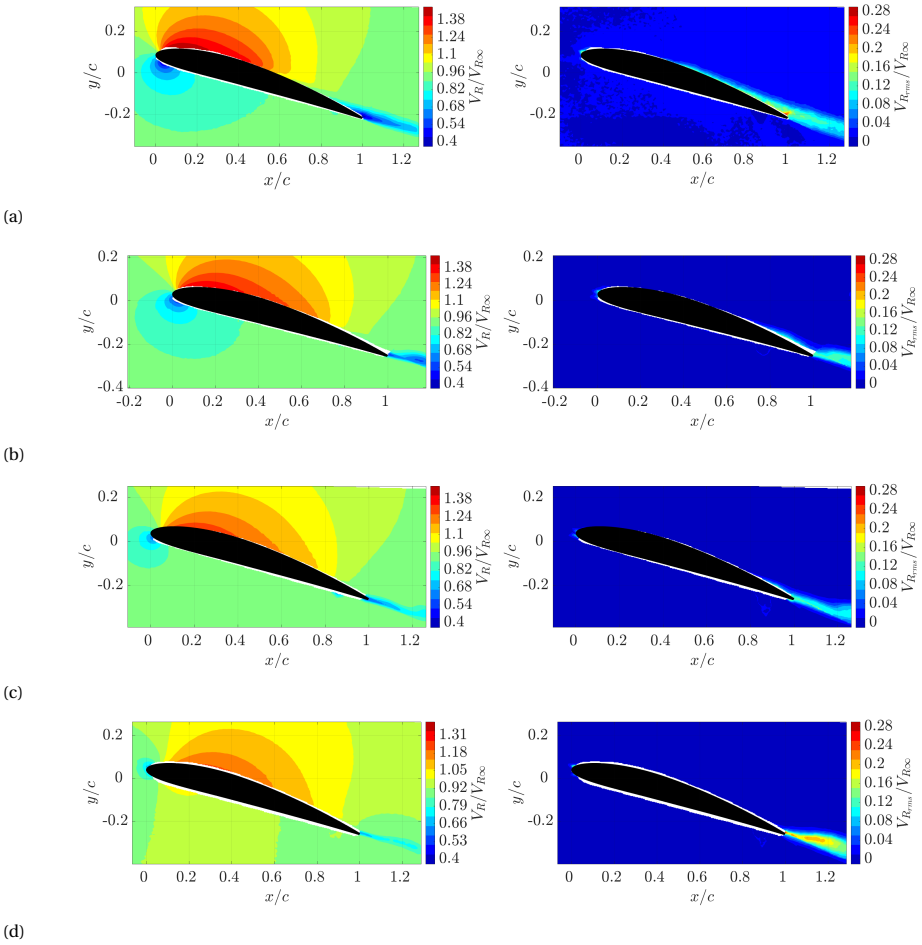

Figure 4.9: Mean and rms velocity fields around the blade cross-section at $r/R = 0.6$ at 4000 rpm and $J = 0$ (a), $J = 0.24$ (b), $J = 0.4$ (c), $J = 0.6$ (c).

pressure side of the airfoil is almost constant, except for the region close to the leading edge.

For each of the four cases the C_p has been also extrapolated on the blade surface and plotted in Figs. 4.11b, 4.11d, 4.11f, 4.11h, furthermore comparisons with computations made via Xfoil [7] and the aerodynamic solver implemented inside *OptyδB*-BEMT tool are included. *OptyδB*-BEMT is a code for the prediction of the propeller performance based on a Blade Element Momentum Theory (BEMT), developed by the authors [6]. The BEMT aerodynamic solver is based on a boundary layer model by Drela and Giles [9] coupled with a second order panel method through an iterative process based on the boundary layer transpiration velocity. A pressure plateau can be identified in all the four figures. This is associated to regions where the boundary layer is separated. The increase of pres-

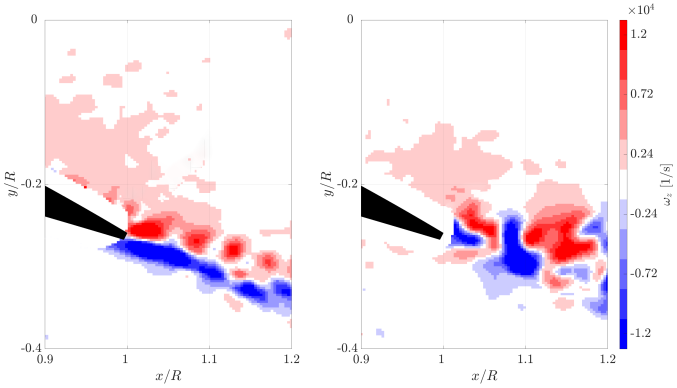

Figure 4.10: Instantaneous spanwise vorticity distribution around the trailing edge and wake of the blade cross-section at $r/R = 0.6$ at 4000 rpm and $J = 0.4$ (left), $J = 0.6$ (right).

sure after the plateau, observed for $J = 0$, 0.24 and 0.4, indicates a boundary layer reattachment. This confirms the presence of a LSB over the blade surface, as already shown by the oil flow. The trend of the LSB with the advance ratio, which can be retrieved by the extent and position of the pressure plateau, is also in agreement with the oil flow visualizations. As the advance ratio increases (angle of attack decreases) the region of nearly constant pressure becomes wider and moves toward the leading edge, which means that the bubble is decreasing in length and moving upstream. A similar trend of the LSB is predicted by Xfoil for these three cases, but the reattachment location is overestimated. When using *Opty∂B*-BEMT, the best match with the experimental curves has been found with an angle of attack of 1° smaller than Xfoil. The predicted trend is similar to Xfoil but with an earlier transition location and a better match at $J = 0$. The case $J = 0.6$ (Fig. 4.11f) exhibits a region of nearly constant pressure that extends up to the trailing edge. This supports the theory that the flow is separated up to the trailing edge. For this case Xfoil and *Opty∂B*-BEMT predict a long LSB with the reattachment point at $x/c = 0.9$ and 0.7 respectively.

4.4.5. FAR-FIELD NOISE

A comparison of noise spectra at a fixed rpm of 4000, by varying the advance ratio J from 0 to 0.6 is presented in Fig. 4.12. The spectra are computed using the pressure signals from microphones 3 (above the rotor plane), 7 (at the rotor plane) and 11 (below the rotor plane) of the array (see Fig. 5.1). All the microphone spectra present both discrete tones, mostly occurring at multiples of the BPF, and a broadband contribution. The most significant sources of broadband noise are: turbulent boundary layer trailing edge noise and turbulence ingestion noise at the leading edge. An additional near wake source is due to the vortex shedding originated from the laminar separation region.

For all the cases the trailing edge noise is mainly responsible for the broadband noise

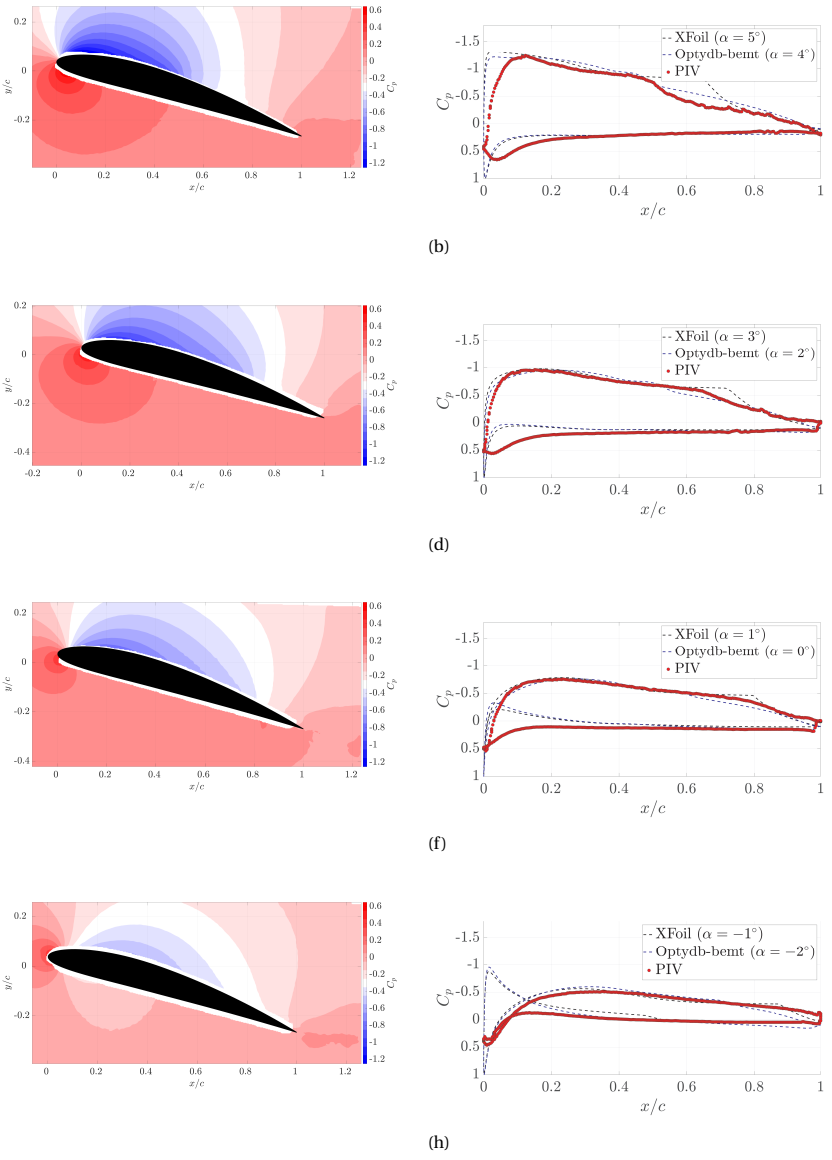

Figure 4.11: Pressure coefficients around the blade cross-section at $r/R = 0.6$ at 4000 rpm and $J = 0$ (a), $J = 0.24$ (c), $J = 0.4$ (e), $J = 0.6$ (g). Each field is combined with the corresponding surface pressure distribution (b), (d), (f), (h).

at low-mid frequency range, up to about BPF 20 (2.7 KHz). The small decrease of broadband noise in this frequency range when J switches from 0 to 0.4 can be partially related to the variation of the integral boundary layer parameters at the trailing edge, such as

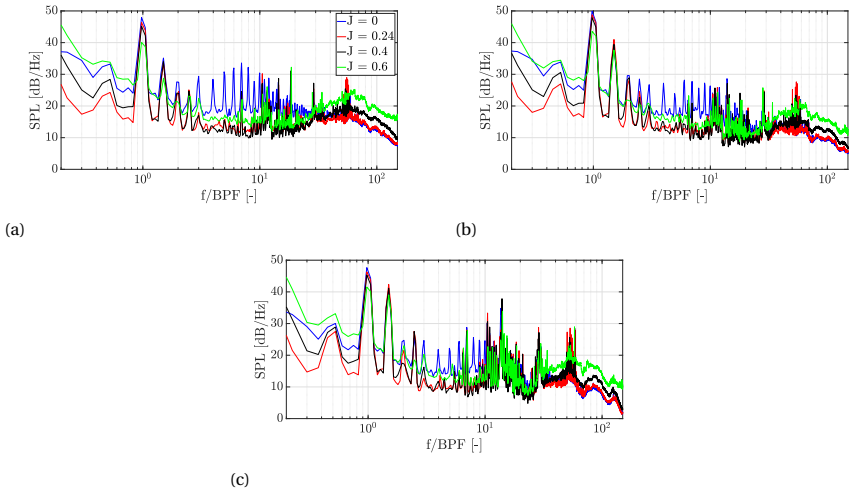

Figure 4.12: Comparison of noise spectra at 4000 rpm measured with mic 3 (a), mic 7 (b), mic 11 (c) by varying the advance ratio J from 0 to 0.6.

momentum, displacement and total thickness, which are expected to decrease when the laminar-to-turbulent transition point moves toward the trailing edge. For the hover case $J = 0$ the broadband level is several dB higher with respect to the other advance ratios. This can be attributed not only to trailing edge noise, but also to turbulence impingement noise at the leading edge [29]. The last condition to analyse is $J = 0.6$, corresponding with the lowest blade loading and angles of attack over the blade. In this case the broadband level is contaminated by the background noise up to BPF 1, while the small increase up to BPF 20 with respect to $J = 0.4$ is associated with a different growing trend of the boundary layer parameters due to the flow separation that extend over the entire blade span (see Fig 4.7). The vortex shedding originated from the laminar separation region, which ultimately transform into wake vortex shedding, constitutes another important source of noise responsible for the hump at high frequency, centered at about BPF 50 (7 KHz). This frequency matches with the frequency calculated using the characteristic wavelength of the vortical structures in the wake (shown in Fig. 4.10) and the wake convection velocity, equal to about 0.003 m and 20 m/s, respectively. A very similar hump at the same frequency range has been found from Wu et al. [36] from a numerical simulation on an airfoil at $Re_c = 1.5 \cdot 10^5$. The hump is clearly visible at all the advance ratios and it grows of about 10 dB when the J increases from 0 to 0.6. The more efficient noise emission as J increases is associated with an increase in length scale and coherence of the vortices when the laminar separation region become wider.

The steady pressure distribution across the rotor, associated with steady loading, is responsible for BPF 1 and 2 [15]. The amplitude of the BPF 1 decreases as the advance ratio increases. This is related with the reduction of thrust with the advance ratio (see Fig 4.8). At positive advance ratios, the tones at higher harmonics (BPF 5 - BPF 100) are associated to the motor electrical noise, as shown above. The appearance of tones in hover conditions, $J = 0$, can be associated with unsteady pressure fluctuations due to

blade vortex interaction, i.e. the impact of a blade with the tip vortex generated by the successive blade, as shown by Gourdain et al. [12]. When the advance ratio is increased, the wake is convected downstream and no interaction take place. It can be noted that, in hover condition, the tones show an increasing trend up to BPF 10. Nardari et al. [21] proved that additional tonal energy in the mid-frequency range is generated by unsteady blade loading due to flow recirculation in a confined environment, as in the anechoic chamber, and tones from BPF 2 to 30 for the confined condition are up to 10 dB higher with respect to the unconfined case. The BPF 1, due to steady loading, and the high-frequency part of the spectra are insensitive to flow recirculation.

4.5. CONCLUSION

A small-scale UAV propeller operating at a chord based Reynolds number of the order of 10^4 has been studied experimentally in terms of characteristics of the flow development over the blade and the far-field noise, via oil-flow visualizations, phase-locked PIV and microphones measurements. Insights about the boundary layer behaviour are retrieved through the analysis of mean and rms velocity, spanwise vorticity and static pressure calculated from the PIV velocity.

The main acoustic contamination during the experimental campaign turn out to be the motor noise that is responsible for a series of discrete tones at mid-high frequency range (BPF 5 - BPF 100). The maximum uncertainty of the main tone level is related to the instantaneous variation of the propeller rotational speed and it is shown to be about 2 dB.

The oil flow and PIV results reveal the presence of a laminar separation bubble (LSB) on the suction side of the blade for J = 0, 0.24 and 0.4. The LSB is found to move toward the leading edge and decreases in size when the angle of attack is increased, or rather, the advance ratio J decreased. As far as the authors' knowledge, it is the first time that a LSB has been visualized on such a small scale propeller. The case $J = 0$ is the only one where the LSB does not extend up to the very tip region. The hypothesis is that the blade vortex interaction washes out the LSB at the tip. The case $J = 0.6$ shows a long bubble without a clear evidence of reattachment. The more pronounced velocity fluctuations in the wake with respect to the other cases are mainly associated with a wake vortex shedding that is more efficient at $J = 0.6$, due to coherent structure with a bigger length scale. Noise spectra in hover condition exhibit stronger tonal contribution, as a result of unsteady loading, with respect to cases at positive advance ratios. The main broadband noise sources at low-mid frequency range associated with the different advance ratios conditions are different. For the case $J = 0$, turbulence ingestion noise at the leading edge is believed to be the dominant source. The turbulence impinging the leading edge is generated by the wake of the previous blade. At $J = 0.24$, 0.4 and 0.6 the trailing edge noise source is expected to become the dominant one. The small differences in the noise levels are associated with different trends of the boundary layer integral parameters at the trailing edge, in turn related with different positions of the laminar-to-turbulent transition and reattachment points. The high frequency hump, visible for all the cases, is caused by the wake vortex shedding, originated from the laminar separation region. The bigger dimension of the vortices at $J = 0.6$ make the noise emission at high frequency 10 dB more efficient with respect to the case $J = 0$.

BIBLIOGRAPHY

[1] William G Bastedo Jr and Thomas J Mueller. “Spanwise variation of laminar separation bubbles on wings at low Reynolds number”. In: *Journal of aircraft* 23.9 (1986), pp. 687–694.

[2] Michael Boutilier and Serhiy Yarusevych. “Parametric study of separation and transition characteristics over an airfoil at low Reynolds numbers”. In: *Experiments in Fluids* 52 (June 2012). DOI: 10.1007/s00348-012-1270-z.

[3] John Brandt and Michael Selig. “Propeller Performance Data at Low Reynolds Numbers”. In: (Jan. 2011). DOI: 10.2514/6.2011-1255.

[4] M. Brendel and T. Mueller. “Boundary-layer measurements on an airfoil at low Reynolds numbers”. In: *Journal of Aircraft* 25 (July 1988), pp. 612–617. DOI: 10.2514/3.45631.

[5] Sebastian Burgmann, Christoph Brücker, and Wolfgang Schröder. “Scanning PIV measurements of a laminar separation bubble”. In: *Experiments in Fluids* 41 (Aug. 2006), pp. 319–326. DOI: 10.1007/s00348-006-0153-6.

[6] Damiano Casalino, Edoardo Grande, Gianluca Romani, Daniele Ragni, and Francesco Avallone. “Definition of a benchmark for low Reynolds number propeller aeroacoustics”. In: *Aerospace Science and Technology* 113 (2021), p. 106707.

[7] M. Drela. *XFOIL: An Analysis and Design System for Low Reynolds Number Airfoils. In: Mueller T.J. (eds) Low Reynolds Number Aerodynamics. Lecture Notes in Engineering, vol 54*. Springer, Berlin, Heidelberg, 1989.

[8] Mark Drela. “XFOIL: An analysis and design system for low Reynolds number airfoils”. In: *Low Reynolds Number Aerodynamics: Proceedings of the Conference Notre Dame, Indiana, USA, 5–7 June 1989*. Springer. 1989, pp. 1–12.

[9] Mark Drela and Michael Giles. “Viscous-Inviscid Analysis of Transonic and Low Reynolds Number Airfoils”. In: *Aiaa Journal* 25 (Oct. 1987), pp. 1347–1355. DOI: 10.2514/3.9789.

[10] Mustafa Genç, Kemal Koca, Halil Açıkel, Gökhan Özkan, Mehmet Kırış, and Rahime Yıldız. “Flow characteristics over NACA4412 airfoil at low Reynolds number”. In: *EPJ Web of Conferences* 114 (Jan. 2016), p. 02029. DOI: 10.1051/epjconf/201611402029.

[11] Mustafa Serdar Genç, Gökhan Özkan, Mustafa Özden, Mehmet Sadik Ki˙ ri˙ ş, and Rahime Yi˙ ldi˙ z. “Interaction of tip vortex and laminar separation bubble over wings with different aspect ratios under low Reynolds numbers”. In: *Proceedings of*

the Institution of Mechanical Engineers, Part C: Journal of Mechanical Engineering Science 232.22 (2018), pp. 4019–4037.

[12] Nicolas Gourdain, Thierry Jardin, Ronan Serre, Sebastien Prothin, and Jean-Marc Moschetta. "Application of a lattice Boltzmann method to some challenges related to micro-air vehicles". In: *International Journal of Micro Air Vehicles* 10 (Sept. 2018), pp. 285–299. DOI: 10.1177/1756829318794174.

[13] Edoardo Grande, Gianluca Romani, Daniele Ragni, Francesco Avallone, and Damiano Casalino. "Aeroacoustic Investigation of a Propeller Operating at Low Reynolds Numbers". In: *AIAA Journal* (2021), pp. 1–12. DOI: 10.2514/1.J060611.

[14] R. Hain, Christian Kähler, and Rolf Radespiel. "Dynamics of laminar separation bubbles at low-Reynolds-number aerofoils". In: *Journal of Fluid Mechanics* 630 (July 2009), pp. 129–153. DOI: 10.1017/S0022112009006661.

[15] Daehan Kim, Chun Park, and Young Moon. "Aerodynamic Analyses on the Steady and Unsteady Loading-Noise Sources of Drone Propellers". In: *International Journal of Aeronautical and Space Sciences* (May 2019). DOI: 10.1007/s42405-019-00176-3.

[16] Dong-Ha Kim, Jae-hun Yang, Jo-Won Chang, and Joon Chung. "Boundary Layer and Near-Wake Measurements of NACA 0012 Airfoil at Low Reynolds Numbers". In: Jan. 2009. ISBN: 978-1-60086-973-0. DOI: 10.2514/6.2009-1472.

[17] Hsiao Mun Lee, Zhenbo Lu, Kian Meng Lim, Jinlong Xie, and Heow Pueh Lee. "Quieter propeller with serrated trailing edge". In: *Applied Acoustics* 146 (2019), pp. 227–236.

[18] J. Lin and L.L. Pauley. "Low-Reynolds-number separation on an airfoil". In: *Aiaa Journal* 34 (Aug. 1996), pp. 1570–1577. DOI: 10.2514/3.13273.

[19] Rens Macneill and Dries Verstraete. "Blade element momentum theory extended to model low Reynolds number propeller performance". In: *The Aeronautical Journal* 121 (May 2017), pp. 1–23. DOI: 10.1017/aer.2017.32.

[20] Roberto Merino-Martinez, Alejandro Rubio Carpio, Lourenco Lima Pereira, Steve Herk, Francesco Avallone, Daniele Ragni, and Marios Kotsonis. "Aeroacoustic design and characterization of the 3D-printed, open-jet, anechoic wind tunnel of Delft University of Technology". In: *Applied Acoustics* 170 (Dec. 2020), p. 107504. DOI: 10.1016/j.apacoust.2020.107504.

[21] Clément Nardari, Damiano Casalino, Francesco Polidoro, Vedran Coralic, Phoitack Lew, and John Brodie. "Numerical and Experimental Investigation of Flow Confinement Effects on UAV Rotor Noise". In: May 2019. DOI: 10.2514/6.2019-2497.

[22] Bas Oudheusden. "PIV-based pressure measurement". In: *Measurement Science and Technology* 24 (Jan. 2013), p. 032001. DOI: 10.1088/0957-0233/24/3/032001.

[23] Tiziano Pagliaroli, Jean-Marc Moschetta, Emmanuel Benard, and Cyril Nana. “3AF: Noise signature of a MAV rotor in hover”. In: Mar. 2014.

[24] Donghun Park, Hojoon Shim, and Yunggyo Lee. “PIV Measurement of Separation Bubble on an Airfoil at Low Reynolds Numbers”. In: June 2019. DOI: 10.2514/6.2019-3644.

[25] S Pröbsting, F Scarano, and SC Morris. “Regimes of tonal noise on an airfoil at moderate Reynolds number”. In: *Journal of Fluid Mechanics* 780 (2015), p. 407.

[26] Stefan Pröbsting and S. Yarusevych. “Laminar separation bubble development on an airfoil emitting tonal noise”. In: *Journal of Fluid Mechanics* 780 (Oct. 2015), pp. 167–191. DOI: 10.1017/jfm.2015.427.

[27] Daniele Ragni, Bas Oudheusden, and Fulvio Scarano. “Non-intrusive aerodynamic loads analysis of an aircraft propeller blade”. In: *Experiments in Fluids* 51 (Aug. 2011), pp. 361–371. DOI: 10.1007/s00348-011-1057-7.

[28] FFJ Schrijer and Fulvio Scarano. “Effect of predictor–corrector filtering on the stability and spatial resolution of iterative PIV interrogation”. In: *Experiments in fluids* 45.5 (2008), pp. 927–941.

[29] Ronan Serre, Nicolas Gourdain, Thierry Jardin, Adrián López, Viswesh Balaramraja, Sylvain Belliot, Marc Jacob, Jean-Marc Moschetta, and Hawaii Maui. “Aerodynamic and acoustic analysis of an optimized low Reynolds number rotor”. In: *ISROMAC*. Dec. 2017.

[30] Giorgia Sinibaldi and L. Marino. “Experimental analysis on the noise of propellers for small UAV”. In: *Applied Acoustics* 74 (Jan. 2013). DOI: 10.1016/j.apacoust.2012.06.011.

[31] S. Sunada, K. Ozaki, M. Tanaka, T. Yasuda, K. Yasuda, and Keiji Kawachi. “Airfoil characteristics at a low Reynolds number”. In: *Journal of Flow Visualization and Image Processing* 7 (Jan. 2000), p. 10. DOI: 10.1615/JFlowVisImageProc.v7.i3.20.

[32] Connor E Toppings, John W Kurelek, and Serhiy Yarusevych. “Laminar Separation Bubble Development on a Finite Wing”. In: *AIAA Journal* (2021), pp. 1–13.

[33] Jerry Westerweel. “Fundamentals of digital particle image velocimetry”. In: *Measurement science and technology* 8.12 (1997), p. 1379.

[34] Christian Willert. “Stereoscopic digital particle image velocimetry for application in wind tunnel flows”. In: *Measurement science and technology* 8.12 (1997), p. 1465.

[35] Justin Winslow, Hikaru Otsuka, Bharath Govindarajan, and Inderjit Chopra. “Basic Understanding of Airfoil Characteristics at Low Reynolds Numbers (104–105)”. In: *Journal of Aircraft* 55 (Dec. 2017), pp. 1–12. DOI: 10.2514/1.C034415.

[36] Hao Wu, Marléne Sanjosé, Stéphane Moreau, and Richard Sandberg. “Direct Numerical Simulation of the Self-Noise Radiated by the Installed Controlled-Diffusion

Airfoil at Transitional Reynolds Number". In: May 2018. DOI: 10.2514/6.2018-3797.

[37] Yannian Yang, Yong Wang, Yu Liu, Haitao Hu, and Zhiyong Li. "Noise reduction and aerodynamics of isolated multi-copter rotors with serrated trailing edges during forward flight". In: *Journal of Sound and Vibration* 489 (2020), p. 115688.

[38] Serhiy Yarusevych, Pierre Sullivan, and John Kawall. "Coherent structures in an airfoil boundary layer and wake at low Reynolds numbers". In: *Physics of Fluids* 18 (Apr. 2006), p. 044101. DOI: 10.1063/1.2187069.

5

ISOLATED PROPELLER: LAMINAR SEPARATION BUBBLE NOISE

This chapter explains the presence and relevance of noise caused by a laminar separation bubble (LSB) on a propeller operating at low-Reynolds number. Microphone measurements of a propeller with both clean and forced boundary layer transition blades are carried out in an anechoic wind tunnel by varying the propeller advance ratio J from 0 to 0.6, corresponding to a tip Reynolds number ranging from $4.3 \cdot 10^4$ *to* 10^5*. The flow behaviour on the blade surface and around the propeller is investigated with oil-flow visualizations and particle image velocimetry. At J = 0.4 and 0.6, vortex shedding from the LSB causes high-frequency noise which appears as a hump in the far-field noise spectra. Forcing the location of the boundary layer transition suppresses the LSB and, consequently, the hump, reducing the noise emission of about 5 and 10 dB at J = 0.4 and 0.6, respectively. The fact that the hump is caused by LSB vortex shedding noise is further assessed by using a semi-empirical noise model; it shows that the hump is constituted by tones of different amplitudes and frequencies, emitted at different spanwise sections along the blade.*

Parts of this chapter have been published in AIAA Journal 2022 [9].

5.1. INTRODUCTION

Chapter 4 oultined the various noise sources which are simultaneously present in a small-scale propeller operating at low-Reynolds numbers. In particular, it demonstrates that under certain operating conditions, the vortex shedding generated from a LSB constitutes the predominant noise source at high-frequency and it is responsible for a hump in the far-field noise spectra, as also noted by Leslie et al. [10]. Building on this foundation, the current chapter serves as a follow-up study, exploring in depth the characteristics of the LSB and the associated vortex shedding noise emission.

Studies on steady airfoils reveal that, as the angle of attack (or Reynolds number) increases, the LSB moves upstream and decreases in length [6]. The decrease in length of the LSB as the angle of attack increases continues until the separation and reattachment point occur at the same point (in the vicinity of the leading edge) and the bubble bursts. In this scenario, a laminar separation is still present but the separated shear layer is not able to reattach anymore. At very low Reynolds numbers, a LSB can burst at low angles of attack, resulting in a notable decrease in the lift curve slope due to a lower suction peak compared to the corresponding inviscid case [20, 11]. The general trend of the separation and reattachment points as function of the angle of attack across various Reynolds numbers, as well as the corresponding lift and drag coefficients are shown in Sect 2.2.1, specifically in Figs. 2.4 and 2.5, respectively.

A LSB located sufficiently close to the airfoil trailing edge is responsible of tonal noise emission [15]. Coherent vortices, result of amplified instability (Tollmien-Schlichting) waves into the laminar boundary layer, roll-up over the separated shear layer and produces tonal noise during their passage over the trailing edge. The coherence of the vortical structures at the trailing edge is a necessary condition for tonal noise emission. The acoustic pressure waves scattered at the trailing edge propagate upstream and trigger the generation of new instability waves in turn leading to vortex shedding, hence creating a feedback loop, discussed more in details in Sect. 2.3.1. It is not clear yet whether the presence of a feedback loop is a necessary condition for the tonal noise generation and there is no agreement on the physics and exact chordwise extent of the feedback loop [4]. In presence of vortex shedding from LSB, the spectrum of the radiated noise consists of a broadband hump, centered at a frequency f_s, and a dominant (or central) tone, at a frequency $f_{n_{MAX}}$, surrounded by a series of regularly spaced tones at frequencies f_n [3]. Paterson et al. [13] observed that, for a small range of free-stream velocities U_∞, the main tone frequency exhibits a power relationship of $U_\infty^{0.8}$. Moreover, at specific velocities, the frequency shifts to higher values while maintaining the same power relationship, resulting in what is referred to as a "ladder-structure." The overall trend of the main tone frequency follows a 3/2 power of the free-stream velocity, thus $f_{n_{MAX}} \propto U_\infty^{1.5}$. While Paterson's model estimates only the vortex shedding tone frequency, the only available model that predicts the amplitude of the tones is the airfoil self noise model from Brooks et al. [7] (in the following referred as BPM model). The latter is a semi-empirical model based on a wind tunnel data set on NACA 0012 airfoils of different chord length. It is unknown if the current knowledge about noise generation due to laminar vortex shedding from steady airfoils applies also to rotating blades. In this case, the spanwise variation of velocity and angle of attack can influence the formation of the LSB and the coherence of the shed vortices.

The small-scale propeller of Chapter 4 is tested at a tip Reynolds number between $4.3 \cdot 10^4$ and 10^5. Far-field noise measurements, phase-locked stereoscopic PIV and oil-flow visualization are used to quantify the noise radiation and to visualize the flow around the propeller and on the blade surface, respectively. A comparison is presented for the case of the propeller with smooth surface and with a turbulator applied on the blade surface to force the location of the transition of the boundary layer from laminar to turbulent. A physical interpretation of the acoustic spectra is given by extending the BPM model to rotating blades.

This chapter is structured as follows. In Sect. 5.2 the propeller geometry is presented together with the experimental setup. Section 5.3 illustrates the extension of the BPM model to rotating blades. Section 5.4 shows the oil-flow and PIV results, while the experimental and numerical noise spectra are illustrated in Sect. 5.5. Finally, the main conclusions of the work are summarized in Sect. 5.6.

5.2. PROPELLER GEOMETRY AND EXPERIMENTAL SETUP

The propeller utilized in this study is the same as the one used in Chapter 4, where a detailed description is provided. Measurements are conducted both with a smooth blades surface (denoted as clean) and with a turbulator applied on the suction side of the propeller blade (denoted as forced-BL s.s), on the pressure side (denoted as forced-BL p.s) and on both pressure and suction side (denoted as forced-BL). The turbulator fixes the boundary layer transition location and it is realized as a flat strip with a thickness of 0.08 mm and a chordwise length of 1 mm and it is applied at 25% of the chord. As for the previous study, the propeller is tested in the open-jet anechoic tunnel (A-tunnel) of TU Delft [12]. The exit nozzle employed is circular, with an exit diameter of 0.60 m and a contraction ratio of 15:1.

For the acoustic measurements, the propeller is operated at three rotational velocities, 4000, 5000 and 6000 rpm, over a range of advance ratios $J = V_\infty / nD$ between 0 and 0.6 (where V_∞ is the axial flow speed in m/s, n is the propeller rotational frequency in Hz and D is the propeller diameter in m). The tip Reynolds number is varied from $4.3 \cdot 10^4$ to 10^5. The operating conditions are summarized in Table 5.1. The flow measurements are conducted over a reduced test-matrix, i.e. 4000 rpm and all the J reported in Table 5.1.

Table 5.1: Propeller operating conditions.

J	**V_∞ [m/s]**		
	$\omega = 4000$ rpm	$\omega = 5000$ rpm	$\omega = 6000$ rpm
0.00	0.0	0.0	0.0
0.24	4.8	6.0	7.2
0.40	8.0	10	12
0.60	12	15	18

5.2.1. ACOUSTIC MEASUREMENTS

The acoustic measurements are performed by means of an arc of microphones, constituted by 7 G.R.A.S. 46BE 1/4" free-field microphones, having a frequency range between 4 Hz and 80 KHz and a maximum SPL of 160 dB. As shown in Fig. 5.1, the microphone arc has a radius of 4D (1.2 m) and the angle between each microphone is 10°). The microphones are calibrated using a G.R.A.S. 42AA pistonphone with a calibration level of 114 dB re. 20 μPa. The uncertainty of the calibration is less than 0.09 dB (99% confidence level). The data acquisition system consists of a National Instrument PXIe-4499 sound and vibrations data acquisition module. Microphone voltages have been recorded for a duration of 30 s at a frequency rate of 100 KHz. Fourier transformed data are obtained with 750 Welch blocks, 50% overlap and Hanning windowing, corresponding to a bandwidth of 25 Hz.

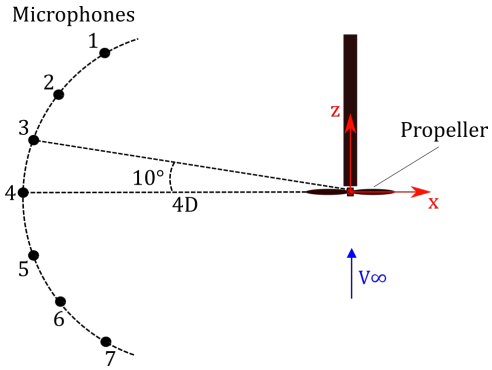

Figure 5.1: Microphone array configuration.

5.2.2. PIV MEASUREMENTS

Stereoscopic PIV measurements are conducted to study the flow around the cross-section of the blade at $r/R = 0.6$ and in the propeller wake. The camera configuration and acquisition parameters are outlined in Sect. 3.4, and illustrations of the two PIV setups used for the cross-section and wake measurements are presented in Figs. 3.4 and 3.5.

A self-calibration through a disparity correction procedure is used [19] to refine the target calibration by correlation of the particle images between the two cameras. The residual average misalignment is equal to 0.005 px. The phase-locked PIV measurements of this study are mainly affected by random errors, as the cross-correlation uncertainty, which is in a range of 0.05-0.1 px [18], for a multi-pass algorithm ending with a windows size of 16 x 16 px. Following the calculation procedure described in Sect. 4.3, the overall uncertainty on the maximum and minimum mean velocities are assessed at 0.04% and 0.22%. On the other hand, the overall uncertainty relative to the maximum and minimum velocity fluctuations are of the order of 1.7% and 14%, respectively.

5.3. EXTENSION OF THE BPM MODEL TO ROTATING BLADES

This section illustrates how the BPM model [7], originally developed to predict self generated noise of a steady airfoil encountering smooth flow is extended to a rotating blade. To this purpose, a strip approach is applied, i.e. the propeller blade is divided in N spanwise elements (sources) and, for each of them, the noise contribution is computed by using the BPM model. The main assumption of the strip theory is that there is no aerodynamic interaction between the elements, thus the effect of the spanwise velocity component is discarded. The airfoil self-noise mechanisms implemented in the current work are the laminar boundary layer vortex shedding (LBL-VS) noise and turbulent boundary layer trailing edge noise (TBL-TE). Following the BPM approach, the LBL-VS noise spectrum in 1/3-octave for the i-th strip can be written as:

$$SPL^{i}_{LBL-VS}(X,Y,Z) = 10\log\left(\frac{L_i \delta_p M^5 \overline{D_h}}{r_e^2}\right) + G_1\left(\frac{St'}{St'_{peak}}\right) + G_2\left[\frac{Re_c}{(Re_c)_0}\right] + G_3(\alpha) \quad (5.1)$$

where the superscript i refers to the i-th strip, L_i is the spanwise length of the strip, δ_p is the boundary layer thickness at the trailing edge of the blade for the pressure side, M is the free-stream Mach number, r_e is the absolute distance source-observer, $\overline{D_h}$ is the directivity function for the high-frequency limit, St' is a Strohual number defined as $St' = f\delta_p/U_\infty$ with f being the frequency vector and U_∞ the free-stream velocity, Re_c is the chord-based Reynolds numbers, α is the angle of attack. For details about $\overline{D_h}$, St'_{peak}, $(Re_c)_0$, G_1, G_2, G_3, the reader can refer to Brooks at al. [7]. The TBL-TE noise spectrum in 1/3-octave for the i-th strip is instead modelled as follows:

$$SPL^{i}_{TBL-TE}(X,Y,Z) = 10\log\left(10^{(SPL_p/10)} + 10^{(SPL_s/10)} + 10^{(SPL_\alpha/10)}\right) \quad (5.2)$$

where the three terms in the equation account for the attached TBL at the pressure side (SPL_p), for the attached TBL at the suction side (SPL_s) and for the separated boundary layer at high angles of attack (SPL_α). The full expressions for these three terms can be found in Brooks at al. [7].

The quantities δ_p and α constitute the main input parameters of the LSB-VS noise model, while δ^*_p, δ^*_s (boundary layer displacement thickness at the pressure and suction side) and α constitute the main input parameters for the TBL-TE noise model. These parameters are predicted by using *Optyδ̂B*-BEMT , which is a tool for the prediction of the propeller loads, based on blade element momentum theory formulation with uniform inflow. Details about the tool can be found in the work of Casalino et al. [8], where the tool has been validated against experimental and numerical results.

When calculating the SPL contribution of the i-th strip from Eq. 5.1, a local reference frame (x,y,z) shown in Fig. 5.2 (right) and located at the midspan of the strip, is used. The axis x,y,z are the the chordwise, spanwise and wall-normal components, respectively. On the other hand, the position of the observer is given in the rotor fixed reference system (X,Y,Z), shown in Fig. 5.2 (left), where the X and Y axes are in the rotor plane and the Z axis is parallel to the free-stream. Therefore, a coordinate transformation is applied to express the position of the observer, given in (X,Y,Z), with respect to (x,y,z). In order to account for the Doppler effect, a frequency shift [2] is applied to each strip as:

$$\frac{\omega_e}{\omega_o} = 1 + M_b \sin\Psi \sin\Theta \tag{5.3}$$

In the latter ω_e is the emitted frequency from the source, ω_o is the frequency at the observer location, M_b is the source Mach number, Ψ is the source azimuthal position and Θ is the observer angle (see Fig. 5.2). Finally, the total noise contribution is computed by assuming fully uncorrelated sources and averaging over all the azimuthal positions of the blade by means of:

$$SPL(x,y,z) = \frac{B}{2\pi}\int_0^{2\pi}\left(\frac{\omega_e}{\omega_o}\right) SPL^i(x,y,z)\, d\Psi \tag{5.4}$$

where B is the number of blades.

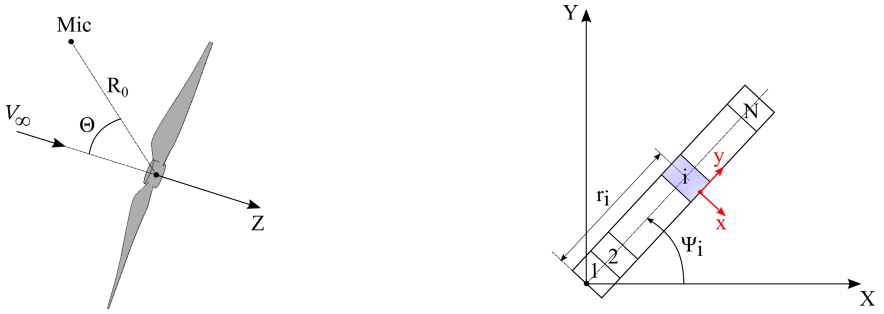

Figure 5.2: Representation of the rotor fixed reference frame (left) and the propeller strip reference frame (right).

The vortex shedding noise frequency for each blade strip is also estimated by means of Paterson's power law relationship (mentioned in Sec. 5.1). He postulated that the vortex shedding phenomenon from an airfoil qualitatively resembles the shedding associated to bluff bodies. Therefore a Strouhal number St of 0.2, defined as $St = 2f\delta_{TE}/U_\infty$ with δ_{TE} being the airfoil boundary layer thickness at the trailing edge, has been taken as non-dimensional frequency scaling law. Using for δ_{TE} the Blasius solution for a flat plate [1], it follows:

$$f = K\frac{U_\infty^{1.5}}{\sqrt{cv}} \tag{5.5}$$

where $K = 0.02$, c is the airfoil chord and v is the kinematic viscosity of the fluid.

5.4. AERODYNAMIC CHARACTERIZATION

5.4.1. OIL-FLOW VISUALIZATIONS

Figure 5.3 shows the oil-flow visualizations of the suction side of the propeller blade for both the clean and forced-BL cases at 4000 rpm and J varying from 0 to 0.6. Since the oil, especially at the tip region, is subjected to the propeller centrifugal force, the oil-flow

results are only used to show the presence of a LSB, and not to retrieve the streamlines direction. The blade portions where the thickness oil accumulates (green area marked with S) represents regions with flow separation. These regions are characterized by a chordwise pressure gradient that is almost zero and the flow is predominantly radial due to the centrifugal force.

The clean case (Fig. 5.3 up) reveals a presence of a LSB at J between 0 and 0.4. The LSB is represented by the green region enclosed between the separation and reattachment lines, highlighted with dashed magenta and red lines, respectively. The LSB length increases with J because of a decrease of the local angle of attack along the blade. Unlike the other cases, at $J = 0$ the LSB does not extend up to the tip and this is ascribed to the tip vortex, that washes out the LSB at the tip region [17, 5]. For the case $J = 0.6$, the flow separates but it is not very clear if it reattaches in proximity of the trailing edge. Thus, a bubble bursting might occur.

When the turbulator is used, Fig. 5.3 (down), the LSB is suppressed and all the cases exhibit a similar behaviour. After the turbulator line the flow is attached and eventually separates close to the trailing edge. The separated region extends up to the tip only at $J = 0$ and reduces in size as the advance ratio increases. This is probably due to the global decrease of the angle of attack over the entire blade as J increases.

5.4.2. VORTICITY FIELD AROUND THE CROSS-SECTION AT $r/R = 0.6$

Figure 5.4 shows the instantaneous spanwise vorticity distribution (obtained with finite difference of order two from the PIV velocity fields) around the cross-section of the clean blade at $r/R = 0.6$ at 4000 rpm and J varying from 0 to 0.6. The x and y axis are normalized with respect to the local airfoil chord and centered at the airfoil leading edge. Each vorticity field is adjacent to the corresponding oil-flow visualization of the blade suction side. The cross-section at $r/R = 0.6$ is marked with the horizontal magenta line.

The cases at $J = 0.4$ and 0.6 exhibit clear coherent structures in the near wake region ($1 < x/R < 1.2$), forming a vortex shedding. For the other two cases, i.e. $J = 0$ and 0.24, coherent structures in the near wake cannot be identified. Indeed, at low advance ratios the LSB has a smaller length and it is closer to the leading edge, as shown from the the oil-flow patterns in the left side of the figure. As a consequence, the vortex shedding is characterized by structures with a lower coherence and length scale, which might be not captured from the current PIV setup. The surface point on the suction side where the vorticity is non-zero (marked with O) moves toward the trailing edge as J increases, in agreement with the downstream displacement of the LSB. It is relevant to note that the length scale of the structures at $J = 0.6$ is larger compared with the case at $J = 0.4$. This is related to the laminar separation without reattachment, as mentioned in the previous section. In fact, as shown by Yarusevich [21], when the flow fails to reattach the scale of the wake structures is noticeably larger.

ESTIMATION OF THE SHEDDING FREQUENCY

The instantaneous vorticity fields at $J = 0.4$ and 0.6 are used to estimate the wake shedding frequency, adopting a statistical approach. To this purpose, the vorticity is extracted in the wake region and the two-dimensional spatial autocorrelation of the vorticity field is computed. Hence, for each frame, the characteristic wavelength λ of the vortices is

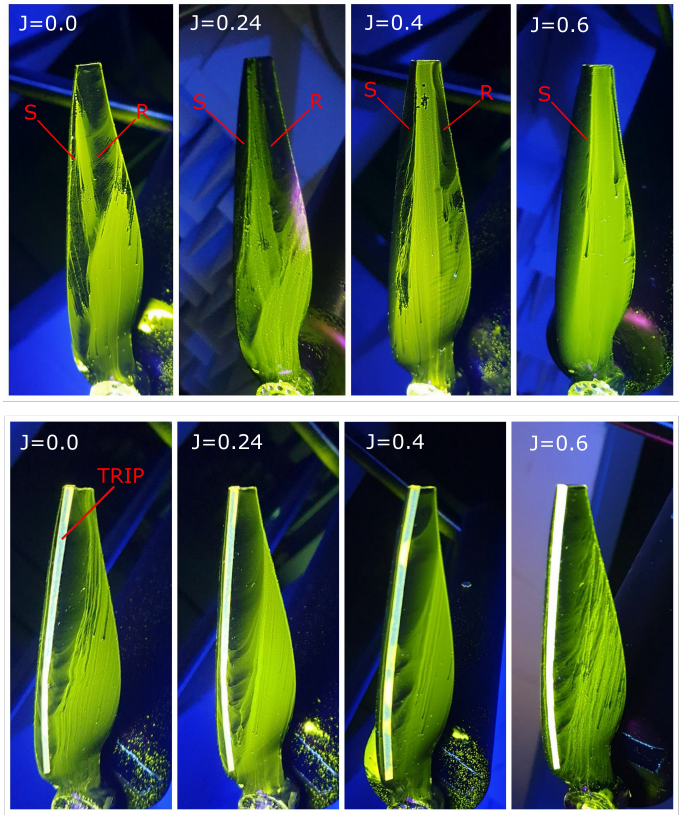

Figure 5.3: Oil flow visualizations of the suction side of the clean blade (up) and of the forced-BL blade (down) at 4000 rpm and **J** = 0, 0.24, 0.4 and 0.6.

calculated from the position of the autocorrelation peak and stored in an array. Lastly, the shedding frequency f_s is retrieved as $f_s = V_{conv}/\lambda$, where V_{conv} is the convection velocity, computed from the PIV velocity field. Figures 5.5a and 5.5b show the 2D autocorrelation coefficient $R_{xx}(\lambda)$ of a single vorticity field for the cases $J = 0.6$ and 0.4, respectively. As expected, they exhibit a unitary peak at $\lambda_x = \lambda_y = 0$ and a second peak with an amplitude of about 0.45 that is associated to the wavelength of the vortices. Spurious peaks with an amplitude lower than 0.2 are discarded. The arrays with the calculated wavelengths λ for each frame are fitted with Gaussian distributions (see Figs. 5.5c and 5.5d). The final wavelengths are chosen as the mean value of each distribution and they are equal to $\lambda = 2$ mm at $J = 0.4$ and $\lambda = 2.3$ mm at $J = 0.6$. The corresponding vortex shedding frequencies are 9635 Hz and 8600 Hz for $J = 0.4$ and 0.6, respectively.

5.4.3. VORTICITY FIELD IN THE PROPELLER SLIPSTREAM

In order to extend the above discussion to the entire blade, the y-component of the vorticity has been calculated in a plane in the propeller slipstream region for two cases: J

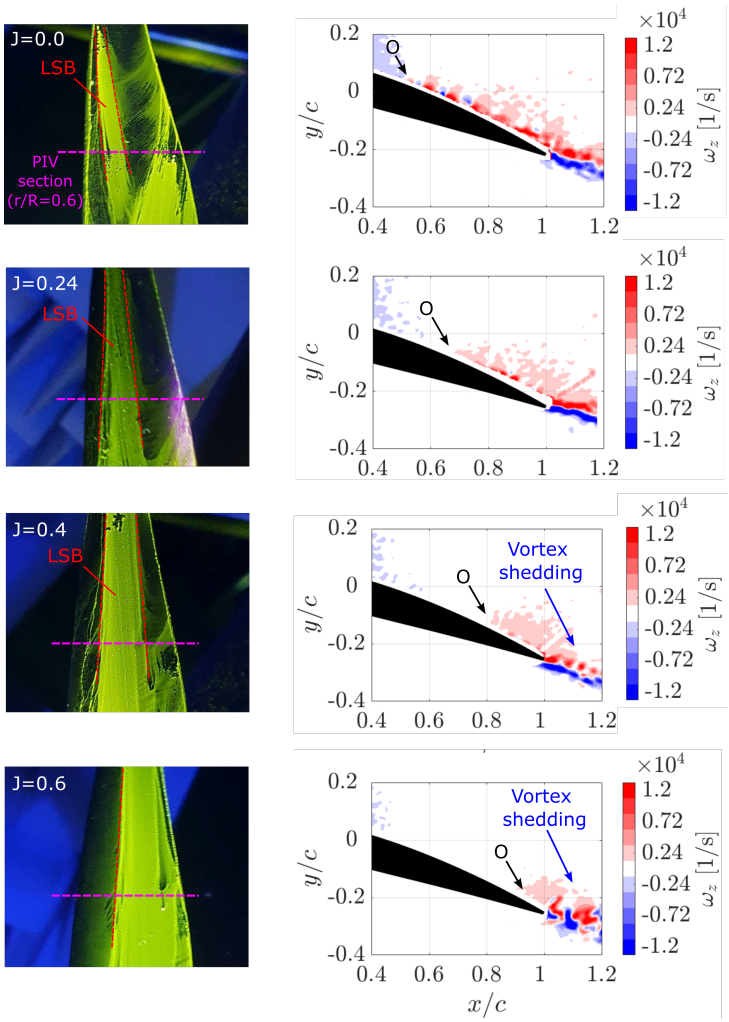

Figure 5.4: Instantaneous spanwise vorticity distribution (right) around the clean blade cross-section at **r**/**R** = 0.6 and oil-flow visualizations of the blade suction side at 4000 rpm. From top to bottom: **J** = 0, **J** = 0.24, **J** = 0.4 and **J** = 0.6.

= 0 (Fig. 5.6a) and $J = 0.4$ (Fig. 5.6b). The three columns in the figure represent three different propeller azimuthal angles: $\Psi = 0°$ (left), $\Psi = 45°$ (center), $\Psi = 90°$ (right). The flow direction is from bottom to top and the x and y axis are normalized with respect to the propeller radius. At $J = 0.4$ (Fig. 5.6b), the propeller presents a well-defined tip vortex together with a positive/negative vorticity region distributed along the entire blade, where different vortex cores are identified. This can be related to the footprint of the structures shed from the LSB, identified in Fig. 5.4, which are convected into the wake. These structures appear to be coherent after half rotor radius downstream of the propeller. The case $J = 0$ (Fig. 5.6a) exhibits a clear difference with respect to $J = 0.4$ and

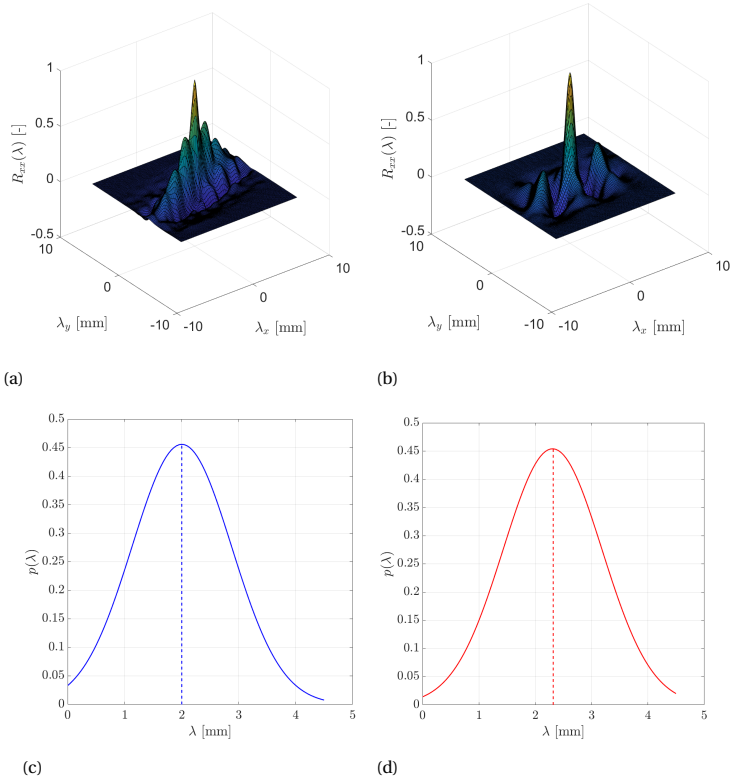

Figure 5.5: First row: two dimentional spatial autocorrelation coefficient of the instantaneous vorticity field in the cross-section wake at **J** = 0.4 (a) and **J** = 0.6 (b). Second row: probability density function distribution of the wavelength of the vortices shed from the LSB at **J** = 0.4 (c) and **J** = 0.6 (d).

a less coherent wake. A spanwise positive/negative vorticity region is barely noticeable, without a visible distribution of vortical structures. Furthermore, this region, together with the tip vortex, appears to dissipate faster and mix with the surrounding flow from about 0.2 rotor radius.

5.5. AEROACOUSTIC CHARACTERIZATION

5.5.1. EXPERIMENTAL FAR-FIELD NOISE SPECTRA

Figure 5.7 shows the experimental far-field noise spectra (above $2 \cdot 10^3$ Hz) for the clean blade, computed by using the pressure signals from microphone 2. Spectra from the other microphones show similar trends and do not provide additional information. Figure 5.7 (left) represents a comparison at a fixed rpm of 4000, by varying the J, Fig. 5.7 (right) represents instead a comparison at a fixed J of 0.6, by varying the rpm. In order to highlight the noise trends, a smoothing function that discard the tonal peaks due to the electric motor (as shown by Casalino et al. [8]), is applied to each spectrum and plotted

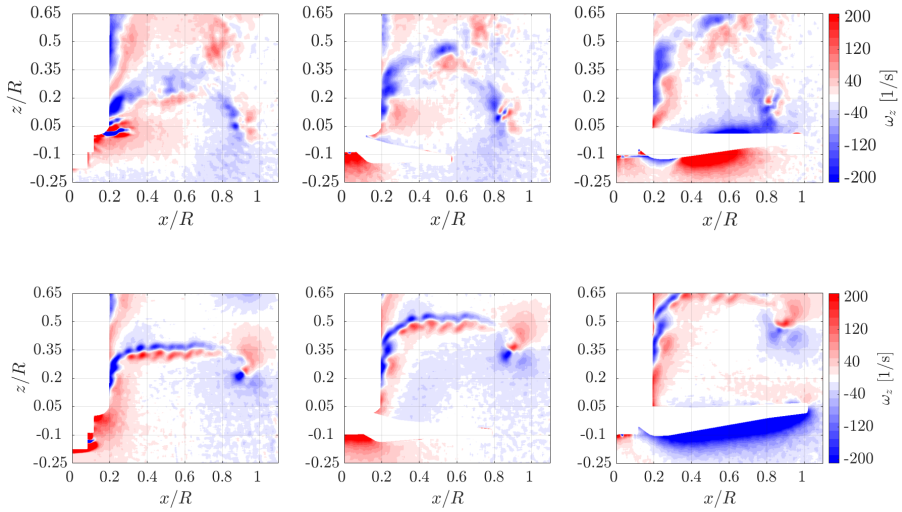

(a)

(b)

Figure 5.6: Instantaneous vorticity distribution in the wake at 4000 rpm and **J** = 0 (a) and **J** = 0.4 (b). The three columns represent three different propeller phases: $\phi = \mathbf{0}°$, $\phi = \mathbf{45}°$, $\phi = \mathbf{90}°$ (from left to right)

on top of the real spectrum. The hump above $5 \cdot 10^3$ Hz, visible at $J = 0.6$, and to a lesser extent, at $J = 0.4$, is due to the vortex shedding from the laminar separation bubble. A further indication is given by the Paterson' model (Eq. 5.5), which predicts vortex shedding frequencies in the same frequency range. Indeed, since the chord and velocity vary along the blade, there is a range of frequencies (instead of a single tone) at which the vortex shedding noise is expected to be present. For each operating condition, the minimum and maximum vortex shedding frequencies from the last 60% of the blade, predicted by Paterson's law, are reported in Table 5.2 and contained between $5 \cdot 10^3$ Hz and $4.7 \cdot 10^4$ Hz. The minimum frequencies are also represented in Fig. 5.7 as vertical lines. For the cross-section at the 60% of the span, the Paterson's frequencies $f_{s_{Pat}}$ predictions are compared with the experimental shedding frequencies $f_{s_{exp}}$ calculated in Sec. 5.4.2. At $J = 0.4$, $f_{s_{Pat}}$ is equal to 7200 Hz and $f_{s_{exp}}$ to 9635 Hz with a difference of about 2400 Hz. At $J = 0.6$, $f_{s_{pat}}$ is 7635 Hz and $f_{s_{exp}}$ = 8600 Hz. These discrepancies are attributed to the simplicity of Paterson's model which does not take into account the effect of the airfoil profile and to the intrinsic degree of uncertainty of the statistical approach used for the estimation of the shedding frequency.

It is evident that the amplitude of the hump increases when J passes from 0.4 to 0.6. This is associated to the increase in length of the shed vortices (see Sec. 5.4.2) and, as a consequence, to a more efficient noise source. For the cases $J = 0$ and 0.24, the lower coherence of the vortices at the trailing edge is the reason for the hump reduction. When the rpm is increased and J is kept equal to 0.6 (Fig. 5.7 right), the hump shifts toward higher frequencies and increases in amplitude. The frequency shifting is in agreement with the Paterson's model as it is dependent on the velocity ($f \propto U^{1.5}$). The increase in amplitude is due to the fact that, when the rpm increases (at a fixed J), the angle of attack

over the blade decreases and, as explained above, this shifts the separated area over the trailing edge and make the vortex shedding noise more efficient.

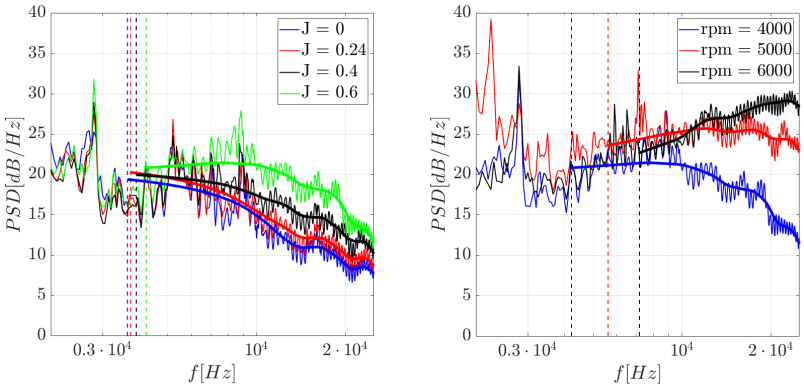

Figure 5.7: Comparison of noise spectra at mic 2 for the clean blade at a fixed rpm of 4000, by varying **J** (left) and a fixed J of 0.6, by varying the rpm (right).

Figures 5.8 shows the noise spectra for the forced-BL blade. As for the clean case, the left side of each figure reports a comparison at a fixed rpm of 4000, by varying the J, instead the right side represents a comparison at a fixed J of 0.6, by varying the rpm. The turbulator suppresses the formation of the laminar separation bubble responsible for the hump. The main noise source for this case is expected to be turbulent boundary layer trailing edge noise. It is interesting to note that, when the rpm is kept constant and J increases, the hump at $J = 0.4$ and 0.6 disappears and the spectra shows the same trend of the cases $J = 0$ and 0.24. This constitutes a further prove that the high frequency noise trend for the clean blade is strongly related to the LSB characteristics. On the other side, the increase of rpm at a fixed J of 0.6 causes an increase in the noise level. This could be related to the scaling of trailing edge noise with the Mach number.

Finally, in Figs. 5.9 and 5.10 are plotted the results for the forced-BL s.s. and forced-BL p.s. cases, respectively. They confirm that the high-frequency hump is due to a LSB

Table 5.2: Propeller vortex shedding frequencies predicted using Paterson's model.

J	**4000 rpm**		**5000 rpm**		**6000 rpm**	
	$f_{S,\min}$ [kHz]	$f_{S,\max}$ [kHz]	$f_{S,\min}$ [kHz]	$f_{S,\max}$ [kHz]	$f_{S,\min}$ [kHz]	$f_{S,\max}$ [kHz]
0.00	5.0	25.7	7.0	35.9	9.3	47.2
0.24	5.1	25.8	7.1	36.0	9.3	47.3
0.40	5.3	26.0	7.3	36.2	9.5	47.5
0.60	5.6	26.4	7.5	36.5	9.7	47.8

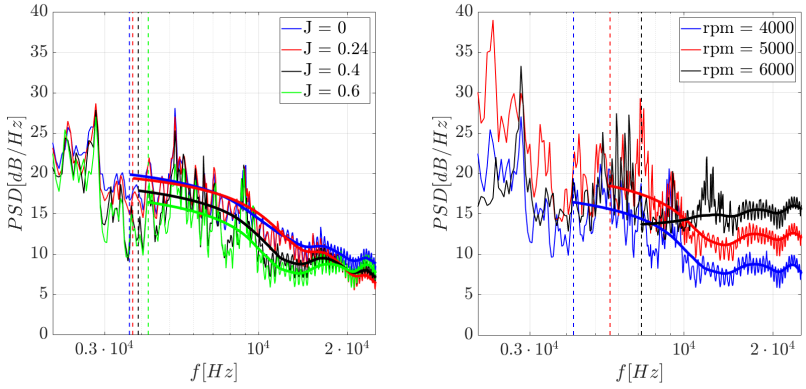

Figure 5.8: Comparison of noise spectra at mic 2 for the forced-BL blade at a fixed rpm of 4000, by varying **J** (left) and a fixed J of 0.6, by varying the rpm (right).

on the suction side of the blade. Indeed, when the turbulator is applied only on the suction side (Fig. 5.9), the spectra are very similar to the forced-BL case (Fig. 5.8). When the turbulator is applied only on the pressure side instead (Fig. 5.10), the hump is still visible and the spectra are similar to the clean case (Fig. 5.7.)

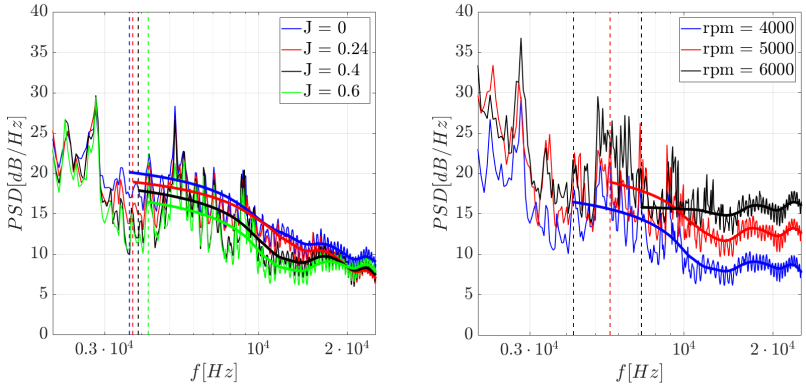

Figure 5.9: Comparison of noise spectra at mic 2 for the forced-BL s.s. blade at a fixed rpm of 4000, by varying **J** (left) and a fixed J of 0.6, by varying the rpm (right).

By comparing the noise spectra between the clean, forced-BL, forced-BL s.s. and forced-BL p.s. cases in Fig. 5.11, the final conclusions about the LSB effect can be more easily inferred. At the lowest advance ratios, i.e. $J = 0$ (Fig. 5.11a) and 0.24 (Fig. 5.11b),

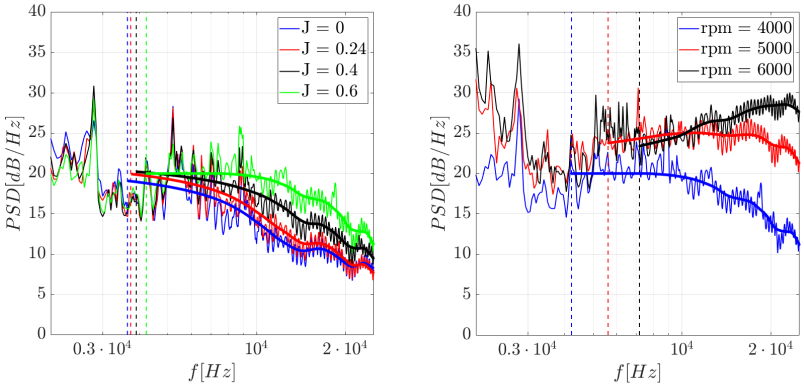

Figure 5.10: Comparison of noise spectra at mic 2 for the forced-BL p.s. blade at a fixed rpm of 4000, by varying **J** (left) and a fixed J of 0.6, by varying the rpm (right).

the LSB, located close to the blade leading edge, has almost no effect and all the spectra have similar levels. At $J = 0.4$ (Fig. 5.11c) and 0.6 (Fig. 5.11d) the vortex shedding from the LSB, which moves toward the blade trailing edge and increases in chordwise length, is the cause of an increment in noise level for the clean case with respect to the forced-BL and forced-BL s.s. cases of about 5 and 10 dB, respectively. When the turbulator is applied only at the pressure side, as expected, the noise spectra compare well to the clean case. In particular, the level of the forced-BL p.s. spectrum is about 1 dB (above $1.5 \cdot 10^4$ Hz) and 1.5 dB lower with respect to the clean case at $J = 0.4$ and 0.6, respectively. The slightly lower noise level compared to the clean configuration could be related to a coupling between the events on the two sides of the blade [14]. In other words, the turbulator on the pressure side could influence the position and length of the LSB on the suction side.

5.5.2. NOISE PREDICTION FROM THE SEMI-EMPIRICAL MODEL

This section presents a discussion about the low-order prediction by means of Eqs. 5.1 and 5.2. Figure 5.12 compares the predictions for the cases $J = 0.4$ and 0.6, which are the ones where the noise due to the shedding from the LSB constitutes the main source, against the experimental noise spectra. The first row illustrates the results at $J = 0.6$ and the second row at $J = 0.4$, while the three columns represents the three different rpm, i.e. 4000, 5000 and 6000 (from left to right). At $J = 0.6$, the LSB-VS model predicts sufficiently well the shape and frequency range of the high frequency hump. The overall mismatch in the amplitude of about 10 dB for all the cases is ascribed to the extreme sensitivity of the BPM model to the angle of attack and not to the present extension for the rotating blade case (see Appendix A). If α along the entire blade is varied of about 1 deg for the three cases, the predictions (labeled as "LSB-VS corr.") match the levels of the experimental spectra. It must be noted that the experimental distribution of angles of

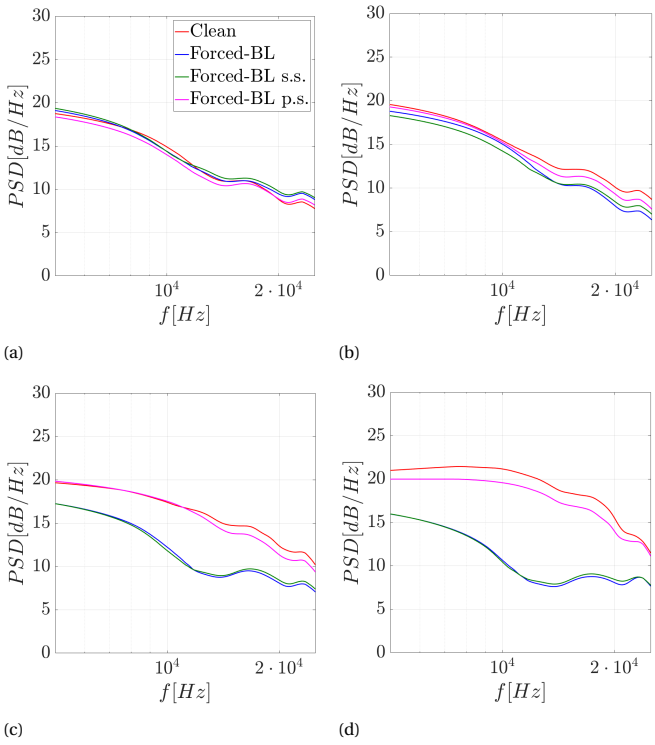

Figure 5.11: Comparison at mic 2 between clean, forced-BL, forced-BL s.s, forced-BL p.s noise spectra at 4000 rpm and **J = 0** (a), **J = 0.24** (b), **J = 0.4** (c), **J = 0.6** (d).

attack along the the blade is not available. Thus, the input angle of attack from *Opty∂B*-BEMT tool is affected by an uncertainty that is not quantifiable. Only for the case at 5000 rpm, the distribution of α from a high-fidelity simulation, performed by means of Simulia PowerFLOW software based on a Lattice-Boltzmann/Very Large Eddy method is also available (see the work from Romani et al. [16] for the details). The result using this α distribution is included in Fig 5.12b (denoted as LBL-VS PF) and it compares well with the "corrected" result using α from *Opty∂B*-BEMT . At $J = 0.4$, the amplitude of the numerical predictions from the LSB-VS model compare well to the experiments after the angle of attack "correction". On the other hand, the predicted frequency range is narrower with respect to the experimental values, which exhibit a broaden hump. At both the advance ratios, the TBL-TE model provides significantly lower levels, hence excluding trailing edge noise as one of the major noise sources. Furthermore, in this case a "correction" of the input α would not improve the match with the experimental values since the TBL-TE model is much less sensitive to a variation of α, as shown in the Appendix.

Figure 5.13a represents the noise spectrum in 1/3-octave (thick black line) at microphone 1 for the case at $J = 0.6$ and 4000 rpm, together with the contribution from each

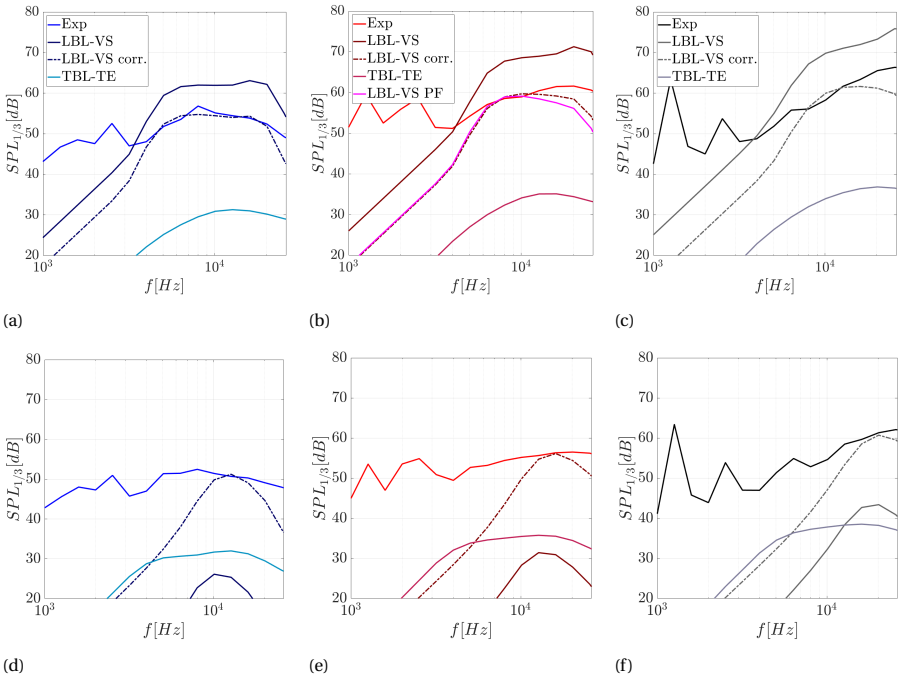

Figure 5.12: Comparison at mic 2 between the experimental noise spectra and the numerical predictions at **J = 0.6** and 4000 rpm (a), **J = 0.6** and 5000 rpm (b), **J = 0.6** and 6000 rpm (c), **J = 0.4** and 4000 rpm (d), **J = 0.4** and 5000 rpm (e), **J = 0.4** and 6000 rpm (f).

individual blade strip, where the blue lines represents the contribution of the sections up to $r/R = 0.7$ and the red lines from $r/R = 0.7$ onward. It is conjectured that the broad hump is due to the superimposition of tones of different amplitudes and frequencies, emitted from the single blade sections. Furthermore, the last 30% of the blade (red lines) has the largest contribution in terms of noise generation and it is responsible for most of the hump. Due to the lower relative velocity and higher angle of attack, the more inboard sections (blue lines) generate tones of much lower amplitude. This can be better visualized by plotting the azimuthal OASPL contribution in the propeller plane, as in Fig. 5.13b. The right outboard part of the disc shows an higher noise level (between 2 and 4 dB) with respect to the corresponding parts on the other sides and makes the plot asymmetric. This is due to the Doppler effect. The other cases present similar results, hence they are not reported.

5.6. CONCLUSIONS

An investigation of the noise emitted by a laminar separation bubble on a small-scale propeller operating at low-Reynolds number was accomplished through experimental measurements in an anechoic wind tunnel. The propeller was tested both with a smooth surface (clean) and with a turbulator applied on the suction side of the propeller blades

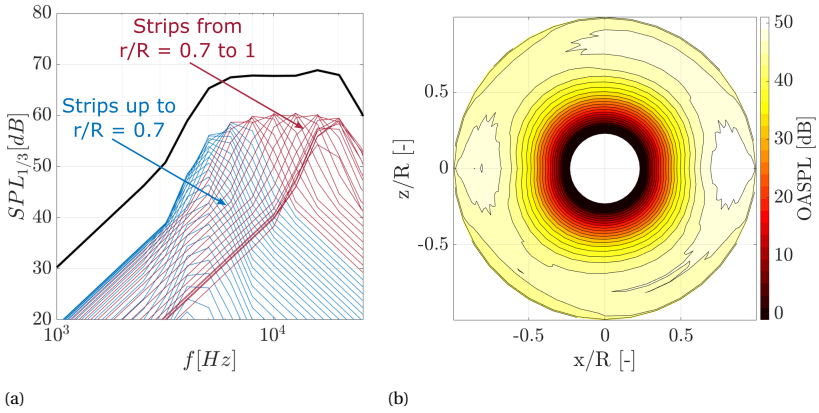

Figure 5.13: Sectional contribution to the numerical noise spectrum (a) and azimuthal OASPL contribution (b) at mic 2 for **J = 0.6** and 4000 rpm.

(forced-BL s.s.), on the pressure side (forced-BL p.s.) and on both suction and pressure side (forced-BL) to force the transition of the boundary layer from laminar to turbulent. Microphone measurements were complemented with oil-flow visualization of the blade surface and phase-locked PIV measurements of a blade cross-section and of the propeller slipstream. Physical insights of noise generation due to the LSB were retrieved by extending the semi-empirical BPM model [7] to rotating blades.

A laminar separation bubble was visualized on the suction side of the clean blade surface at $J = 0$, 0.24 and 0.4. At $J = 0.6$ the LSB probably bursts since there was not a visual evidence of flow reattachment. When the boundary layer transition location is forced, the LSB was suppressed and the flow appeared to be attached after the transition strip. The analysis of the instantaneous vorticity field around the cross-section at 60% of the span revealed that the LSB is responsible for vortex shedding, characterized by coherent structures in the wake for the cases $J = 0.4$ and 0.6. The bigger length scale of the shed vortices at $J = 0.6$ was associated with the hypothesis of separation without reattachment. The shedding frequency, calculated by means of a statistical approach, was found to be 9635 Hz and 8600 Hz at $J = 0.4$ and 0.6, respectively. Vortical coherent structures were not clearly visible for the cases $J = 0$ and 0.24 and this was attributed to the loss of coherence due to the smaller chordwise length of the LSB and the closer vicinity of the latter to the blade leading edge.

The vortex shedding from the LSB at the suction side of the propeller blades is responsible for a high frequency hump in the far-field noise spectra at $J = 0.4$ and 0.6. In accordance with the Paterson's model, the hump shifts toward higher frequencies when the rpm is increased. The comparison between clean and forced-BL noise spectra showed that, when the turbulator is used on both pressure and suction side or only at the suction side, the hump was removed and the noise was reduced of about 5 dB at $J = 0.4$ and 10 dB at $J = 0.6$. This constitutes a further prove of the link between the LSB and high frequency noise radiation.

The application of the semi-empirical model revealed that the different spanwise

blade sections emits tones at different amplitudes and frequencies, because of the variation of the relative velocity and angle of attack along the blade. Hence, the hump in the noise spectra is due to the superposition of the same tones. The comparison of the numerical predictions against the experimental results showed that the model satisfactory predicts the frequency range of the hump. The mismatch found for the amplitude was proven to be associated to an extreme sensitivity of the BPM model itself to the angle of attack. A variation of approximately 1 degree in the angle of attack across the blade was sufficient to align the numerical predictions closely with the experimental results.

BIBLIOGRAPHY

[1] John D. Anderson. *Fundamentals of Aerodynamics*. 4th. New York: McGraw-Hill, 2007.

[2] Pagano Antonio, Mattia Barbarino, Damiano Casalino, and Luigi Federico. "Tonal and Broadband Noise Calculations for Aeroacoustic Optimization of a Pusher Propeller". In: *Journal of Aircraft - J AIRCRAFT* 47 (May 2010), pp. 835–848. DOI: 10.2514/1.45315.

[3] H. Arbey and J. Bataille. "Noise generated by airfoil profiles placed in a uniform laminar flow". In: *Journal of Fluid Mechanics* 134 (1983), pp. 33–47. DOI: 10.1017/S0022112083003201.

[4] Elias Arcondoulis, Con Doolan, A Zander, and Laura Brooks. "A review of trailing edge noise generated by airfoils at low to moderate Reynolds number". In: *Acoustics Australia / Australian Acoustical Society* 36 (Mar. 2011).

[5] William G Bastedo Jr and Thomas J Mueller. "Spanwise variation of laminar separation bubbles on wings at low Reynolds number". In: *Journal of aircraft* 23.9 (1986), pp. 687–694.

[6] Michael Boutilier and Serhiy Yarusevych. "Parametric study of separation and transition characteristics over an airfoil at low Reynolds numbers". In: *Experiments in Fluids* 52 (June 2012). DOI: 10.1007/s00348-012-1270-z.

[7] Thomas Brooks, Dennis Pope, and Michael Marcolini. "Airfoil self-noise and prediction". In: *Nasa Reference Publication 1218* (Aug. 1989).

[8] Damiano Casalino, Edoardo Grande, Gianluca Romani, Daniele Ragni, and Francesco Avallone. "Definition of a benchmark for low Reynolds number propeller aeroacoustics". In: *Aerospace Science and Technology* 113 (2021), p. 106707.

[9] Edoardo Grande, Daniele Ragni, Francesco Avallone, and Damiano Casalino. "Laminar separation bubble noise on a propeller operating at low Reynolds numbers". In: *AIAA Journal* 60.9 (2022), pp. 5324–5335. DOI: 10.2514/1.J061691.

[10] Angus Leslie, Kee Choon Wong, and Doug Auld. "Experimental analysis of the radiated noise from a small propeller". In: *Proceedings of 20th International Congress on Acoustics, ICA*. 2010.

[11] J. F. Marchman and A. Abtahi. "Aerodynamics of an aspect ratio 8 wing at low Reynolds numbers". In: *Journal of Aircraft* 22.7 (1985), pp. 628–634. DOI: 10.2514/3.45176.

[12] Roberto Merino-Martinez, Alejandro Rubio Carpio, Lourenco Lima Pereira, Steve Herk, Francesco Avallone, Daniele Ragni, and Marios Kotsonis. "Aeroacoustic design and characterization of the 3D-printed, open-jet, anechoic wind tunnel of Delft University of Technology". In: *Applied Acoustics* 170 (Dec. 2020), p. 107504. DOI: 10.1016/j.apacoust.2020.107504.

[13] Robert W. Paterson, Paul G. Vogt, Martin R. Fink, and C. Lee Munch. "Vortex Noise of Isolated Airfoils". In: *Journal of Aircraft* 10.5 (1973), pp. 296–302. DOI: 10.2514/3.60229.

[14] Stefan Pröbsting, Fulvio Scarano, and Scott Morris. "Regimes of tonal noise on an airfoil at moderate Reynolds number". In: *Journal of Fluid Mechanics* 780 (Sept. 2015), pp. 407–438. DOI: 10.1017/jfm.2015.475.

[15] Stefan Pröbsting and S. Yarusevych. "Laminar separation bubble development on an airfoil emitting tonal noise". In: *Journal of Fluid Mechanics* 780 (Oct. 2015), pp. 167–191. DOI: 10.1017/jfm.2015.427.

[16] Gianluca Romani, Edoardo Grande, Francesco Avallone, Daniele Ragni, and Damiano Casalino. "Performance and noise prediction of low-Reynolds number propellers using the Lattice-Boltzmann method". In: *Aerospace Science and Technology* (Sept. 2021), p. 107086. DOI: 10.1016/j.ast.2021.107086.

[17] Connor E. Toppings and Serhiy Yarusevych. "Structure and dynamics of a laminar separation bubble near a wingtip". In: *Journal of Fluid Mechanics* 929 (2021), A39. DOI: 10.1017/jfm.2021.881.

[18] Jerry Westerweel. "Fundamentals of digital particle image velocimetry". In: *Measurement science and technology* 8.12 (1997), p. 1379.

[19] Christian Willert. "Stereoscopic digital particle image velocimetry for application in wind tunnel flows". In: *Measurement science and technology* 8.12 (1997), p. 1465.

[20] Serhiy Yarusevych, Pierre Sullivan, and John Kawall. "Coherent structures in an airfoil boundary layer and wake at low Reynolds numbers". In: *Physics of Fluids* 18 (Apr. 2006), p. 044101. DOI: 10.1063/1.2187069.

[21] Serhiy Yarusevych, Pierre Sullivan, and John Kawall. "On vortex shedding from an airfoil in low-Reynolds-number flows". In: *Journal of Fluid Mechanics* 632 (Jan. 2010), p. 245. DOI: 10.1017/S0022112009007058.

6

CO-ROTATING ROTORS: COMPUTATIONAL AEROACOUSTIC STUDY

This chapter aims to investigate, by means of Lattice-Boltzmann simulations, the flow-field and far-field noise of two co-axial co-rotating rotors operating at 3000 rpm in hover conditions. The two co-rotating configurations are made by 2×2*-bladed rotors with a fixed axial separation and two different azimuthal separations* $\Delta\phi$ *equal to* 84° *and* 12°*. Isolated 2- and 4-bladed rotors, are also simulated at the same operating conditions and used as aerodynamic and aeroacoustic reference. For both* $\Delta\phi = 84^\circ$ *and* 12°*, the upper rotor tip vortices are accelerated downstream due to the induction from the lower rotor, avoiding blade vortex interaction (BVI). The lower rotor tip vortices convect into the wake with a lower velocity, causing BVI for* $\Delta\phi = 12^\circ$*. The lower rotor shows a reduction of thrust, relative to the upper rotor, of 36% and 66% for* $\Delta\phi = 84^\circ$ *and* 12°*, respectively. For* $\Delta\phi = 12^\circ$*, the lower blades act as a wing flap for the upper ones, increasing their thrust. The tonal noise emission for the co-rotating rotors is driven by the interference between the acoustic waves from upper and lower rotors. Because of destructive interference, the configuration* $\Delta\phi = 84^\circ$ *shows a first harmonic up to 15 dB lower than* $\Delta\phi = 12^\circ$*, but still 4.5 dB higher than the isolated 4-bladed rotor.*

Parts of this chapter have been published in AESCTE Journal (2024) [12].

6.1. INTRODUCTION

After examining the aeroacoustic characteristics of an isolated rotor at low Reynolds numbers in detail in Chapters 4 and 5, this section shifts the focus to unconventional rotor configurations, specifically coaxial co-rotating rotors. These configurations are currently considered promising solutions for meeting both noise and aerodynamic requirements of UAM vehicles. As discussed in Sect. 2.5.1, co-rotating rotors have two primary design parameters: the axial distance Δx and azimuthal separation $\Delta\phi$, which significantly affect aerodynamic performance and noise emissions. Notably, rotor thrust and sound pressure levels are more influenced by azimuthal separation than by axial separation [16, 21, 14], with optimal azimuthal separation for achieving maximum thrust and minimum noise depending on factors such as the number of rotors, axial distance, blade design, and rotational speed [22].

The present chapter investigates, by means of Lattice-Boltzmann simulations, the flow mechanisms affecting the thrust generation and noise emissions of two co-rotating rotor configurations in hover, made by 2x2-bladed rotors having the same axial distance but different azimuthal separation $\Delta\phi = 84°$ and $12°$. Selected from Tinney's research [21], these configurations exhibit about 12.5 dB(A) difference in pressure level at the first rotor harmonic. Additionally, they are compared against isolated 2-bladed and 4-bladed rotors operating at the same conditions. The isolated rotor cases represent two extremes for the co-rotating rotors: a co-rotating configuration with zero axial separation can be seen as a single 4-bladed rotor (which has the same solidity as the co-rotating configuration), while a configuration with infinite axial separation can be seen as two 2-bladed rotors (same solidity as the upper and lower rotors of the co-rotating configuration). High-fidelity simulations are used to analyse how the mutual induction between the upper and lower rotors of the co-rotating configurations changes the evolution of the blades tip vortices and the pressure distribution on the blade surfaces with respect to the isolated rotors. This is linked to a significant difference in aerodynamic performances between upper and lower rotors. Finally, the acoustic waveforms and tonal noise emissions from the co-rotating rotors are analysed and compared against the isolated rotor cases. The final goal is to understand if the co-rotating rotors can achieve, at the same time, higher thrust and lower tonal noise relative to the isolated (2 and 4-bladed) rotors.

This chapter is organized as follows. In Sect. 6.2 the computational methodology is introduced and the rotor geometry, operating conditions and computational setup are described. In Sect. 6.3 the numerical results are validated against experimental results. In Sect. 6.4 the study of the flow field around the rotor, the aerodynamic performances and the noise emission are discussed. The main findings and future work are summarized in Sect. 6.5.

6.2. COMPUTATIONAL METHODOLOGY AND SETUP

The CFD/CAA solver Simulia PowerFLOW 6-2021, based on the Lattice-Boltzmann method (LBM) described in Sect. 3.1.1, is used in this work to compute the flow around the rotor and to predict the noise generated. This software has already been validated for aerodynamic and aeroacoustic studies on large and small scale rotors [1] [7] [18]. Furthermore, the works of Romani et. [20, 19] and Casalino et al. [6] show the robustness of

LBM for a small-scale rotor application. Far-field noise is computed by using the Ffowcs-Williams and Hawkings (FW-H) acoustic analogy applied to a permeable surface encompassing the rotors. The FW-H solver is based on a forward-time solution of [5] of the formulation 1A of Farassat and Succi [10] extended to a convective wave equation [3].

Two co-rotating co-axial rotors configurations (Fig. 6.1, first row), made by 2x2-bladed rotors, with azimuthal separations $\Delta\phi = 84°$ and 12° and a fixed axial separation $\Delta x = 2.8$ cm (0.06 D) are investigated together with isolated 2-bladed and 4-bladed rotors (Fig. 6.1, second row). The two co-rotating configurations are selected from Tinney's database [21] as they show a large difference in noise emission. All the rotors (co-rotating and single) have fixed-pitch APC 18x5.5 MR blades and a diameter D = 0.457 m. They operate in hover conditions with a rotational velocity of 3000 rpm, as summarized in Table 6.1. The blade-tip Mach number and chord-based Reynolds number based on the chord length at 75% of the blade span ($c_{75} = 3.02$ cm) are $M_t = 0.21$ and Re = 1.1×10^5, respectively.

Table 6.1: Simulated rotor configurations and operating conditions.

N	rotor type	$\Delta\phi$ [°]	Δz [cm]	V_∞ [m/s]	ω [rpm]
1	co-rotating	84	2.8	0.0	3000
2	co-rotating	12	2.8	0.0	3000
3	single 4-bladed	-	-	0.0	3000
4	single 2-bladed	-	-	0.0	3000

The computational fluid domain, illustrated in Fig. 6.2a, is a spherical volume of 185D with the co-rotating geometry at the center. Free-stream static pressure and velocity and a turbulence intensity of 0.1% of the free-stream velocity are prescribed on its outer boundary. The free-stream static pressure and velocity are set to 101.325 kPa and 0 m/sec, thus mimicking hover conditions. A total of 16 Variable Resolution (VR) regions are used to discretize the whole fluid domain, with the finest resolution regions placed around the blade leading edge and trailing edge. An additional mesh refinement is placed around the blade tips, due to their significance in capturing accurate flow physics in a rotor flow field. The smallest voxel size is 0.054 mm, resulting in $y+ \approx 15$ on the blade surface. The resulting number of fine equivalent voxels for the current study is 55 million. As sketched in Fig 6.2a, an acoustic sponge, defined by two concentric spheres of $18D$ and $70D$ radius, centered around the rotor, is used to dissipate the acoustic waves and minimize the reflections from the external boundaries.

The simulation time is 0.24 sec, which corresponds to a total of 12 rotor rotations. After 2 transient rotations, results are sampled for 10 rotations. The far-field aeroacoustic analysis is performed by using the permeable formulation of the FW-H analogy. Colin et al. [9] adopted the same approach for a similar case, finding that the permeable FWH closely matched experimental results. In this study a total of 3 cylindrical surfaces (represented in red in Fig. 6.2a) surrounding the rotor flow field are used as permeable FWH surfaces. In order to remove spurious noise caused by the hydrodynamic fluctuations in the wake of the propeller, data are sampled on the three permeable surfaces and the pressure resulting from FWH integration over these surfaces is averaged (which is equivalent to averaging the noise signals corresponding to the three different integration sur-

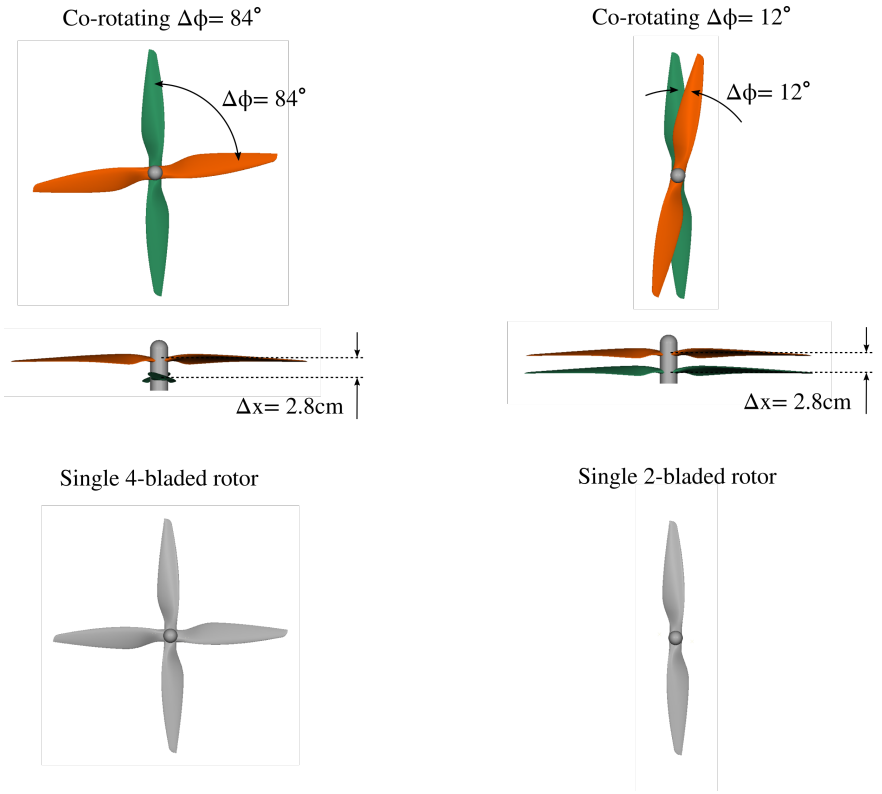

Figure 6.1: Co-rotating (first row) and single (second row) rotors geometries.

face). A similar approach is adopted by Mendez et a. [17], who also provide a mathematical expression to set the distance between the surfaces.. Far-field noise is computed using the circular array of 36 microphones, sketched in Fig. 6.2b. The array has a radius of 3D and it is in a plane perpendicular to the rotor plane. Acoustic data are sampled at 85 kHz and pressure spectra are then calculated using a Hanning window of 50% overlap and a frequency resolution of 10 Hz.

6.3. VALIDATION AGAINST EXPERIMENTAL RESULTS

The aerodynamic and aeroacoustic results are validated against the experimental data from [21] et al. The thrust coefficient, defined as $c_T = T/(\rho n^2 D^4)$ (where T is the thrust in N, ρ the air density in kg/m^3, n the propeller rotational frequency in Hz, D the propeller diameter in m), is reported in Table 6.2 from both simulations ($c_{T_{PF}}$) and experiments ($c_{T_{exp}}$), together with the difference between the two ($\Delta c_T = c_{T_{PF}} - c_{T_{exp}}$). The simulations underpredict the thrust coefficient by 13.6% and 11% for $\Delta\phi = 84°$ and $\Delta\phi = 12°$, respectively. The discrepancies are ascribed to the fact that the measurements were acquired during slow startup and shutdown cycles of the motor because of thermal drift due to load cell´s heating from the electric motor. Moreover, the experimental uncer-

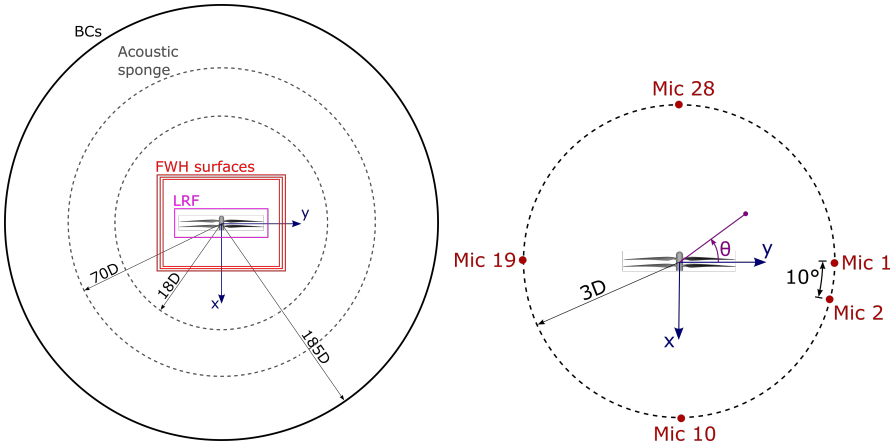

(a) (b)

Figure 6.2: Illustration of the computational setup (a). Sketch of the microphone array used for the far-field noise computation (b).

tainty due to repeatability, found from the difference in repeated thrust measurements of the same co-rotating configuration, is about 6% of the total thrust. From the numerical side, [4] et al. showed that the thrust increases with increasing mesh resolution for a small-scale rotor in hover at low-Reynolds numbers [11].

Table 6.2: Comparison between experimental and numerical thrust coefficient.

$\Delta\phi$ [°]	$c_{T_{PF}}$	$c_{T_{exp}}$	Δc_T
84	0.0915	0.104	-0.0125
12	0.0900	0.100	-0.0100

The far-field noise is plotted in Fig. 6.3 at a probe located at $x = 0.443$ m and $y = 0.372$ m. The frequency axis of each plot is normalized by the blade passing frequency BPF (100 Hz). To support the analysis of the numerical results, it is worth mentioning that the experimental spectra are affected by facility noise, responsible for the large broadband noise level at low-frequencies ($BPF < 3$), electric motor noise, causing high-frequency tones (above BPF 10) and presence of harmonics of the shaft frequency (BPF 0.5, 1.5, 2.5, etc.). The PowerFLOW spectra at BPF 1 and 2 compare reasonably well with the experimental ones, with a difference between 1.3 and 3.5 dB for both the co-rotating configurations. On the other side, the underestimation of broadband noise is expected. This is because, as shown by [20] et al., a low intrusive zig-zag trip on the blade surface that guides the VLES turbulence model toward a scale resolving mode and triggers the formation of vortical structures is required for turbulent boundary layer trailing-edge noise computation. Alternatively, as shown by Casalino et al. [8], the usage of a VLES model with transitional capabilities can be made to promote the onset of turbulent fluctuation in the boundary layer (this approach would lead to an elevated computational cost, given the necessity of maintaining a y+ on the blade surface of approximately 10).

Since the main focus of this work is on the effects of the azimuthal blade separation on forces and tonal noise (rather than broadband), a standard VLES model without trip is used, considering the additional effort required for a proper trip tuning.

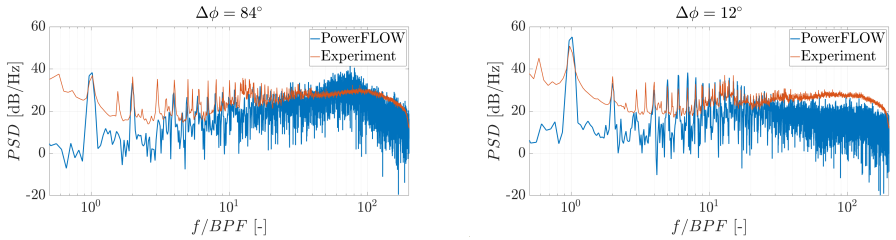

(a) (b)

Figure 6.3: Comparison between experimental and numerical far-field noise spectra at x = 0.443 m and y = 0.372 m.

6.4. FLOW AND ACOUSTIC ANALYSIS

This section analyses the flow field surrounding the co-rotating rotors by showing how the mutual induction between the upper and lower rotor influences the evolution of the blade tip vortices (Sec. 6.4.1) and surface pressure (Sec. 6.4.2). The knowledge about the flow behaviour is then linked to the aerodynamic performance (Sec. 6.4.3) and the tonal noise generation (Sec. 6.4.4).

6.4.1. TIP VORTICES INTERACTION

Fig. 6.4 shows the iso-surfaces of λ_2, colored by velocity magnitude (in the range from 0 to 25 m/s), which highlight the trajectories of the blades tip vortices. For the co-rotating configurations, the possible interactions between the tip vortices shed from the upper and lower blades and between the tip vortices and the blades themselves are investigated. For both $\Delta\phi = 84°$ and 12°, the upper blades tip vortices are ingested deeper radially into the faster-moving region of rotor wake and, during one rotor revolution, they convect downward by about 25% of the rotor radius. Conversely, the lower blades tip vortices show a lower convection velocity into the wake with respect to the upper ones, as can be inferred from the slope of their trajectories in the direction of the rotor axis.

Fig. 6.5, representing the instantaneous out-of-plane vorticity ω_z, highlights the exact position of the tip vortices cores from the blade surfaces. The higher convection velocity of the tip vortices shed from the upper rotors results in a miss distance, i.e. the x-distance between the blade and tip vortex core, of 0.15R and 0.2R for $\Delta\phi = 84°$ and 12°, respectively. Conversely, the tip vortices shed from the lower blades are in close proximity to the blade surface (see also the zoom boxes in Fig. 6.4). Specifically, for $\Delta\phi = 84°$, the lower rotor exhibits a miss distance of 0.06R; for $\Delta\phi = 12°$, instead, the miss distance is zero, resulting in blade vortex interaction (BVI) occurring at $y/R = 0.85$. The BVI observed with the co-rotating rotors differs from the conventional helicopter BVI, where blades periodically interact with the tip vortex generated by the preceding blade. The blade-to-blade distance in stacked rotors generates a potential upwash/downwash ef-

fect created by the tip vortex vicinity to respectively the outer and inner part of the blade. Despite not being cutting through the vortical velocity profile, we still refer to this phenomenon to as BVI, following the work of Hong et al. [13]. Nonetheless, the interaction is also characterized by a periodic component. Fig. 6.6a shows, for both the co-rotating configurations, the surface pressure spectra from a point located at the leading edge of the lower blades at the BVI location ($y/R = 0.85$), while Fig. 6.6b shows the total thrust evolution for 4 propeller rotations. The BVI for the configuration $\Delta\phi = 12°$ causes periodic surface pressure fluctuations, which translate into the harmonics visible in the left figure, and thrust fluctuations at 2/rev. On the other side, the case $\Delta\phi = 84°$ does not exhibit any substantial periodic fluctuation in both the surface pressure and thrust, due to the positive miss distance for the lower blades.

The behavior of the lower rotors is similar to the isolated rotor configurations. In particular, the single 4-bladed rotor is affected by BVI, likewise the lower rotor of the $\Delta\phi = 12°$ configuration, while for the single 2-bladed rotor, the tip vortex travels in proximity to the blade surface with a miss distance of 0.05R, similar to the lower rotor of the $\Delta\phi = 84°$ configuration.

To summarize, concerning BVI, having two rotors in hover in a co-rotating configuration is beneficial for the upper rotor. Indeed, due to the induction from the lower rotor, the tip vorteices from the upper rotor are accelerated downward, avoiding BVI with the upper/lower rotor blades. On the other hand, the lower rotor shows BVI when $\Delta\phi$ decreases, behaving similarly to a single 4-bladed rotor.

6.4.2. SURFACE PRESSURE AND SECTIONAL VELOCITY

The interaction between the induction fields created by the upper and lower rotors of the co-rotating configurations changes the pressure distribution on the surface of the blades with respect to the single rotor configurations. Figure 6.7 compares the surface pressure coefficient c_p at the fixed radial station r/R = 0.6 for the upper (left side) and lower rotor (right side) against the single 2- and 4-bladed rotor cases. Solid and dashed lines represent the suction and pressure side, respectively. The c_p at a generic radial section is calculated as $c_p = (p - p_\infty)/(0.5\rho_\infty V_{R_\infty}^2)$, where p is the time-averaged surface static pressure, p_∞ and ρ_∞ are the free-stream air pressure and density, respectively and V_{R_∞} is the free-stream velocity experienced by the rotor at that specific section, defined as $V_{R_\infty} = \sqrt{V_\infty^2 + (\omega r)^2}$, with V_∞ being the free-stream flow velocity in m/s, ω the propeller rotational speed in rad/s and r the radial position of the blade section in m. The c_p figure is corroborated with a contour plot of the time-averaged velocity magnitude V_R (Fig. 6.8) around the sections at $r/R = 0.6$. Note that for $\Delta\phi = 84°$, the flow is visualized in two separate planes, one aligned with the upper blade and one with the lower blade. Conversely, for $\Delta\phi = 12°$ one unique plane aligned with the upper rotor and containing both the upper and lower blade sections, is used. The error in the in-plane velocity component due to the misalignment of the plane with respect to the lower rotor is negligible.

For the upper rotor (Fig. 6.7 left), the c_p for the co-rotating configuration with $\Delta\phi = 12°$ is the highest one. In particular, the c_p for $\Delta\phi = 12°$ shows a significant difference with respect to $\Delta\phi = 84°$ and the single 4-bladed rotor (which appears to be the lowest one). On the other hand, the c_p for $\Delta\phi = 84°$ is only higher than the single 4-bladed rotor. The analysis of the flow around the blade sections in Fig. 6.8 proves that for $\Delta\phi = 12°$ the

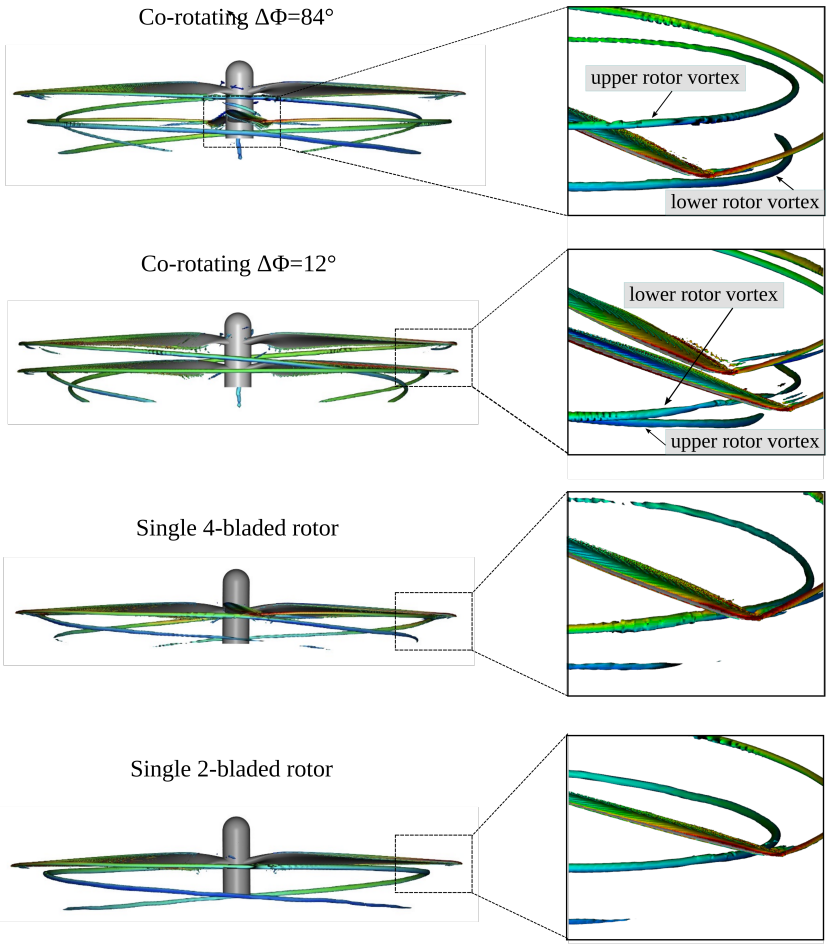

Figure 6.4: Iso-surfaces of λ_2 for the co-rotating and single rotor configurations.

lower blade, being in proximity of the upper one, behaves as a wing flap, increasing the suction (or decreasing the pressure) on the upper blade to values slightly higher than the single 2-bladed rotor.

The differences between the co-rotating and isolated cases are amplified at the lower rotor (Fig. 6.7 right), where both the single rotor cases show higher c_p compared to the co-rotating ones. The configuration $\Delta\phi = 12°$ exhibits the lowest c_p and hence poor aerodynamic performances. Furthermore, the co-rotating rotors show a negative c_p peak located at the pressure side (dashed line in the figure), which is associated with a negative angle of attack. This is due to the fact that the lower rotor, operating into the wake of the upper one, experiences a higher axial velocity that decreases the angle of

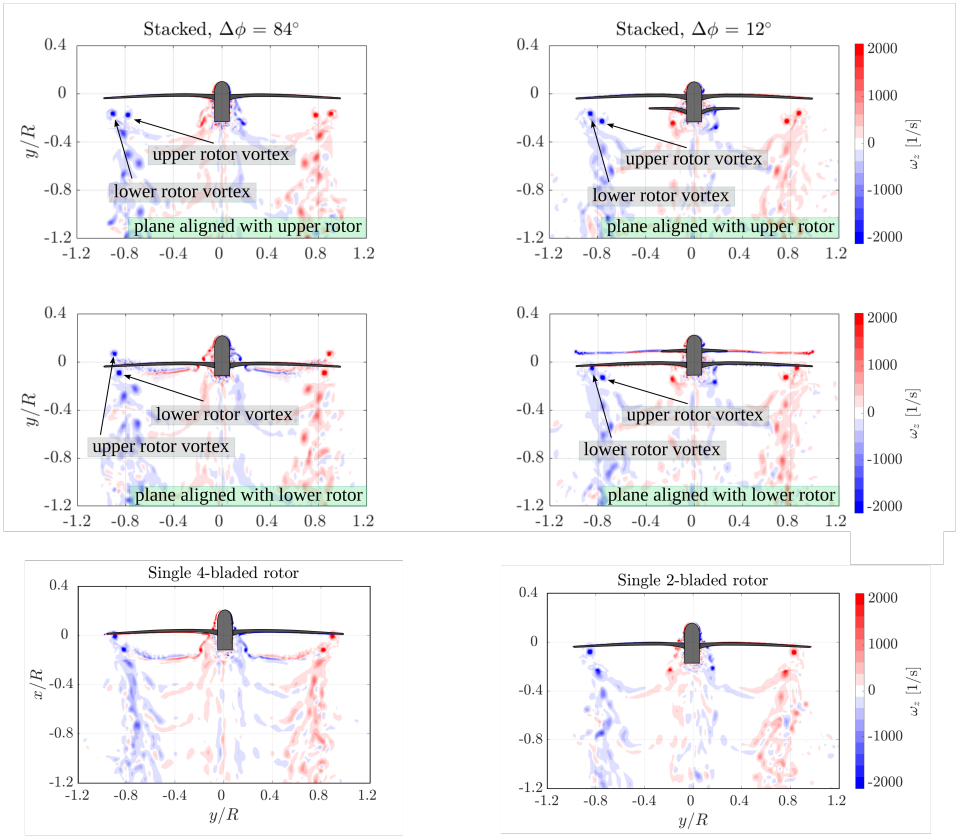

Figure 6.5: Contour plot of the instantaneous vorticity in xy-planes for both co-rotating (first and second row) and single rotors (third row).

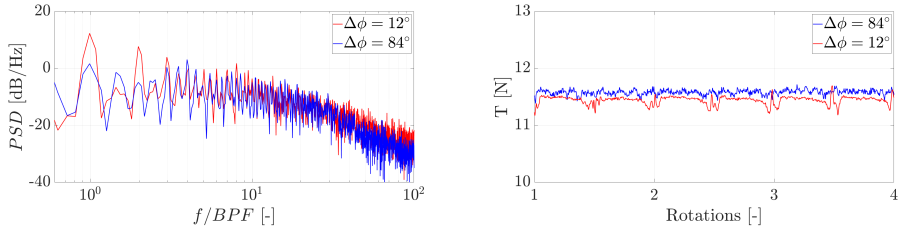

(a) (b)

Figure 6.6: Surface pressure spectra from a point on the lower rotors, at r/R = 0.85, of the co-rotating configurations (a). Total thrust evolution for four rotations (b).

attack. As expected, the flow analysis shows a reduced suction on the lower sections of the co-rotating cases relative to the isolated rotors. In particular, for $\Delta\phi = 12°$, as a counterpart of the flap effect (mentioned above), the upper section produces a substantial

decrease in velocity on the lower one (mainly at the leading edge).

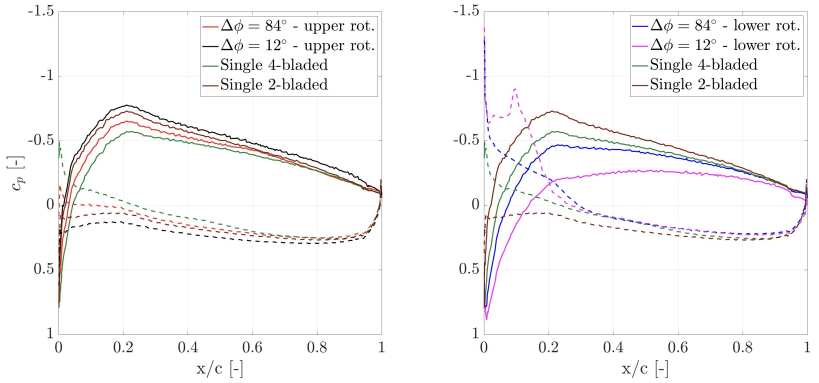

Figure 6.7: Comparison of surface pressure coefficient between the co-rotating and single rotors at r/R = 0.6. Solid and dashed lines represent suction and pressure side, respectively.

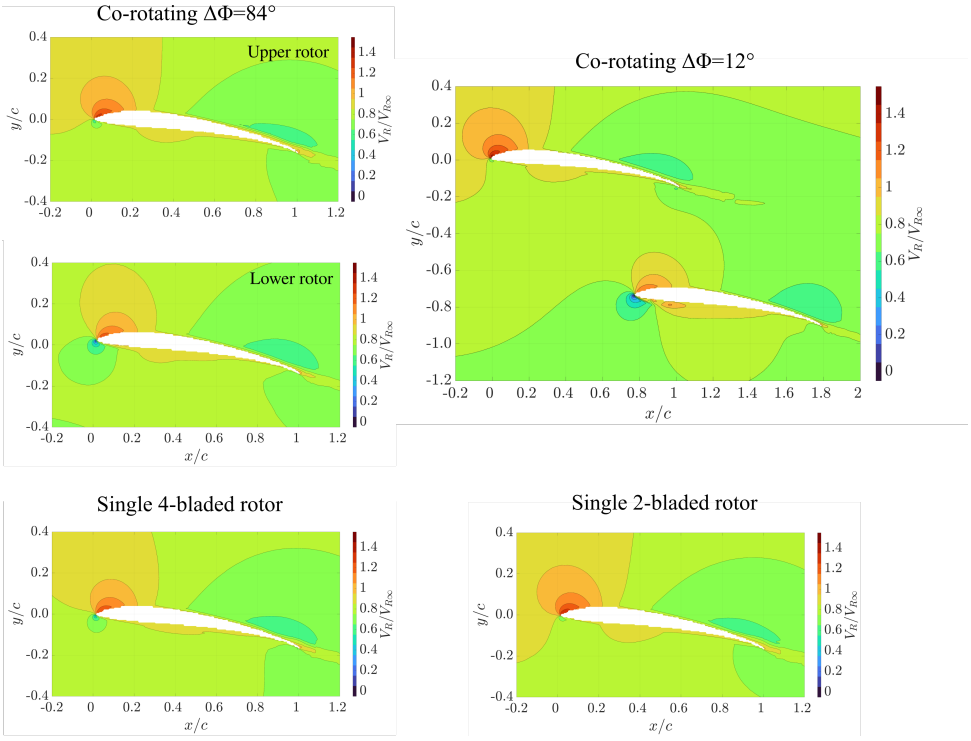

Figure 6.8: Mean velocity field around the blade cross-sections at $r/R = 0.6$ for both co-rotating (first row) and single rotor (second row) configurations.

Fig. 6.9 compares the surface pressure coefficient c_p between the two co-rotating cases at different radial stations (ranging from $r/R = 0.4$ to 0.9). The first row of the figure shows that the c_p of the upper rotor for the 12° configuration is higher at all the radial stations. At the lower rotor instead (second row of the figure), the c_p exhibits the opposite trend, i.e. it is considerably lower for $\Delta\phi = 12°$ up to $r/R = 0.8$. This is a direct consequence of the higher c_p at the upper rotor. At the lower blade, the pressure plateau that follows the c_p peak, visible until $r/R = 0.6$ for $\Delta\phi = 12°$ and, to a minor extent, also for $\Delta\phi = 84°$, is linked to flow separation [23, 2]. Finally, the vicinity of the tip vortex to the blade surface (discussed in Sect. 6.4.1) is responsible for the increase of c_p at $r/R = 0.9$. Indeed, the tip vortex induces an upward velocity on the outboard part of the blade, increasing the local angle of attack.

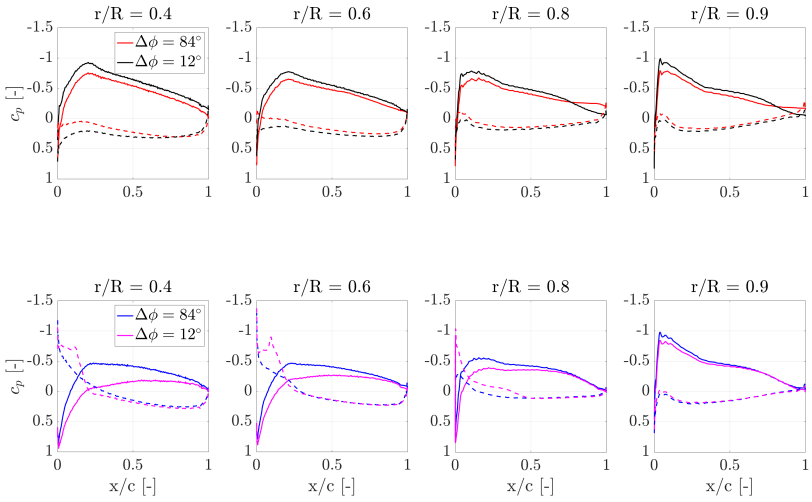

Figure 6.9: Comparison of surface pressure coefficient for the upper (first row) and lower rotor (second row) at different radial stations between the co-rotating configurations $\Delta\phi = \mathbf{84}°$ and $\mathbf{12}°$. Solid and dashed lines represent suction and pressure side, respectively.

6.4.3. AERODYNAMIC PERFORMANCE

The induction discussed above strongly affects the aerodynamic performance of the co-rotating rotors. To assess this, the thrust c_T and torque c_Q coefficients of the co-rotating configurations are calculated and compared against the isolated 2-bladed and 4-bladed rotors.

The c_T for both co-rotating and single rotors is represented in the bar plot in Fig. 6.10 (left). Overall, the total c_T (defined in Sect 6.3) for the configurations $\Delta\phi = 84°$ and 12° is, respectively, 2.8% and 1.5% higher than the single 4-bladed rotor. The analysis of the thrust produced by the upper and lower rotors, taken individually, shows that, for both $\Delta\phi = 84°$ and 12°, the c_T of the upper rotor is higher than the lower one. This thrust

imbalance is a direct consequence of the c_p distributions observed in Sect. 6.4.2. For $\Delta\phi = 12°$, because of the lower rotor behaving as a wing flap, the upper rotor generates 11.4% more thrust than the single 2-bladed rotor. In this case, the increased upper rotor thrust induces more axial velocity at the lower rotor, thus decreasing the thrust of the latter to lower values with respect to $\Delta\phi = 84°$. The analysis of the torque coefficient, defined as $c_Q = Q/(\rho n^2 D^5)$, where Q is the torque in Nm, indicates that the c_Q for the two co-rotating configurations is the same as to the single 4-bladed rotor. Additionally, in comparison to the single 2-bladed rotor, the upper rotor for $\Delta\phi = 84°$ shows the same c_Q, while for $\Delta\phi = 12°$, the c_Q is 10.7% higher. In contrast, the lower rotor, for both $\Delta\phi$, shows a reduced c_Q (with respect to the single 2-bladed case) due to their poor aerodynamic performances.

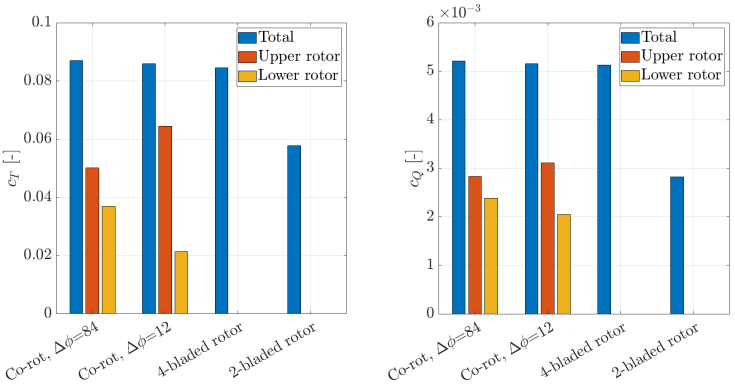

Figure 6.10: Comparison of total thrust and torque between the two co-rotating configuration with $\Delta\phi = 84°$ and 12° and the single 4-bladed and 2-bladed rotors.

To dig more into the differences between the two configurations, the spanwise distribution of c_T is plotted in Fig. 6.11. The figure shows that the rotor coupling strongly affects both the amplitude and shape of the radial distribution of c_T. While the upper rotor exhibits a smooth thrust distribution, the lower rotor of both the co-rotating configurations shows a change in the thrust slope at about $r/R = 0.85$, which is the radial position identified in Sect. 6.4.1 where the blade tip vortex core is located. The tip vortex causes downwash at the inner part of the blade and upwash at the outboard part, locally decreasing α and consequently c_T over the former region and increasing α and c_T over the latter. This is in agreement with Hong et al. [13], who also show the higher induction velocity at the blade tip. The increase in thrust is higher for $\Delta\phi = 12°$ because the tip vortex is at the rotor plane. The comparison with the single rotors shows, for the 4-bladed one, lower c_T values with respect to the upper rotor of both co-rotating configurations and a sharp thrust peak at $r/R = 0.95$, which is associated with a stronger BVI effect. On the other hand, the c_T of the single 2-bladed rotor is higher than the upper rotor for the 84° configuration and lower of the upper rotor for the 12° configuration because the lower rotor has a positive effect on the thrust of the upper rotor, as shown in Sect. 6.4.2.

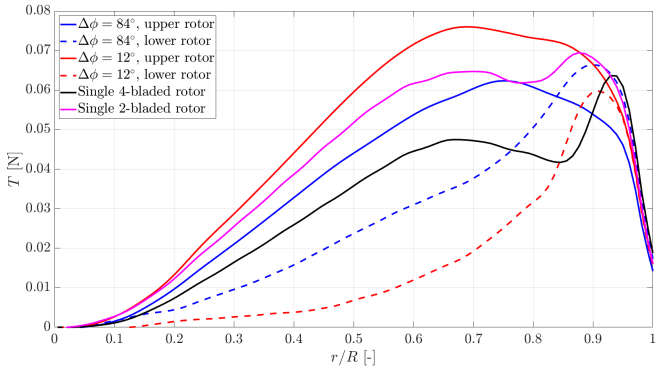

Figure 6.11: Comparison of spanwise distribution of thrust between the two co-rotating configuration with $\Delta\phi = \mathbf{84}°$ and $\mathbf{12}°$ and the single 4-bladed and 2-bladed rotors.

The differences in thrust between upper and lower rotor and the single 2-bladed rotor are reported in Tab. 6.3.

Table 6.3: Thrust variation between upper/lower rotor of the co-rotating configurations and the single 2-bladed rotor.

$\Delta\phi$ [°]	Upper rotor	Lower rotor
84	-13.0%	-36.4%
12	+11.4%	-63.0%

The vicinity of the tip vortex core to lower blades surface, as a first approximation, can be considered negligible in the variation of total thrust. The velocity induced by the tip vortex on the blade surface scales linearly with the distance from the vortex core, hence this effect is nearly local (as shown in Fig. 6.11).

6.4.4. FAR-FIELD NOISE

By using the circular array of 36 microphones sketched in Fig. 6.2b, it is evaluated if the co-rotating configurations can reduce the tonal noise emission with respect to the single 2-bladed and 4-bladed rotors. The tonal noise directivity for the first BPF is calculated and plotted in Fig. 6.12, where the two co-rotating rotors are individually compared to the single 4- and 2-bladed rotors. Note that for the two co-rotating rotors the first BPF is equal to 100 Hz, as for the single 2-bladed rotor, instead for the single 4-bladed rotor the first BPF is 200 Hz. For a meaningful comparison, the SPL of each single rotor is scaled with the thrust of the co-rotating configuration used as a comparison. The scaling is based on the assumption that the tonal noise is dominated by steady loading noise. Furthermore, the torque contribution to tonal noise is considered negligible. In light of this, the tonal noise is approximately proportional to the thrust T as $SPL \propto 20\log(T/T_{ref})$ [15].

The comparison for $\Delta\phi = 84°$ (Fig. 6.12, left) reveals that this configuration is overall acoustically more efficient than the single 2-bladed rotor, being about 15 dB quieter,

apart around $\theta = \pm 90°$ which are the directions perpendicular to the rotor plane. Instead, with respect to the single 4-bladed rotor, it generates overall more noise (+4.5 dB at $\theta = 0°$), apart around the upstream and downstream positions. On the other hand, the tonal noise emission for the configuration $\Delta\phi = 12°$ (Fig. 6.12, right) is overall significantly higher than the single 4-bladed rotor (+21.5 dB at $\theta = 0°$), and it is comparable to the single 2-bladed rotor, being 1.7 dB louder. The difference in noise emission between the two co-rotating configurations is due to constructive and destructive interference between the acoustic waves radiated by the upper and lower rotors. This is shown in Fig. 6.13 where the acoustic pressure signals from the upper and lower rotor at Mic 1 are plotted separately, for four propeller rotations. The resulting waveforms from the upper and lower rotor, if low-pass filtered, are similar to each other but time-shifted. The time-shift correlates to the azimuthal separation as $\Delta\phi/(n \cdot 360)$, where n is the rotational speed in Hz. Consequently, for $\Delta\phi = 84°$ the acoustic waveforms are more out of phase compared to $\Delta\phi = 12°$, thus justifying the different tonal noise components. Tinney at al. [21] demostrated that the total acoustic waveform from the co-rotating system can be estimated as a linear superposition of the contribution of the single rotors. The increased high-frequency pressure fluctuations visible at the upper rotor for $\Delta\phi = 84°$ are likely linked to the unsteadiness induced by the tip vortex shed from the upper rotor, which remains closer to the rotor disk. Specifically, in this case, the tip vortex travels above the lower rotor blades and becomes unstable at the passage of the lower blades.

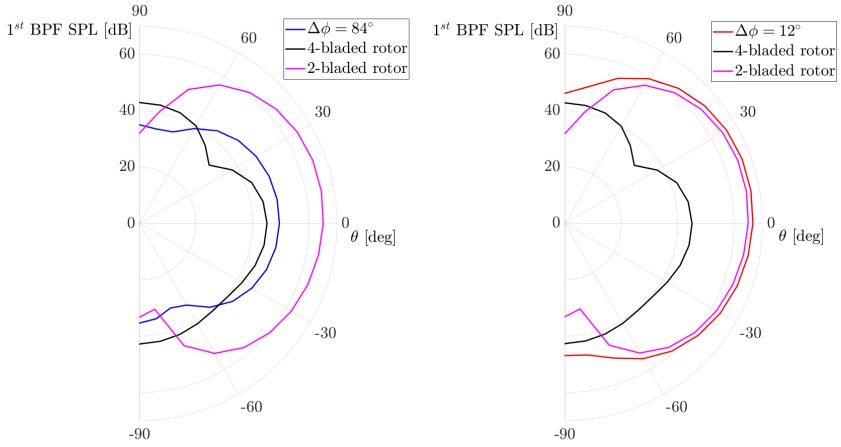

Figure 6.12: Directivity of the **1st** BPF for the co-rotating setup $\Delta\phi = \mathbf{84°}$ (left) and $\Delta\phi = \mathbf{12°}$ (right), compared to the single 4-bladed and 2-bladed rotors.

Fig 6.14, shows a comparison of noise spectra for the two co-rotating configurations at the rotor plane (mic 1) and upstream of the rotor plane (mic 28). At mic 1 (in-plane), the configuration $\Delta\phi = 12°$ exhibits a first BPF tone 17 dB higher with respect to $\Delta\phi = 84°$ due to destructive interference described above. At mic 28 (out-of-plane), the BPF 1 tone has a level comparable to the broadband noise, with a substantial decrease with respect to mic 1. This is expected from the loading noise directivity, which is more pronounced

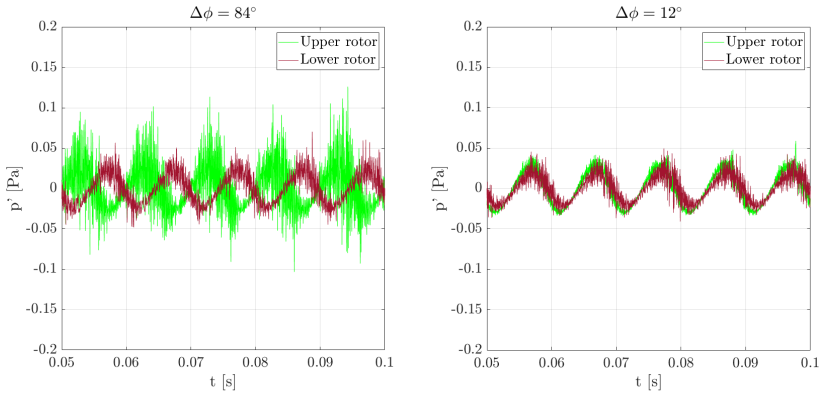

Figure 6.13: Comparison between the acoustic pressure time series from the upper and lower rotors at mic 1.

at the rotor plane. The difference at BPF 1 between the two configurations reduces to 13 dB. Interestingly, for $\Delta\phi = 12°$ there is a raise of high order harmonics that is associated with unsteady pressure fluctuations caused by BVI (Sect. 6.4.1).

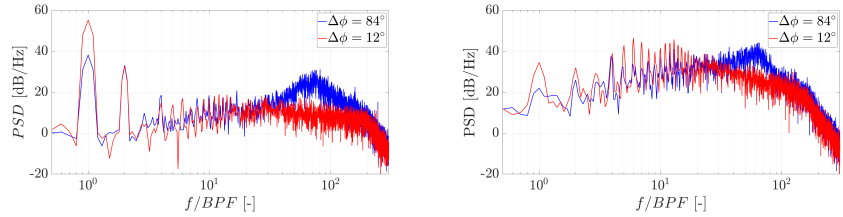

(a) (b)

Figure 6.14: Comparison of far-field noise spectra at mic 1 (a) and mic 28 (b).

6.5. CONCLUSIONS

This chapter presents a computational aeroacoustic study on two co-rotating rotors in hover, formed by two identical 2-bladed APC 18x5.5 MR propellers stacked on top of each other. By adopting two azimuthal separations $\Delta\phi = 84°$ and $12°$ between the upper and lower rotor blades and keeping the same axial separation, two different configurations are simulated and compared. In addition, isolated 2-bladed and 4-bladed rotors with the same type of blades as the co-rotating configurations are also simulated at the same conditions and used as aerodynamic and aeroacoustic reference. The lattice Boltzmann method implemented in the CFD/CAA solver Simulia PowerFLOW is used to obtain the flow solution around the rotors while the noise generation is computed by means of the Farassat's formulation 1A of the FW-H equation.

The mutual induction between upper and lower rotor of the co-rotating systems affects the evolution of the blades tip vortices and the distribution of surface pressure. For both azimuthal separations, the tip vortices from the upper rotor do not originate any BVI because it is ingested into the faster-moving region of the rotor wake and accelerated downstream. The lower blades tip vortices stagnate into a region close to the rotor plane and leads to BVI for $\Delta\phi = 12°$ at about 85% of the blade span, similarly to the isolated 4-bladed rotor. The surface pressure coefficient c_p, hence the thrust, on the upper rotor of both configurations is significantly higher than the c_p on the lower rotor since the latter, operating into the wake of the upper one, experiences a reduced angle of attack. Furthermore, for $\Delta\phi = 12°$, the lower blades acts as a wing flap for the upper ones, increasing the suction and consequently the thrust of the upper rotor.

Overall, the co-rotating configurations show a total thrust increase with respect to the single 4-bladed rotor of 2.8% and 1.4% for $\Delta\phi = 84°$ and 12°, respectively. On the other side, the differences in thrust between upper and lower rotor and the single 2-bladed rotor (see Tab. 6.3) represent a quantification of the inflow interaction between upper and lower rotors. Interestingly the lower rotor for $\Delta\phi = 12°$ shows 63% of thrust reduction related to the single 2-bladed rotor.

The tonal noise emission is driven by the interference between the acoustic waveforms from the upper and lower rotor. Due to destructive interference, the configuration $\Delta\phi = 84°$ shows, at the rotor plane, a first BPF tone 15 dB lower than $\Delta\phi = 12°$, but 4.5 dB higher the single 4-bladed rotor, which is the configuration that generates overall less tonal noise.

The main issue of a co-rotating configuration is constituted by the poor aerodynamic performance of the lower rotor (especially when the ayimuthal separation is decreased). A possible strategy would be to differentiate the geometry of upper and lower rotors, for instance using an upper rotor with a smaller radius than the lower one. In this way, only the inner part of the lower rotor is affected by the wake of the upper one and the outer part would work in a clean flow. However, the thrust reduction due to a smaller upper blade area must be considered. Furthermore, a positive variation of the collective pitch angle of the lower rotor would increase the angle of attack, and consequently the produced thrust. An increase in thrust for the lower rotor would be also beneficial for tonal noise reduction of configurations with azimuthal separation close to 90°. As seen in this study for $\Delta\phi = 84°$, a higher thrust would translate into a higher amplitude of the acoustic waveform from the lower rotor, thus in a more efficient destructive interference with the upper rotor waveform.

BIBLIOGRAPHY

[1] Francesco Avallone, L Ende, Q Li, Daniele Ragni, Damiano Casalino, Georg Eitelberg, and L Veldhuis. "Aerodynamic and Aeroacoustic Effects of Swirl Recovery Vanes Length". In: *Journal of Aircraft* (Aug. 2019). DOI: 10.2514/1.C035552.

[2] M. Brendel and T. Mueller. "Boundary-layer measurements on an airfoil at low Reynolds numbers". In: *Journal of Aircraft* 25 (July 1988), pp. 612–617. DOI: 10.2514/3.45631.

[3] Guillaume Brès, Franck Pérot, and David Freed. "Properties of the lattice Boltzmann method for acoustics". In: *15th AIAA/CEAS Aeroacoustics Conference (30th AIAA Aeroacoustics Conference)*. 2009, p. 3395.

[4] D Casalino, E Grande, G Romani, D Ragni, and F Avallone. "Towards the definition of a benchmark for low Reynolds number propeller aeroacoustics". In: *Journal of Physics: Conference Series*. Vol. 1909. 1. IOP Publishing. 2021, p. 012013.

[5] Damiano Casalino. "An advanced time approach for acoustic analogy predictions". In: *Journal of Sound and Vibration* 261.4 (2003), pp. 583–612.

[6] Damiano Casalino, Edoardo Grande, Gianluca Romani, Daniele Ragni, and Francesco Avallone. "Definition of a benchmark for low Reynolds number propeller aeroacoustics". In: *Aerospace Science and Technology* 113 (2021), p. 106707.

[7] Damiano Casalino, Andreas Hazir, and Adrien Mann. "Turbofan Broadband Noise Prediction using the Lattice Boltzmann Method". In: May 2016. DOI: 10.2514/6.2016-2945.

[8] Damiano Casalino, Gianluca Romani, Raoyang Zhang, and Hudong Chen. "Lattice-Boltzmann calculations of rotor aeroacoustics in transitional boundary layer regime". In: *Aerospace Science and Technology* 130 (2022), p. 107953.

[9] Yann Colin, Bastien Caruelle, and AB Parry. "Computational strategy for predicting CROR noise at low-speed Part III: investigation of noise radiation with the Ffowcs-Williams Hawkings analogy". In: *18th AIAA/CEAS Aeroacoustics Conference (33rd AIAA Aeroacoustics Conference)*. 2012, p. 2223.

[10] F Farassat and George P Succi. "A review of propeller discrete frequency noise prediction technology with emphasis on two current methods for time domain calculations". In: *Journal of Sound and Vibration* 71.3 (1980), pp. 399–419.

[11] Stewart Glegg and William Devenport. *Aeroacoustics of low Mach number flows: fundamentals, analysis, and measurement*. Academic Press, 2017.

[12] Edoardo Grande, Shubham Shubham, Francesco Avallone, Daniele Ragni, and Damiano Casalino. “Computational aeroacoustic study of co-rotating rotors in hover”. In: *Aerospace Science and Technology* 153 (2024), p. 109381. DOI: 10.1016/j.ast.2024.109381.

[13] Yoonpyo Hong, Dawoon Lee, Sunwoong Yang, Hyojin Kook, and Kwanjung Yee. “Exploration of stacked rotor designs for aerodynamics in hover”. In: *Aerospace Science and Technology* 141 (2023), p. 108557.

[14] George Jacobellis, Rajneesh Singh, Chloe Johnson, Jayant Sirohi, and Rob McDonald. “Experimental and computational investigation of stacked rotor performance in hover”. In: *Aerospace Science and Technology* 116 (2021), p. 106847.

[15] Mark T Kotwicz Herniczek, Daniel Feszty, Sid-Ali Meslioui, Jong Park, and Fred Nitzsche. “Evaluation of acoustic frequency methods for the prediction of propeller noise”. In: *AIAA Journal* 57.6 (2019), pp. 2465–2478.

[16] Anton J Landgrebe and E Dean Bellinger. “Experimental investigation of model variable-geometry and ogee tip rotors.[aerodynamic characteristics of variable geometry rotary wings]”. In: (1974).

[17] S Mendez, M Shoeybi, SK Lele, and P Moin. “On the use of the Ffowcs Williams-Hawkings equation to predict far-field jet noise from large-eddy simulations”. In: *International Journal of Aeroacoustics* 12.1-2 (2013), pp. 1–20.

[18] Clément Nardari, Damiano Casalino, Francesco Polidoro, Vedran Coralic, Phoitack Lew, and John Brodie. “Numerical and Experimental Investigation of Flow Confinement Effects on UAV Rotor Noise”. In: May 2019. DOI: 10.2514/6.2019-2497.

[19] Gianluca Romani, Edoardo Grande, Francesco Avallone, Daniele Ragni, and Damiano Casalino. “Computational study of flow incidence effects on the aeroacoustics of low blade-tip Mach number propellers”. In: *Aerospace Science and Technology* 120 (2022), p. 107275.

[20] Gianluca Romani, Edoardo Grande, Francesco Avallone, Daniele Ragni, and Damiano Casalino. “Performance and noise prediction of low-Reynolds number propellers using the Lattice-Boltzmann method”. In: *Aerospace Science and Technology* (Sept. 2021), p. 107086. DOI: 10.1016/j.ast.2021.107086.

[21] Charles E Tinney and John Valdez. “Thrust and Acoustic Performance of Small-Scale, Coaxial, Corotating Rotors in Hover”. In: *AIAA Journal* (2019), pp. 1–11.

[22] John A. Valdez and Charles E. Tinney. “Wake of a Coaxial Corotating Rotor in Hover”. In: *AIAA Journal* 60.8 (2022), pp. 4829–4839. DOI: 10.2514/1.J061651. eprint: https://doi.org/10.2514/1.J061651. URL: https://doi.org/10.2514/1.J061651.

[23] Serhiy Yarusevych, Pierre Sullivan, and John Kawall. “Coherent structures in an airfoil boundary layer and wake at low Reynolds numbers”. In: *Physics of Fluids* 18 (Apr. 2006), p. 044101. DOI: 10.1063/1.2187069.

7

CONCLUSIONS

This concluding chapter summarizes the work presented in the thesis, highlighting its key findings. It also offers recommendations and insights for future research directions.

7.1. SUMMARY AND CONCLUSIONS

In Chapter 1, the primary research objective was encapsulated in the following statement:

To evaluate the noise emitted by both conventional and unconventional propeller configurations operating at low Reynolds numbers.

This objective was broken down into four sub-objectives. In this concluding chapter, these sub-objectives are evaluated based on the work presented in the preceding chapters.

1. *Characterize the primary tonal and broadband noise sources in isolated propellers operating at low-Reynolds numbers under clean inflow conditions.*

   To address this aspect a 2-bladed propeller with a 30 cm diameter is designed and tested in an anechoic wind tunnel at a chord-based Reynolds number of the order of 10^4. Far-field noise measurements are conducted at a fixed rpm, under both hover and axial flow conditions (with an advance ratio J ranging from 0 to 0.6) and are complemented by loads measurements and flow visualization techniques, including phase-locked PIV and oil flow.

   The far-field noise spectra exhibit both discrete tones, mostly occurring at multiples of the BPF, and a broadband component. As the advance ratio J increases, the amplitude of the first BPF (133 Hz), which is associated to steady loading, diminishes due to the corresponding reduction in thrust. At $J = 0$ (hover condition), there is a higher tonal noise content between BPF 5 and 10, primarily linked to unsteady pressure fluctuations caused by BVI and flow recirculation within a confined environment like an anechoic chamber. BVI is generated by the impact of a blade with the tip vortex generated by the preceding blade and fades when J is increased, due to the downstream convection of the wake. The flow recirculation in the anechoic tunnel generates additional unsteady blade loading and contributes to the increasing trend of these tones.

   The main sources of broadband noise in the low to mid-frequency range (up to about BPF 20) differ according to the various advance ratio conditions. For $J = 0$, turbulence ingestion noise at the leading edge is considered the dominant source, resulting in higher noise levels compared to cases with positive J. For these cases, trailing edge noise is the dominant source. The high frequency hump centered around BPF 50 (7 kHz), particularly prominent at higher J, is attributed to wake vortex shedding originating from a LSB at the blade suction side. The presence of the LSB is confirmed by oil flow visualizations and rms velocity contours. As J decreases (indicating an increase in the angle of attack over the blade), the LSB shifts toward the leading edge and decreases in size. The case $J = 0$ is the only one where the LSB does not extend to the very tip region. The hypothesis is that the BVI washes out the LSB at the tip. Conversely, the case $J = 0.6$ shows a long bubble without a clear evidence of reattachment, indicating that the LSB likely bursts. This results in more efficient wake vortex shedding characterized by coherent structures with a larger length scale (compared to other scenarios with lower J)

and notable velocity fluctuations, reaching 22% of the free-stream velocity. Consequently, the high-frequency noise emission is about 10 dB higher than $J = 0$.

2. *Investigate the unique flow phenomena at low-Reynolds numbers, such as the behavior of the transitional boundary layer, and quantify their effects on the far-field noise spectrum.*

   As introduced in Point 1, the boundary layer over the small-scale propeller under study is characterized by a LSB and subsequent vortex shedding, which causes a noticeable high-frequency hump in the far-field noise spectra. To further investigate the characteristics of the LSB and related noise emission, experimental measurements from Point 1 are extended to include different rotational speeds. These are conducted not only on a smooth surface (clean) but also with a turbulator applied on the suction side (forced-BL p.s.), the pressure side (forced-BL p.s.), and both sides (forced-BL) of the propeller blades to force the transition of the boundary layer from laminar to turbulent.

   Oil-flow visualizations for the clean blade confirm the presence of a LSB on the blade suction side, as previously discussed. When the turbulator is employed, the LSB is suppressed, and in all cases, the flow remains attached after the turbulator and eventually separates near the trailing edge. From the analysis of the instantaneous vorticity field a clear coherent vortex shedding is identified at $J = 0.6$ and 0.4 only. The shedding frequency, calculated by means of a statistical approach, is found to be 9.6 kHz and 8.6 kHz at $J = 0.4$ and 0.6, respectively. Coherent vortical structures are not clearly visible at $J = 0$ and 0.24 and this is attributed to the loss of coherence due to the smaller chordwise length of the LSB, which is positioned closer to the blade leading edge.

   The evident high-frequency hump in the far-field noise spectra at $J = 0.4$ and 0.6, due to vortex shedding from the LSB, shifts toward higher frequencies with increasing rpm, in accordance with the Paterson's model. The comparison between clean and forced-BL noise spectra showed that, when the turbulator is used on both pressure and suction side or only at the suction side, the hump disappears and the noise is reduced by about 5 dB at $J = 0.4$ and 10 dB at $J = 0.6$. This constitutes a further evidence of the link between the LSB and high frequency noise radiation.

   This study demonstrates that high-frequency noise radiation is a significant contributor to the overall noise levels of UAVs and UAM vehicles, highlighting the need for accurate predictions during mission-level analysis to avoid underestimating noise levels by several dB.

3. *Determine how these characteristic low-Reynolds noise sources can be modelled using low-fidelity methods.*

   An effort to model the airfoil blade self-noise, particularly the high-frequency hump previously discussed, is made by extending the semi-empirical BPM model, originally developed to predict self generated noise of a steady airfoil encountering smooth flow, to a rotating blade. This is achieved by employing a strip approach, wherein the propeller blade is divided in N spanwise elements (sources), and the

noise contribution from each element is calculated using the BPM model. The main assumption of the strip theory is the absence of aerodynamic interaction between elements, thus the effect of the spanwise velocity component is discarded. The airfoil self-noise mechanisms implemented in the current work are the laminar boundary layer vortex shedding (LBL-VS) noise and turbulent boundary layer trailing edge (TBL-TE) noise.

The LBL-VS model reveals that the different spanwise sections of the blade emits tones at different amplitudes and frequencies, because of the variation in relative velocity and angle of attack along the blade. Consequently, the hump in the noise spectra results from the superposition of these tones.

The comparison of the numerical predictions against the experimental results shows that the model satisfactory predicts the frequency range of the hump. The discrepancy observed in the amplitude is shown to be linked to the BPM model's high sensitivity to the input angle of attack, which is predicted by means of the low-fidelity *Opty∂B*-BEMT tool. Adjusting the angle of attack by approximately 1 deg across the entire blade or using as input the angle of attack derived from an high-fidelity simulations improved the alignment of numerical predictions with experimental data. In all cases, the TBL-TE model predicts significantly lower noise levels, thereby excluding trailing edge noise as a major source of high-frequency noise.

Taking into account the model's high sensitivity to input aerodynamic parameters, it is considered premature to utilize this method at an industrial level, as it may result in significant under- or overestimations of noise levels. However, it can still be useful for quick and rough estimations in preliminary analyses.

4. *Analyze the aeroacoustic characteristics of unconventional rotor configurations, such as co-rotating rotors, and evaluate their potential to reduce noise while enhancing the aerodynamic performance in comparison to traditional isolated rotors.*

   Two co-rotating rotors in hover, each consisting of identical 2-bladed propellers with a diameter of 45.7 cm, are numerically investigated using Lattice Boltzmann simulations. The two configurations are obtained by employing two azimuthal separations, $\Delta\phi = 84°$ and $12°$, between the upper and lower rotor blades, while maintaining the same axial separation. Additionally, isolated 2-bladed and 4-bladed rotors, with the same blade type as the co-rotating configurations, are simulated under identical conditions and serve as aerodynamic and aeroacoustic benchmarks. Noise generation is calculated by means of Farassat's formulation 1A of the FW-H equation.

   The analysis of the flow around the rotors aimed to understand how the mutual induction between the upper and lower rotors influences the development of tip vortices and the distribution of surface pressure. For both azimuthal separations, the tip vortices generated by the upper rotor do not cause blade-vortex interaction (BVI) as they are ingested into the faster-moving region of the rotor wake and accelerated downstream. In contrast, the lower blades tip vortices stagnate into a region close to the rotor plane and leads to BVI for $\Delta\phi = 12°$ at about 85% of the blade span, similar to the behavior observed in the isolated 4-bladed rotor.

The surface pressure coefficient c_p, and consequently the thrust, is significantly higher on the upper rotor in both configurations compared to the lower rotor. This difference arises because the lower rotor operates into the wake of the upper rotor, experiencing a reduced angle of attack. Furthermore, for $\Delta\phi = 12°$, the lower blades acts as a wing flap for the upper blades, enhancing suction and consequently increasing the thrust of the upper rotor. Additionally, the thrust differences between the upper rotor and the single 2-bladed rotor, as well as between the lower rotor and the single 2-bladed rotor, represent a quantification of the inflow interaction between upper and lower rotors. Notably, for $\Delta\phi = 12°$, the lower rotor experiences a 63% thrust reduction relative to the single 2-bladed rotor.

Finally, the tonal noise emissions from the two co-rotating configurations are individually compared to those of the single 4- and 2-bladed rotors. To ensure a meaningful comparison, the SPL of each single rotor is scaled with the thrust of the co-rotating configuration used as a comparison. The tonal noise levels are primarily driven by the interference between the acoustic waveforms generated from the upper and lower rotor. When low-pass filtered, these waveforms appear similar but are time-shifted relative to each other. The time-shift correlates to the azimuthal separation as $\Delta\phi/(n \cdot 360)$, where n is the rotational speed in Hz. As a result, for $\Delta\phi = 84°$ the acoustic waveforms are more out of phase compared to $\Delta\phi = 12°$, leading to destructive interference. Due to this effect, the configuration $\Delta\phi = 84°$ shows, at the rotor plane, a first BPF tone that is 15 dB lower than that of $\Delta\phi = 12°$. However, it remains 4.5 dB higher than the single 4-bladed rotor, which produces the lowest overall tonal noise level.

7.2. RECOMMENDATIONS FOR FUTURE WORK

This section provides recommendations derived from the experience gained during this research work, intended to guide potential future studies. Concerning the investigation of the isolated propeller presented in Chapters 4 and 5:

- The propeller test-rig could be optimized to minimize vibrations and, thereby further improving the quality of the measurements. The load and torque cell system depicted in Fig. 4.2b introduced some flexibility, causing slight movement in the propeller axis. It is expected that the replacement of load and torque cells with a unified sensor that combines both type of measurements will increase the stiffness of the system. Additionally, dynamic balancing of the propeller, to eliminate mass imbalances around the rotational axis, is highly advised regardless of the propeller's manufacturing method. Finally, accelerometers should be installed on the setup to correlate structural vibrations with the acoustic spectra.

- The contamination of the propeller's acoustic spectra by electric motor noise, characterized by narrow tonal peaks, posed a significant challenge during the experimental campaigns. While a thorough investigation of electric motor noise was beyond the scope of the research, the insights gained from attempts to mitigate this noise contamination could benefit future experiments in this area. future experiments. When selecting a brushless motor, careful consideration should be given

to the following parameters:

  - motor design: it was observed that outrunner motors are quieter than inrunner motors, and motors with a higher number of poles tend to shift noise to higher frequencies.
  - Electronic speed control (ESC): the ESC controls the speed of the motor by varying the current and voltage with a PWM signal, introducing high-frequency noise. Using a high PWM frequency can shift the noise to higher frequencies, ideally outside the audible range.
  - Loading conditions: motor loading affects the amplitude, but not the frequency, of the tonal noise components generated by the motor. Under high-load conditions, some motor components experience greater stress, increasing noise emission;
  - Motor mounting: the way the motor is connected to the structure influences noise transmission and amplification. The installation of a thin layer of damping material between the motor and the structure could be beneficial for noise reduction.

- The study focused on investigating the aeroacoustic characteristics of a UAV propeller under clean inflow conditions. However, in real scenarios, UAV propellers are likely to encounter turbulence when operating in urban environments. Therefore, the propeller's behaviour under turbulent inflow conditions should be investigated, with a focus on the impact on boundary layer parameters such as laminar-to-turbulent transition and the characteristics of LSBs.

- Chapter 5 demonstrated that applying a turbulator to the blade surface effectively suppresses the LSB and, as a consequence, reduces the high-frequency hump in the far-field noise spectrum. Further investigations are needed to assess the impact of the turbulator on the aerodynamic performance of the propeller.

With regard to the study of co-rotating propellers presented in Chapter 6, the following recommendations are provided:

- The main issue of a co-rotating configuration is constituted by the poor aerodynamic performance of the lower rotor (particularly when the azimuthal separation is decreased). One potential strategy worth exploring is to differentiate the geometry of upper and lower rotors, such as using an upper rotor with a smaller radius than the lower rotor. This would ensure that only the inner part of the lower rotor is affected by the wake of the upper one, while the outer part would operate in a clean flow. Another strategy that could be investigated is applying a differential collective pitch, which involves increasing the collective pitch angle of the lower rotor. This adjustment would increase the angle of attack and, consequently, the produced thrust.

- A detailed optimization study focusing on key design parameters, such as blade shape, pitch angle, and rpm could be conducted. In this study, low-fidelity methods such as vortex ring models or momentum theory could be employed to quickly

assess performance trade-offs and identify promising design candidates. Once potential configurations are established, high-fidelity simulations can be used for further refinement and validation of these designs.

A

SENSITIVITY OF LBL-VS AND TBL-TE NOISE PREDICTION MODELS

This appendix assesses the sensitivity of the LBL-VS and TBL-TE noise prediction models used in Chapter 5 to changes in the angle of attack α. To achieve this, a fixed wing with a NACA 4412 airfoil (the same one used for the isolated propeller blade presented in this thesis) is examined, varying α from 0 to 6 degrees. The wing has a chord length of 0.03 m/s, a span of 0.15 m and it is operated at a free-stream velocity of 50 m/s, corresponding to a chord Reynolds number of 10^5. The noise is evaluated at a distance of 3 m from the mid-span of the wing. The results for the two noise models are plotted in Figs. A.1 and A.2, where the left side shows the output noise spectra for each α, whereas the right side represents the ΔSPL, which is the difference in the noise level when a variation of 1 deg of angle of attack is applied. For each α, the difference is calculated with respect to the previous one.

For the LSB-VS noise model, when α is increased, the level of the predicted tone reduces substantially. Furthermore, a change of α has only an effect on the amplitude of the tone and not on the frequency. It appears that only when α is varied from 0 to 1 deg the ΔSPL is below 10 dB, while for all the other cases a variation higher than 10 dB is found. The maximum variation found is 19 dB and corresponds to a change of α from 2 to 3 deg. This high sensitivity of the model to a change of angle of attack might be not very realistic and should be verified against experimental data.

On the other side, the TBL-TE noise model shows an increase in the noise level and a shift towards lower frequencies when α is increased. In this case, the model is much less sensitivity to the angle of attack. Indeed, the ΔSPL found varies from 1 dB up to a maximum of 2 dB.

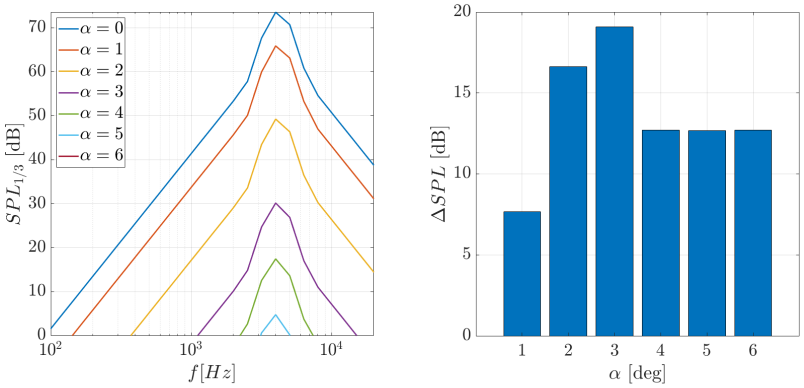

Figure A.1: LBL-VS noise model results for a straight wing at different α (left). Variation of the noise level Δ**SPL** with respect to a change of α of 1 deg (right).

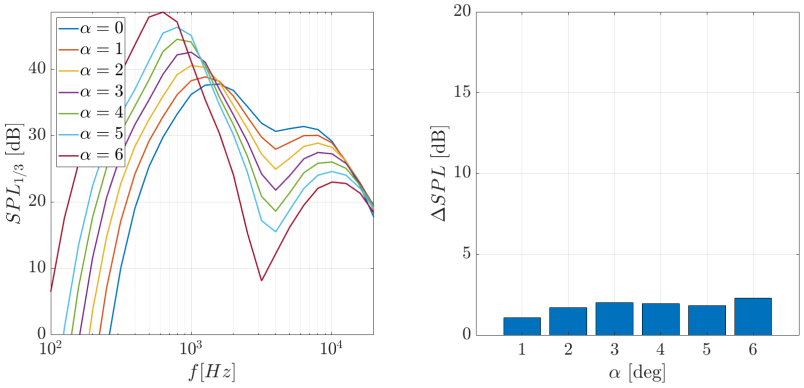

Figure A.2: TBL-TE noise model results for a straight wing at different α (left). Variation of the noise level Δ**SPL** with respect to a change of α of 1 deg (right).

CURRICULUM VITÆ

Edoardo GRANDE

11-09-1992 Born in Avellino, Italy.

RESEARCH & WORK EXPERIENCE

2022–today Acoustics & Vibration Engineer
Airbus Defence & Space, Manching, Germany

2018–2022 PhD Candidate
Delft University of Technology, Delft, The Netherlands

EDUCATION

2015–2018 MSc in Aeronautical Engineering
Roma Tre University, Rome, Italy

2011–2015 BSc in Mechanical Engineering
Roma Tre University, Rome, Italy

List of Publications

Journal Articles

8. **E. Grande**, S. Shubham, F. Avallone, D. Ragni, D. Casalino, *Computational aeroacoustic study of co-rotating rotors in hover*, Aerospace Science and Technology, 153 (2024)

7. S. Meloni, E. de Paola, **E. Grande**, D. Ragni, L. G. Stoica, A. Di Marco, R. Camussi, *A wavelet-based separation method for tonal and broadband components of low Reynolds-number propeller noise*, Measurement Science and Technology, 044007 (2023)

6. **E. Grande**, D. Ragni, F. Avallone, D. Casalino, *Laminar separation bubble noise on a propeller operating at low Reynolds numbers*, AIAA Journal, 5324-5335 (2022)

5. G. Romani, **E. Grande**, F. Avallone, D. Ragni, D. Casalino, *Computational study of flow incidence effects on the aeroacoustics of low blade-tip Mach number propellers*, Aerospace Science and Technology, 107275 (2022)

4. F. Yunus, **E. Grande**, D. Casalino, F. Avallone, D. Ragni, *Efficient low-fidelity aeroacoustic permanence calculation of propellers*, Aerospace Science and Technology, 107438 (2022)

3. **E. Grande**, G. Romani, D. Ragni, F. Avallone, D. Casalino, *Aeroacoustic Investigation of a Propeller Operating at Low Reynolds Numbers*, AIAA Journal, 1-12 (2021).

2. D. Casalino, **E. Grande**, G. Romani, D. Ragni, F. Avallone, *Definition of a benchmark for low Reynolds number propeller aeroacoustics*, Aerospace Science and Technology, 113 (2021)

1. G. Romani, **E. Grande**, F. Avallone, D. Ragni, D. Casalino, *Performance and noise prediction of low-Reynolds number propellers using the Lattice-Boltzmann method*, Aerospace Science and Technology, 107086 (2021)

Conference Proceedings

8. **E. Grande**, D. Ragni, F. Avallone, D. Casalino, *Laminar separation bubble noise in a propeller operating at low Reynolds numbers*, 28th AIAA/CEAS Aeroacoustics 2022 Conference, Southampton, UK (2022)

7. S. Meloni, E. de Paola, **E. Grande**, D. Ragni, L. G. Stoica, A. Di Marco, R. Camussi, *Wavelet-based decomposition of the tonal-broadband components of propeller noise*, 28th AIAA/CEAS Aeroacoustics 2022 Conference, Southampton, UK (2022)

6. W. Baars, **E. Grande**, D. Ragni, *Noise metrics of the time-varying acoustic far-field of rotors*, INTER-NOISE and NOISE-CON Congress and Conference Proceedings, Lexington, Kentucky (2022)

5. **E. Grande**, D. Ragni, F. Avallone, D. Casalino, *Laminar separation bubble noise in a propeller operating at low Reynolds numbers*, 2nd Delft International Conference on Urban-Air-Mobility, Delft, the Netherlands (2022).

4. S. Shubham, F. Avallone, **E. Grande**, D. Casalino, *Computational Aeroacoustic Investigation of Co-rotating rotors for Urban Air Mobility*, 1st Delft International Conference on Urban-Air-Mobility, Delft, the Netherlands (2021).

3. G. Romani, **E. Grande**, F. Avallone, D. Ragni, D. Casalino, *Low-Reynolds Number Propeller Noise Prediction Using the Lattice-Boltzmann/Very Large Eddy Simulation Method*, 1st Delft International Conference on Urban-Air-Mobility, Delft, the Netherlands (2021).

2. **E. Grande**, G. Romani, D. Ragni, F. Avallone, D. Casalino, *Experimental Aeroacoustics Investigation of a Propeller Operating at Low-Reynolds Number*, 1st Delft International Conference on Urban-Air-Mobility, Delft, the Netherlands (2021).

1. P. Candeloro, R. E. Nargi, **E. Grande**, D. Ragni, T. Pagliaroli, *Experimental Fluid Dynamic Characterization of Serrated Rotors for Drone Propulsion*, AIVELA XXVIII National Meeting 2020 17-18 December, Ancona, Italy (2020).

C'é un momento preciso, nella tua vita,
in cui capisci che puoi andare da solo.
Vicino a te, ad accompagnarti, c'é sempre
qualcuno di particolarmente caro.
In senso fisico, oppure metaforico.
Ma poi ti lascia andare e sei tu, solo con te stesso,
dapprima in equilibrio precario e poi sempre piú
stabile e solido.
Sei #alvento.

Alvento - Italian Cycling Magazine